Nondestructive Evaluation of Alkali-Silica Reaction (ASR) in Concrete

BY

MEREDITH STROW
B.S., Illinois State University, 2013

THESIS

Submitted as partial fulfillment of the requirements
for the degree of Master of Science in Materials Engineering
in the Graduate College of the
University of Illinois at Chicago, 2019

Chicago, Illinois

Defense Committee:

Dr. Didem Ozevin, Chair and Advisor, Civil and Materials Engineering
Dr. Alex Heifetz, Argonne National Laboratory
Dr. Ernesto Indacochea, Civil and Materials Engineering

ACKNOWLEDGMENTS

This research was initially started as a partnership between Argonne National Laboratory (ANL) and CTLGroup. I only stumbled upon it during Dr. Sasan Bakhtiari's (ANL) guest presentation in Dr. Didem Ozevin's NDT of Materials course, where I recognized images of cracked concrete as my own specimens from petrographic testing at CTLGroup. What lead me to embark on this research was truly being in the right place at the right time.

I'd like to begin extending my utmost gratitude to Dr. Didem Ozevin for acting as my thesis advisor, aiding in acoustic microscope testing, and exchanging specimens in the early morning on multiple occasions. Dr. Alex Heifetz is owed many thanks for sharing his research and allowing me to further it under his guidance. His supervision and assistance with electrical impedance and microwave testing was fundamental to the completion of this research. To Dr. Ernesto Indacochea, thank you for sticking around long enough to so I wouldn't have to experience the program without you; good luck in your retirement. Lastly, I would like to thank CTLGroup for supporting me in multiple ways throughout the entirety of this research. Much appreciation to Bill Demharter for performing ASTM C1293 testing, Thomas Plange for preparing samples for petrographic examination, and to Jean Randolph for being a constant source of enthusiasm and encouragement.

MLS

TABLE OF CONTENTS

CHAPTER PAGE

LIST OF TABLES

LIST OF FIGURES

LIST OF FIGURES (continued)

LIST OF FIGURES (continued)

LIST OF FIGURES (continued)

LIST OF ABBREVIATIONS

AE	Acoustic Emissions
AM	Acoustic Microscope
ANL	Argonne National Laboratory
AMBT	Accelerated Mortar Bar Test
ASR	Alkali-Silica Reaction
CPT	Concrete Prism Test
CSH	Calcium Silicate Hydrates
DEF	Delayed Ettringite Formation
DRI	Damage Rating Index
EIS	Electrical Impedance Spectroscopy
NIRAS	Nonlinear Impact Response Acoustic Spectroscopy
SCM	Supplementary Cementitious Materials
UT	Ultrasonic Testing
w/c	Water-cement ratio

SUMMARY

Alkali-silica reaction (ASR) is a mechanism of deterioration in concrete which can result in expansion cracking. The identification and evaluation of the extent of ASR deterioration is commonly conducted by petrographic examination testing on cores extracted from an affected structure. However, this mode of evaluation is destructive, requiring portions of the active structure to be removed. The purpose of this research is to aid in the pursuit of *nondestructive* test methods which can relatively quantify the amount of ASR gel present within concrete and provide a correlation to the extent of ASR-associated deterioration within the structure.

Concrete prisms were produced using two mix designs: reactive (RA) or nonreactive (NRA). The reactive mix design included siliceous aggregate and high alkali cement whereas the nonreactive mix design contained the same constituents plus fly ash. The prisms were tested in hot, moist conditions per ASTM C1293 to accelerate ASR. Nondestructive electrical impedance spectroscopy (EIS) was performed on the concrete specimens in ambient air and saturated conditions to measure impedance and bulk resistance. Microwave testing was also performed on the concrete specimens in ambient air, saturated and dry conditions to measure dielectric constant and water volume fraction. Petrographic examination and Damage Rating Index (DRI) testing was performed later to confirm the presence and extent of ASR for correlation purposes. Acoustic microscope image analysis, a type of ultrasonic testing, was also performed as another method of evaluating the extent of ASR deterioration (cracking) through image analysis.

Expansion at 365 days in reactive and nonreactive specimens was measured at 0.229% and 0.014%, respectively. Nonreactive specimens only expanded 6.11% of the measured expansion of the reactive specimens. In comparison to nonreactive specimens, reactive specimens revealed smaller real impedance (resistance) and larger imaginary impedance (capacitance), and smaller bulk resistance from EIS testing as well as smaller dielectric constants from microwave testing. Microwave testing also highlighted differences in water volume fraction between reactive specimens and nonreactive specimens. Petrographic testing identified ASR gel and deterioration ranging from a substantial amount in reactive specimens to a minor amount in nonreactive specimens. Normalized DRI scores at 365 days were 595 for Specimen RA-365 and only 52 for Specimen NRA-365. Nonreactive specimens only showed approximately 8% of the ASR-related deterioration that the reactive specimens displayed.

Based on the results of this study, it possible to distinguish between reactive and nonreactive concrete specimens using nondestructive EIS and microwave testing and correlating results with supplemental petrographic examination and DRI testing. Real and imaginary impedance, bulk resistance and dielectric constant measurements correlate to ASR-related concrete characteristics observed petrographically. Although acoustic microscope image analysis was performed on the specimens' outer surface, the surface was not successfully penetrated in order to model the interior concrete. Surface scans were produced in this study but further testing and image analysis is necessary to extract more information from the scans.

I. INTRODUCTION

A. Statement of Problem

Alkali-silica reaction (ASR) is a common form of deterioration in concrete which occurs when specific types of siliceous aggregate and alkalis within the cementitious paste react with one another and produce hygroscopic ASR gel. The ASR gel absorbs moisture and can ultimately cause expansion cracking of concrete paste and aggregates. In the past, ASR was poorly understood by civil engineers, geologists, and material scientists and reactive siliceous aggregate was used in concrete without precaution. Presently, test methods and specifications exist to limit the use of potentially reactive aggregate as well as the alkali content in cement. However, a number of concrete structures containing reactive aggregates were built before ASR was widely understood , and these currently exhibit cracking and require evaluation. Critical infrastructure concrete structures, such as those existing in nuclear power plants, restrict destructive testing methods for evaluation due to nuclear health and safety protections. Nondestructive tests methods are necessary in these situations to provide valuable information with minimal harm to the integrity of the structure.

Several techniques have been utilized in the pursuit of nondestructive ASR test methods including visual inspection, acoustic shear wave tomography, length change sensor monitoring, acoustic emissions, and ultrasonics (linear and nonlinear). While preliminary results showed promise in laboratory tests, transition to field applications requires further studies to develop a

procedure for detection and identification of ASR in the presence of confluence factors, such as other concurrent deleterious mechanisms. Therefore, diversity of ASR detection signatures could prove very important in ultimate field applications. Few ASR studies have investigated the use of electromagnetics to understand electrical properties of ASR and its resultant effects on concrete. This study aims to use electrical impedance spectroscopy and microwave testing in an attempt to find alternate methods of nondestructively evaluating the progression and degree of ASR in concrete.

B. Objectives and Approach

This study aims to find correlations between nondestructive techniques of electrical impedance spectroscopy and microwave testing and the ASR progression in concrete. Air-entrained concrete prisms were produced using two mix designs: reactive (RA) and nonreactive (NRA). The reactive mix design consisted of nonreactive carbonate coarse aggregate, reactive siliceous fine aggregate and high alkali portland cement. The nonreactive mix design contained the same constituents with the addition of fly ash, which replaced a fraction of the portland cement. The concrete prisms were subjected to the same conditions as ASTM C1293 testing to accelerate ASR. Changes in length and mass were measured frequently to monitor the progression and magnitude of ASR over time using established methods.

Nondestructive electrical impedance spectroscopy (EIS) and microwave testing were performed on the concrete specimens to measure impedance (real and imaginary), bulk

resistance, and dielectric constant with the aim of correlating electrical properties to the presence or progression of ASR in concrete. EIS and microwave testing were performed on the concrete prisms in ambient air, saturated and dry conditions. Petrographic examination and Damage Rating Index (DRI) testing were performed to establish an independent benchmark of the presence and extent of ASR gel and resultant deterioration for correlation purposes. Acoustic microscope image analysis was also performed as an additional technique to identify the extent of ASR deterioration (cracking).

C. Structure of Thesis

This thesis document presents in Chapter 1 the problems faced in the pursuit of nondestructively evaluating ASR in concrete and thereafter describes the approach taken in this study in the hopes of contributing valuable scientific data to the understanding of ASR. Chapter 2 provides a description of the ASR process in concrete, how ASR has been evaluated in concrete both destructively and nondestructively, and a brief summary of previous work associated to this study. Chapter 3 documents experimental procedures and equipment used to create concrete prism specimens and measure their length and mass change, perform EIS and microwave testing, and confirm ASR gel and associated deterioration through petrographic examination, DRI testing and acoustic microscope image analysis. Chapter 4 discusses the results of each step of testing and Chapter 5 concludes with a summary of the results as they pertain to the aim of this study. Future work is also discussed in Chapter 5.

II. BACKGROUND

A. Alkali-Silica Reaction (ASR) in Concrete

Alkali-silica reaction (ASR) was first identified by Thomas Stanton nearly 80 years ago and is now considered to be one of the most common and damaging deterioration mechanisms observed in concrete structures [40]. In general terms, alkali ions in pore solution react with reactive silica aggregate to form ASR gel. This hygroscopic gel absorbs water, which often results in expansion cracking. ASR gel reveals itself as colorless to white deposits circumscribing reactive aggregate particles, extending outwardly from reactive aggregate particles through microcracks and macrocracks, filling pore space within the paste microstructure, and lining to filling air voids within the concrete. ASR deterioration is commonly identified in concrete when cracking and/or white deposits become noticeable on exterior surfaces during visual inspection.

Concrete is formed when cement, aggregate, and mixing water are combined; mix constituents may also include supplementary cementitious materials (SCMs) and admixtures (air-entraining, water-reducing, etc.). The combination of cement with mixing water creates a paste which holds aggregate particles together. The paste is formed by calcium silicates, supplied by the cement, which react with mixing water to form calcium silicate hydrates (CSH) and calcium hydroxide. The CSH bonds provide the majority of the concrete strength. However, the cement also supplies alkalis (Na^+ and K^+), to the paste microstructure and pore solution. Alkalis

provided by cement and mixing water play an important role in the ASR deterioration mechanism [16, 17, 29, 33, 39].

ASR deterioration is characterized by three main stages: 1) reaction of alkaline pore solution and siliceous aggregate, 2) formation of hygroscopic gel, and 3) concrete expansion as gel absorbs and retains moisture (Figure 1) [33]. The reaction between pore solution and aggregate begins when there are sufficiently high levels of sodium hydroxide and potassium oxide in cement pore solution [17]. The hydroxide ions cleave bonds of the metastable silica (SiO_2) in aggregate particles, followed by imbedding of Na+ and K+ into the silica matrix to form ASR gel [33]. Finally, the hygroscopic ASR gel absorbs moisture, swells, and ultimately causes expansion in concrete. It is of importance to note that the ASR deterioration mechanism has been described, but not all concrete which experiences ASR gel formation experiences deterioration (cracking) [17].

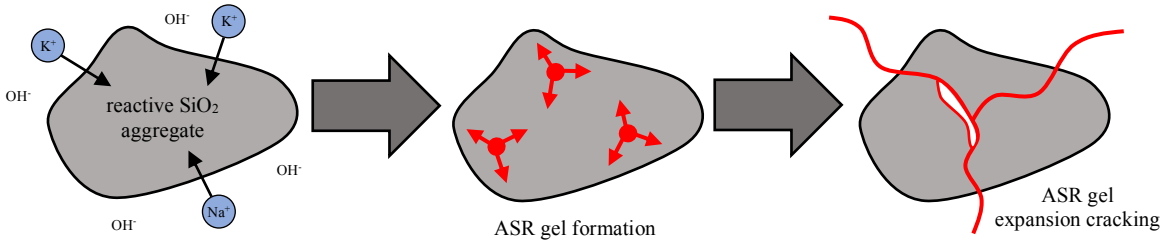

Figure 1 Progression of alkali-silica reaction

Although many studies have been conducted to understand ASR and develop accelerated tests for concrete mix evaluation, the reaction can still occur even when the concrete mix was qualified with such tests. For example, aggregates could be qualified using ASTM C1260 or ASTM C1567 accelerated mortar bar testing (AMBT) or ASTM C1293 concrete prism testing (CPT). However, the mix might not perform well in the field, or when the deleterious nature of the aggregate has gone unidentified in laboratory testing. ASTM C295, petrographic examination of aggregate for concrete [5], is a useful test for identifying the deleterious nature of aggregate particles. It can also still occur when SCMs, such as fly ash, are incorporated in the mix.

For economic reasons, the type of aggregate used in concrete is generally local to the geographic region in which the structure is built. However, rock types vary by geographic location and, therefore, a variety of aggregates are used in concrete structures around the world. Silicates make up the largest portion of rock-forming minerals on this planet; however, silica (SiO_2) is found in many forms including quartz and quartzite, strained quartz, microcrystalline or cryptocrystalline quartz (e.g. chert and chalcedony), volcanic glass (e.g. cristobalite), and other forms of amorphous silica (e.g. opal) [28]. The type of reactive silica may be present as chert within cherty limestone in one geographic location whereas in another location the reactive silica may be present as strained quartz within a metamorphic gneiss particle. Proper identification of aggregate particles and their potentially deleterious nature are critical to reducing the probability of ASR deterioration in concrete.

B. Evaluation of ASR Using Destructive Techniques

The most common and effective mode of identifying the presence of ASR gel in concrete and evaluating the extent of associated damage is petrographic examination. However, this type of analysis requires concrete to be extracted from the structure and, therefore, it is a destructive test method. Petrographic examination of concrete, ASTM C856, yields valuable information including aggregate rock lithology or lithologies, determination of reactive rock type or types, qualitative amount of ASR gel, and degree of deterioration (cracking) and deterioration characteristics [6]. The analysis is qualitative in nature and does not provide a prognosis for future expansion.

Although standard petrographic examination of concrete only yields qualitative information, it can be performed in conjunction with DRI testing which provides quantitative information for ASR evaluation. The DRI test method, described by Grattan-Bellew [22] and Dunbar and Grattan-Bellew [20], quantifies the amount of ASR-related deterioration features present in a concrete specimen. This test method is often performed as supplemental testing to petrographic examination because it requires a semi-polished, or lapped, concrete surface which is often prepared for petrographic examination. DRI is the most effective approach for quantifying ASR deterioration while also providing visual confirmation of ASR gel and its characteristics within concrete. Similar to the petrographic examination, this approach does not provide prognosis for future ASR expansion.

Residual expansion testing, on the contrary, does provide ASR prognosis information. Fournier et al. proposed this destructive test method which involves extracting cores from ASR-affected structures and storing them in two types of conditions: 1) over-water in air at 95 percent or greater relative humidity (RH) and at 38°C (100°F), and 2) submerged in 1N NaOH solution at 38°C (100°F) [21]. These conditions are intended to represent realistic expansion and residual reactivity of the concrete, respectively. The first condition replicates ASTM C1293, 'Standard test method for determination of length change of concrete due to alkali-silica reaction,' testing conditions [8]. Length expansion measurements collected over the course of one year (% exp./yr) are used to predict the degree of concrete expansivity and aggregate reactivity. No other test method as of yet, either destructive or nondestructive, provides both diagnosis and quantitative prognosis of ASR using concrete from the active structure. In addition, Fournier et al. suggest supplementing residual expansion testing with water-soluble alkali testing of the concrete; this is also done destructively by obtaining core samples from the structure. The amount of water-soluble alkalis extracted from concrete allows for interpretation regarding whether or not the concrete contains enough alkalis to either produce ASR gel or to further ASR deterioration. Water-soluble alkali testing offers meaningful information for both diagnosis and prognosis assessments of ASR. Residual expansion testing is often conducted alongside petrographic examination and DRI testing for visual confirmation of ASR and correlation of data [21].

Rivard et al. conducted a study where concrete prisms which, after undergoing ASR expansion testing, were impregnated with fluorescent epoxy resin and urneyl acetate to assess

cracking and gel content [36]. DRI testing and image analysis was subsequently performed to correlate the amount of gel, and extent of confirmed ASR-related deterioration. Although Rivard et al. found a correlation between image analysis and length expansion data, no clear correlation was made between the amount of gel and length expansion. The results of this thesis study does, however, make this correlation.

C. Evaluation of ASR Using Nondestructive Techniques

A variety of nondestructive techniques have been studied to aid in the evaluation of ASR deterioration. Nondestructive ASR testing can be divided into two groups: laboratory testing and field testing. Laboratory testing typically consists of preparing concrete samples within the laboratory, inducing ASR, and evaluating concrete properties and characteristics. This type of testing is helpful in qualifying materials for use in concrete and understanding how materials may perform in field conditions. Field testing consists of investigating in-situ concrete structures without damaging the integrity of the structure; no samples are removed and the structure is not taken out of service. This type of testing supplies data which is specific to the structure, its materials, and the environment which it exists in; these variables are fairly impossible to recreate in a laboratory setting.

The three most common laboratory tests performed for evaluating alkali-silica reactivity of concrete constituents are 1) ASTM 1260: Standard test method for potential alkali reactivity of aggregates, 2) ASTM C1567: Standard test method for determining the potential alkali-silica

reactivity of combinations of cementitious materials and aggregate, and 3) ASTM C1293: Standard test method for determination of length change of concrete due to alkali-silica reaction. ASTM C1260 and ASTM C1567 are considered accelerated tests due to the total testing period of 16 days, compared to that of ASTM C1293 testing which takes one to two full years [7, 8, 9].

ASTM C1260 is an accelerated mortar bar test which evaluates a specific aggregate's ability to react with a typical portland cement. The test uses one crushed and properly graded aggregate to produce at least three 1 x 1 x 11.25 in. mortar bars. The mortar bars, after curing, are submerged in sodium hydroxide solution for 14 days and length change measurements are collected to calculate percent expansion. ASTM C1260 states that final percent expansion of less than 0.10% indicates innocuous aggregate reactivity behavior, final percent expansion of greater than 0.20% indicates potentially deleterious aggregate reactivity behavior, and expansion between 0.10 to 0.20% is inconclusive because both aggregates known to be reactive and aggregates known to be nonreactive have expanded within this range. If an aggregate fails ASTM C1260 testing, ASTM C1567 testing is commonly recommended to reevaluate the potential for reactivity with the use of ASR-mitigating supplementary cementitious materials, such as fly ash or slag [7].

ASTM C1567 is also an accelerated mortar bar test, but this test evaluates a specific aggregate's ability to react with a typical portland cement in combination with supplementary cementitious materials, such as fly ash. Like ASTM C1260, the test uses one crushed and

properly graded aggregate to produce at least three 1 x 1 x 11.25 in. mortar bars. The mortar bars, after curing, are submerged in sodium hydroxide solution for 14 days and length change measurements are collected to calculate percent expansion. ASTM C1567 states that final percent expansion of greater than 0.10% indicates potentially deleterious aggregate reactivity behavior [9].

ASTM C1293 is the one-year long equivalent of ASTM C1260 and the two-year long equivalent of ASTM C1567. ASTM C1293 testing uses one crushed and properly graded aggregate with a known nonreactive counterpart (fine or coarse aggregate) to produce at least three 3 x 3 x 11.25 in. concrete prisms, or prisms. If the test is intended to determine reactivity of a fine aggregate, a known nonreactive coarse aggregate is used in the concrete mix. Conversely, if the test is intended to determine reactivity of a coarse aggregate, a fine aggregate known to be nonreactive is used in the concrete mix. The test can be performed on portland cement concrete as well as concrete designed with supplementary cementitious materials. The concrete prisms are submerged in sodium hydroxide solution for one to two years and length change measurements are collected to calculate percent expansion. ASTM C1293 states that final percent expansion of greater than 0.04% indicates potentially deleterious aggregate reactivity behavior. The standard also states that expansion of less than 0.04% in prisms containing portland cement after one year and in prisms containing portland cement and supplementary cementitious materials after two years is considered innocuous [8].

Another laboratory test which aids in the evaluation of aggregate reactivity is ASTM C295: Standard guide for petrographic examination of aggregates for concrete. This test is performed by identifying the rocks and minerals within an aggregate (coarse or fine), per ASTM C294 descriptive nomenclature, and quantifying the amount of each observed rock lithology for a total classification of the aggregate sample [4, 5]. Deleterious rock types and particles containing potentially reactive mineralogy are quantified with the intent of providing engineers, quarries, and ready-mix producers information to help understand the characteristics of the material and its potential limitations for use in concrete or other building materials. For example, a limestone aggregate may contain individual chert particles or limestone particles containing chert; the total weighted percent of chert and particles containing chert would be reported because chert consists of microcrystalline quartz which is potentially reactive with the alkalis in portland cement. ASTM C295 testing is commonly performed prior to ASTM C1260, ASTM 1567, and ASTM C1293 testing because results indicate whether or not potentially reactive particles exist within an aggregate sample.

Field testing of in-situ structures for ASR evaluation can be performed nondestructively by one or more, but not limited to, the following field techniques: visual observation, acoustic shear wave tomography, length expansion sensor monitoring, acoustic emissions (AE), ultrasonic testing (UT), EIS, and microwave testing. Visual observation of cracks and/or white ASR gel deposits is the most straight forward and inexpensive nondestructive technique; however, it takes a trained eye to discern ASR gel from other types of white secondary deposits

such as ettringite and calcium carbonate efflorescence. The other listed techniques are briefly described in the following text. Electrical impedance spectroscopy and microwave testing are explained in greater detail to provide more pertinent information relating to the objective of this study.

Acoustic shear wave tomography, which uses the ultrasonic pulse-echo technique, has the ability to detect surface-parallel macrocracks, reinforcement (rebar), and other forms of discontinuities in concrete. Commercial system sold under brand name MIRA is commonly used for identifying the depth of horizontal cracks and delamination cracks, finding rebar, evaluating the thickness of concrete repair cover, and similar concrete features [13]. However, MIRA is not capable of identifying microscopic features such as microcracks and ASR gel within concrete. If a structure has experienced significant ASR cracking and exhibits macrocracks, this equipment may provide valuable information such as in a recent study of Seabrook Nuclear Power Plant where MIRA data was correlated to ASR-related expansion and ASR gel and deterioration was confirmed with petrographic examination [15].

Concrete expansion measurements can be collected nondestructively through the use of sensors applied to an in-situ structure. The process of installing demountable mechanical strain gauge (DEMEC) points on concrete surfaces at known initial distances and periodically collecting length change measurements between sensors provides expansion information and can indicate relative degrees of expansion within the same structure [21]. This test method provides

rate of expansion which can be correlated to laboratory expansion data. Although length expansion can be due to ASR, it is important to understand the structure and other possible chemical and/or structural mechanisms which could also be affecting length change measurements, such as cracking due to delayed ettringite formation (DEF) or as a result of loading.

Another nondestructive method used to evaluate ASR is acoustic emissions. Acoustic emission testing of ASR deterioration in concrete has experienced much difficulty because ASR gel substantially attenuates AE signals [31]. Lokajicek et al. determined that acoustic emission data can be informative in the early stages of ASR growth but as the amount of ASR gel and cracks increase, the technique loses sensitivity [31]. This is been a common finding with AE-related ASR investigations. However, Abdelrahman et al. was able to correlate AE data to ASR maturity in concrete prisms through testing similar to C1293 with confirmation of ASR gel and deterioration via petrographic examination and DRI testing [1].

Ultrasonic testing of ASR-damaged concrete has been conducted in numerous successful studies. Both linear and nonlinear ultrasonic testing have been performed; however, although linear ultrasonic testing is able to detect wave speed and attenuation changes in ASR-affected concrete, linear testing is not adequately sensitive for effective nondestructive testing [8]. Nonlinear ultrasonic testing, conversely, offers a much greater degree of sensitivity. Several studies show correlations between ASR deterioration and the acoustic nonlinear parameter, a

parameter which utilizes linear attenuation measurements. The acoustic nonlinearity parameter has been shown to correlate to degradation of strength in ASR-affected concrete, ASR-related length expansion, microcracking, DRI testing results, and relative permittivity (microwave backscatter parameter). Because the acoustic nonlinearity parameter has been successfully correlated to ASR on a broad scale, it is considered an effective tool for nondestructive ASR evaluations, based on laboratory testing [12, 27, 30, 34, 37].

Chen et al. studied the Nonlinear Impact Response Acoustic Spectroscopy (NIRAS) method, which uses the acoustic nonlinear technique, on AMBT specimens. The study measured shifts in resonance frequency as a factor affecting the nonlinearity parameter and testing showed more sensitivity to damage in general and especially in early ages of aggregate reactivity than linear techniques. This study provided substantial evidence of correlation between the nonlinearity parameter of concrete and the degree of ASR cracking and deterioration features, particularly in the early ages of ASR growth and progression [11]. The NIRAS approach and, again, the acoustic nonlinear parameter appear to be effective tools for evaluating the ASR process in concrete, based on laboratory testing.

Electrical impedance spectroscopy (EIS), chosen for this study, measures impedance (Z) which is defined as "a measure of a circuit's tendency to resist (or impede) the flow of alternating electrical current" [32]. Additionally, impedance is made up of real and imaginary parts. The real part, real impedance (Z'), refers to resistance, or the ability to resist current flow.

The imaginary part, imaginary impedance (Z"), refers to capacitance, or the ability to store energy [20]. Impedance is directly affected by moisture content within concrete; moisture is required for a material to be adequately conductive for impedance spectroscopy testing [14]. EIS can measure several variables in order to evaluate the microstructure of a material. Bulk resistance of different types of cement was studied by Christensen et al. and it was found that 1) denser pastes exhibit greater bulk resistance, and 2) cement pastes exhibit greater bulk resistance over time as hydration of CSH progresses [14]. Real and imaginary impedance as well as bulk resistance was studied by Heifetz et al. and is discussed later in this text.

In addition to evaluating bulk resistance and impedance parts, EIS has been used to estimate cracking and the effect of supplementary cementitious materials (SCMs) on dielectric constant [41, 42]. However, there is a lack of information and rare studies of ASR in concrete using EIS. Research conducted by Shi et al. and Heifetz et al. has provided some initial data which shows resistance and phase angle EIS measurements trending with increasing amounts of reactive aggregate and ASR progression [25, 38]. Experiments conducted by Heifetz et al. are discussed in the following section.

Microwave testing employs the use of transducers to send waves through a material and the ways in which the signals move (mainly reflect and transmit) through the material are studied to postulate methods of detecting subsurface characteristics. Research has been conducted on concrete and mortar specimens to better understand electromagnetic properties such as relative

permittivity, dielectric constant, loss factor and reflection coefficients in relation to subsurface defects such as cracking and ASR progression or characteristics such as moisture content. The dielectric constant, a complex parameter which measures electrical energy storage, is principally characterized by its real (relative permittivity) and imaginary (relative loss factor) parts; relative permittivity measures a material's ability to store energy and the relative loss factor measures a material's ability to lose energy. Reflection (S_{11}) and transmission (S_{22}) coefficients can also be measured to provide useful reflected and transmitted signal information for determining dielectric constants for material characterization [19, 25, 26].

Jamil et al. performed electromagnetic testing to measure dielectric constant, loss factor, and reflection coefficient on concrete specimens with varying water-cement ratios (w/c), varying fiber content, and varying chloride content [26]. The study found that high w/c initially corresponded to high dielectric constant values in the first week of testing but high w/c later corresponded to the lowest dielectric constant values reported; this phenomenon was purportedly attributed to the availability of free water within the samples as well as hydration of cement in high w/c concrete initially compared to that of lesser free water availability in lower w/c concrete. The same study also measured dielectric constant for concrete containing varying amounts of steel fibers, noting a distinct correlation between the increase in dielectric constant values with increasing steel fiber volume. A similar trend was observed when the researchers tested concrete with varying amounts of chloride content [26]. Although Jamil et al. did not test for ASR-related deterioration, the study was successful in showing that electromagnetic

properties can be correlated to concrete characteristics and also that free water and cement hydration have potentially discernable effects on dielectric constant values.

Multiple studies have been conducted to understand how moisture availability in free and bound states can affect dielectric constant and reflection coefficient values in cementitious materials which undergo curing, a cement hydration process in which mixing water (free water) reacts with portland cement and either becomes bound in hydrations products (e.g. CSH and calcium hydroxide) or evaporates [10]. These studies reported similarly trending results showing that high w/c materials initially exhibit high reflection coefficients but later exhibit low reflection coefficients in relation to their low w/c counterparts. These results, like the dielectric constant results presented by Jamil et al., are attributed to the amount of free water, which has a relatively high dielectric constant, initially available and the later loss of free water to curing or evaporation [10, 18, 19, 23, 24, 26] . As Bois et al. states, “the water content becomes less and less free and more and more bound (to cement particles) over time. The reason for this is that free water has much higher dielectric properties compared to those of cement powder, whereas bound water has similar to cement powder dielectric properties” [10].

Donnell et al. performed microwave testing on specimens made with reactive aggregate or nonreactive aggregate to study reflection coefficients, among other properties, of ASR-affected mortar; testing utilized a filled waveguide to minimize signal at the junction of the waveguide to the sample surface [19]. The results revealed smaller reflection coefficients for

reactive mortar specimens compared to nonreactive mortar specimens during the latter part of 36-day testing. Results also showed smaller dielectric constant and greater loss factor for reactive specimens throughout the entirety of testing compared to the nonreactive specimens. Microwave testing of ASR-affected concrete was studied by Hashemi et al. using S-band, R-band, and X-band frequencies comparatively amongst different curing conditions to obtain dielectric constant data [23]. Results from this study mimicked the latter study, showing smaller dielectric constant and greater loss factor for reactive specimens compared to the nonreactive specimens. These findings support the theory that microwave testing can be used as a nondestructive tool for ASR evaluations.

D. Associated Studies

This thesis study is a continuation of previous Argonne National Laboratory (ANL) nondestructive testing performed on ASR-affected non-air-entrained concrete. Heifetz et al. performed microwave testing and impedance spectroscopy on non-air-entrained reactive and nonreactive concrete prisms fabricated at CTLGroup to correlate properties such as dielectric constant, reflection (S_{11}) and transmission (S_{21}) coefficients, and impedance values to the progression of alkali-silica reactivity. The reactive and nonreactive concrete prisms were fabricated with the same constituents, except the nonreactive mix contained Class F fly ash to limit alkali-silica reactivity, and subjected to ASTM C1293 testing for one to two months to accelerate ASR progression. A cement paste-only specimen bar was also fabricated [25].

Microwave testing was performed with a portland cement filled X-band antenna and measurements were taken along one of the smooth prism surfaces of each specimen. Results of microwave testing revealed low reflectivity of reactive specimens and greater reflectivity of nonreactive specimens. Transmission data revealed higher measurements for reactive specimens and significantly lower measurements for nonreactive specimens. Microwave data clearly indicated differences in electrical properties between reactive and nonreactive specimens [25].

Impedance spectroscopy testing was performed using two electrode patches spaced 3 in. apart from each other on the same surface to couple the transducers to concrete prisms. Complex-valued impedance, phase angle, and real and imaginary impedance values were measured and plotted, showing distinct differences between reactive, nonreactive, and cement specimens in each case. Complex-valued impedance |Z| measurements, when plotted against frequency, were highest in nonreactive specimens, followed by reactive specimens at a magnitude of power lower, and the cement specimen exhibited the lowest |Z| measurements (Figure 2). Phase angle measured against frequency showed similarly clear differences between the reactive, nonreactive and cement specimens (Figure 2). When real and imaginary impedance measurements were plotted against frequency, again, the reactive, nonreactive and cement specimens plotted in notably different regions (Figure 3). Nyquist diagrams from impedance testing showed greatest resistance and capacitance in nonreactive specimens, followed by reactive specimens, and then the cement specimen (Figure 4). With decreasing resistance and capacitance, decreasing range of values was observed [25].

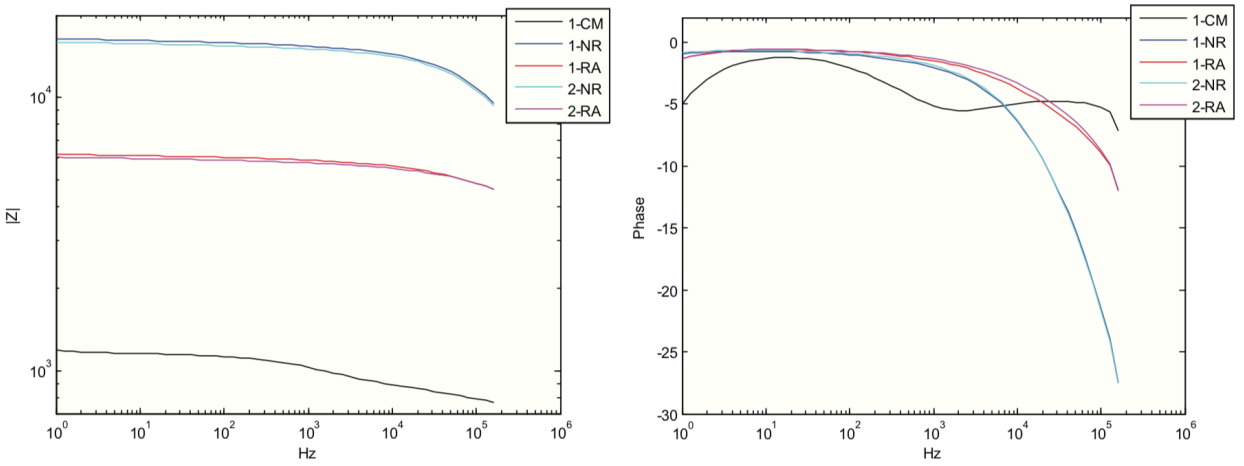

(a) (b)

Figure 2 Bode plots of complex-valued impedance (a) and phase angle in degrees (b) plotted against frequency for reactive (RA), nonreactive (NR) and cement (CM) samples [25]

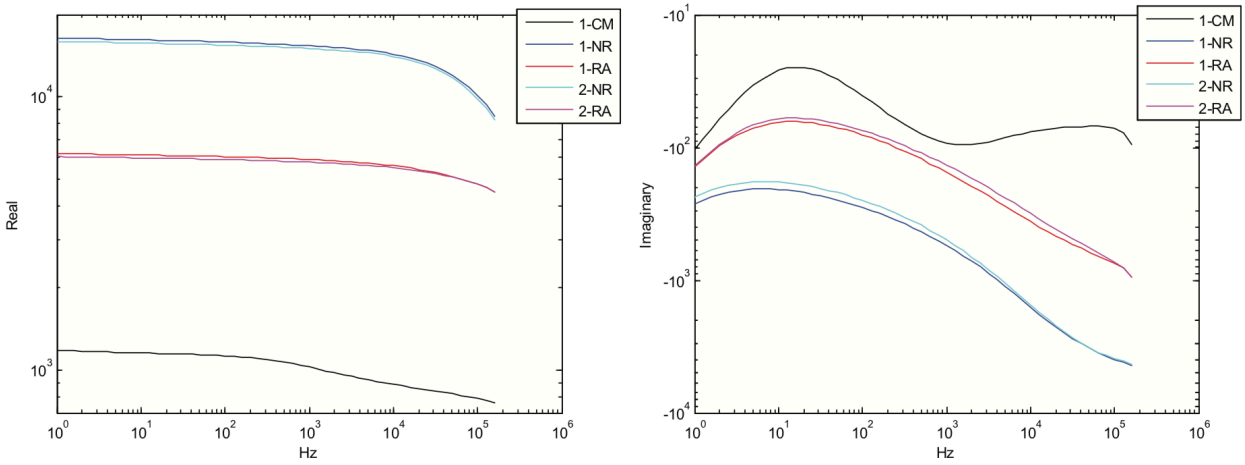

(a) (b)

Figure 3 Real (a) and imaginary (b) cartesian values in Ohms plotted against frequency for reactive (RA), nonreactive (NR) and cement (CM) samples [25]

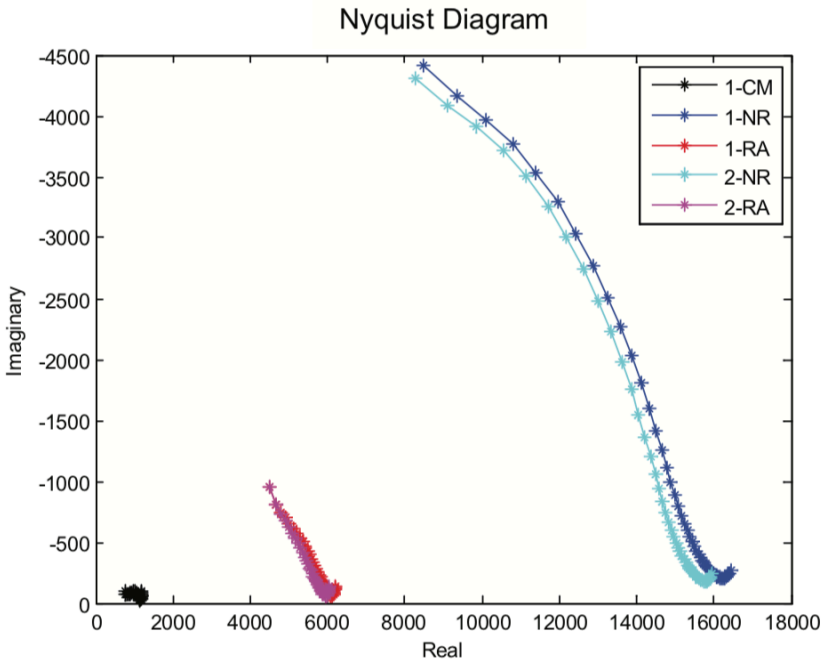

Figure 4 Nyquist diagram showing real vs. imaginary impedance values in Ohms [25]

Heifetz et al. showed reactive and nonreactive non-air-entrained specimens exhibit discernably different electrical properties through impedance spectroscopy and microwave testing. The study concluded that reactive specimens exhibit notably lower resistive and greater capacitive response, and lower X-band microwave absorption than the nonreactive specimens. The difference in measured impedance and microwave parameters was attributed to the effects of ASR on pore solution, likely ASR gel's uptake of water from pore solution, resulting in less available water in the system which reduces resistivity of the sample; however, the presence of fly ash in the nonreactive specimens could also have had an effect, since it is known to lower conductivity of concrete [25].

III. EXPERIMENTAL PROCEDURES AND EQUIPMENT

A. Concrete Prism Preparation and Mix Design

Eight 3 x 3 x 11.25 in. concrete prism specimens were cast in molds at CTLGroup on August 15, 2017. Four specimens were cast using a reactive (RA) concrete mix and the other four specimens were cast using a nonreactive (NRA) concrete mix (Figure 5). The molds consist of a bottom surface with four side walls and an open top. The mold set-up yields five formed surfaces and one struck top surface per specimen.

a)  b) 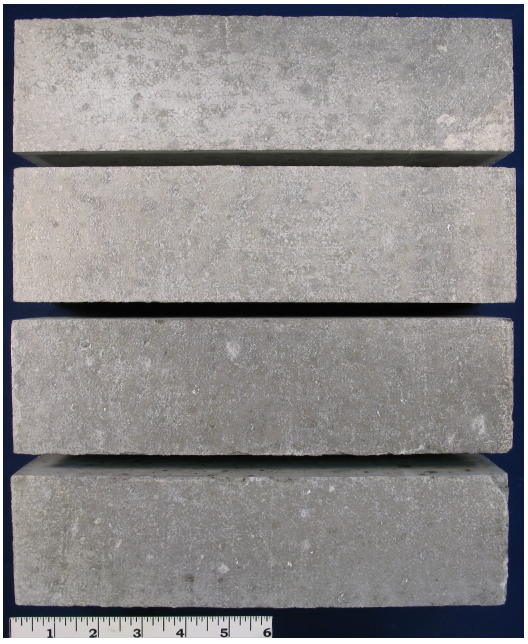

Figure 5 Concrete prism specimens showing struck top surfaces of a) RA and b) NRA specimens

For this study, the struck surface is referred to as ‘Side A’ and one adjacent formed longitudinal surface was selected for testing and referred to as ‘Side B’, with the two remaining longitudinal surfaces as Sides C and D. The majority of tests in this study were performed along the surface or parallel to the surface of Side B of each specimen. The mold set-up also allowed for placement of metal gauges in the middle of the two ends of each specimen; gauges are required to measure length change during ASTM C1293 testing.

The reactive and nonreactive concrete mix designs differ from each other by paste constituents. The cementitious paste in the reactive mix consists of portland cement. The cementitious paste in the nonreactive mix consists of both portland cement and Class F fly ash. The coarse aggregate and fine aggregate are the same in both mixes. The coarse aggregate is a crushed limestone and dolomitic limestone; this carbonate rock type is not alkali-silica reactive. The fine aggregate is a siliceous natural sand which contains some rock types known to be deleteriously reactive with the alkalis in concrete [4]. Both mixes are air entrained. The main difference between the two mixes is the addition of fly ash into the nonreactive mix; fly ash is known to mitigate ASR in concrete. Both mixes contain reactive aggregate; however, the terms reactive and nonreactive denote the absence or presence, respectively, of fly ash in the mix. TABLE I summarizes the concrete constituents within each mix.

TABLE I RA AND NRA CONCRETE MIX DESIGNS

Concrete Constituent	**Reactive Mix (RA)**			**Nonreactive Mix (NRA)**		
	Weight (lbs./batch)	Weight %	Volume %	Weight (lbs./batch)	Weight %	Volume %
High-Alkali Portland Cement	19.7	18.8	13.3	13.8	13.4	9.3
Class F Fly Ash	N/A	N/A	N/A	5.9	5.7	5.3
Water	8.5	7.9	17.7	8.5	8.0	17.7
Air Entrainment	-	-	5.5	-	-	5.5
Coarse Aggregate	51.0	49.2	42.9	51.0	50.1	42.9
Fine Aggregate	25.4	24.0	20.6	23.8	22.8	19.2

B. Concrete Length and Mass Change Testing

All eight concrete prisms were tested in general accordance with ASTM C1293, Standard Test Method for Determination of Length Change of Concrete Due to Alkali-Silica Reaction, except that the concrete specimens are air-entrained [8]. Concrete prism specimens were cast and cured in accordance with ASTM C192, Practice for Making and Curing Concrete Test Specimens in the Laboratory [3], and specimens were measured in accordance with ASTM C157, Test Method for Length Change of Hardened Hydraulic-Cement Mortar and Concrete [2]. Specimens were removed from their casting molds after 23.5 $\pm$ 0.5 hours of moist curing and subsequently placed in a lime-saturated water tank for 30 minutes to reduce variation in length measurements due to temperature flux. After 30 minutes, the initial length change measurement

was recorded and the specimens were thereafter stored in moist conditions at 38.0 ± 2 °C until 28 days. Length measurements were collected at 1, 7 and 28 days and testing was halted; no mass change measurements were collected in the first 28 days. No additional testing was performed on the 28-day specimens, Specimens RA-28 and NRA-28.

ASTM C1293 testing was halted after 28 days due to Argonne losing funding to continue the research; testing halted on September 12, 2017 and resumed on January 12, 2018, four months later, when research was able to continue. The samples were stored in a freezer between September 12, 2017 and January 12, 2018 to significantly reduce the amount of reaction capable of occurring. Once testing resumed, the 90, 180 and 365 day specimens (RA-90, RA-180, RA-365 and NRA-90, NRA-180, NRA-365) were placed back into moist conditions at 38.0 ± 2 °C and 95% relative humidity (RH) until each set was tested for their respective amount of time. Length and mass change measurements were collected once a week through 90 days, and every 30 days afterward.

C. Electrical Impedance Spectroscopy Testing

Once specimens completed ASTM C1293 testing, electrical impedance spectroscopy (EIS) was performed on each of the specimens. Electrical impedance spectroscopy was performed using ZPlot software which communicated with a Solartron Multiplexer (1281), a Solartron electrochemical interface (SI 1287) and a Solartron frequency response analyzer (1252A). Two 2 in. by 2 in. AcuZone® self-adhesive electrode patches were placed 3 in. apart

from each other on side B of each specimen and transducers were clipped onto the electrode connectors at the center of each pad (Figure 6). Polarization settings were set to an AC amplitude of 1 V or 1000 mV (millivolts) and frequency sweep settings were set to range of 0.1 Hz to 150,000 Hz (0.15 MHz).

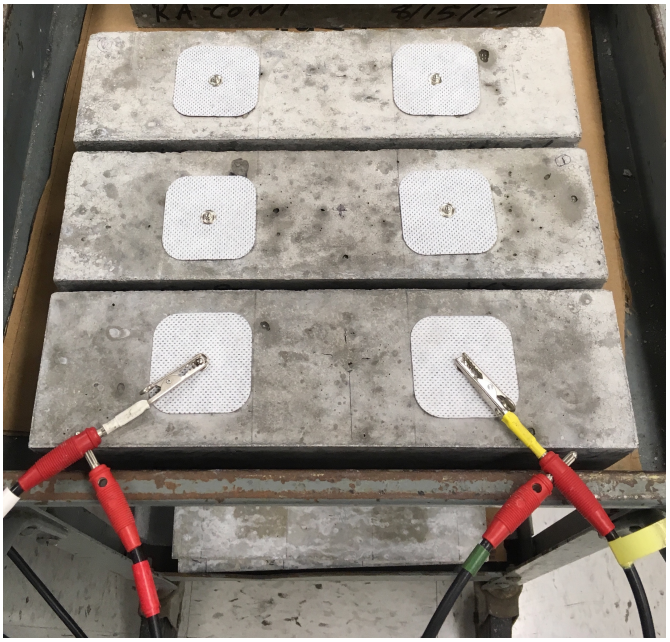

Figure 6 Side B of concrete specimens with transducers attached to electrode patch connectors

Electrical impedance testing was performed on all eight specimens in ambient air condition, after three days of being submerged in water (saturated condition), and after three

hours of heating in a furnace at temperatures ranging between 130 to 140 °C (dry condition). Specimens tested in ambient air condition were intended to represent concrete structures exposed to the environment, specimens submerged in water were intended to represent saturated structures (e.g. concrete piers below water line), and specimens heated to elevated temperatures were intended to represent structures exposed to dry heat conditions (e.g. structures in hot, dry climates or concrete furnaces).

D. Microwave Testing

After electrical impedance spectroscopy testing was completed, microwave testing was performed using a N5245A PNA-X series power network analyzer (PNA) (10 MHz to 50 GHz) produced by Agilent Technologies; setup replicated settings from associated work previously performed by Dr. Heifetz at ANL [25]. Bulk material reflection measurements were collected from the S_{11} parameter along the three smooth longitudinal surfaces of each specimen using an X-band antenna operating between 8.2 to 12.4 GHz and incident microwave power at approximately 10 dBm. The struck surface, the fourth longitudinal surface of each sample, was not tested due to its rough, irregular surface. The X-band antenna was placed upon the specimens through free space, flush to the smooth concrete surfaces.

E. Petrographic Examination and DRI Testing

Petrographic examination was performed on all eight specimens. The concrete prisms were visually inspected and photographed in intact condition after ASTM C1293 testing was

completed. The lapped surface of each specimen was also photographed and examined using a stereomicroscope at magnifications up to 50X. For thin-section study, one small rectangular block, approximately 1 in. by 1.4 in., was cut from a selected region within Specimens RA-365 and NRA-365, and one side of each of the blocks was semi-polished, or lapped, to produce a smooth, flat surface. The blocks were cleaned and dried, and the prepared surfaces were mounted on separate ground glass microscope slides with epoxy. After the epoxy hardened, the thickness of the mounted blocks was reduced to approximately 20 microns. Another set of rectangular blocks were cut from Specimens RA-28, RA-365, NRA-28 and NRA-365 for thin-section analysis using blue epoxy impregnation. The blocks were impregnated with blue epoxy, and then prepped in the same manner as the previously described thin section blocks. Thin-section analysis was performed using a polarized-light (petrographic) microscope at magnifications up to 400X to study ASR gel and deterioration, other concrete features and paste microstructure.

Damage Rating Index testing is described by Grattan-Bellew [22] and Dunbar and Grattan-Bellew [20] as a method of quantifying the amount of ASR damage This test was performed on the semi-polished, or lapped, interior surface of each of the eight specimens. A clear adhesive sheet with printed 1 x 1 cm (0.4 x 0.4 in.) grid squares was placed on each of the lapped concrete surfaces (Figure 7). Concrete features, such as microcracks and ASR gel in voids, were examined and quantified with the aid of a stereomicroscope at 16X magnification within 200 grid squares. At least 200 grid squares, or 200 cm^2, is required for sufficient data collection. DRI values were calculated by multiplying the amount of observed ASR-related

features by their corresponding weight factor, then normalized to 100 cm^2 [35]. ASR-related concrete features and their corresponding weight factor are presented in TABLE II.

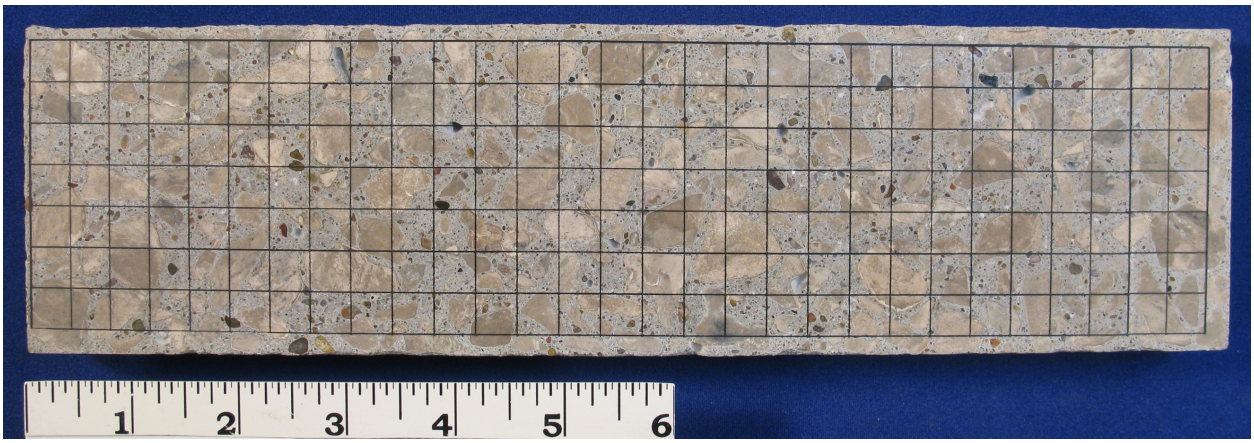

Figure 7 Specimen with DRI grid paper adhered to lapped surface

TABLE II DRI PETROGRAPHIC FEATURES AND WEIGHT FACTORS

Petrographic Features Quantified	**Weight Factor**
Coarse Aggregate Features	
Coarse aggregate with cracks	0.25
Coarse aggregate with cracks and ASR gel	2.00
Debonded coarse aggregate	3.00
Reaction rims around coarse aggregate	0.50
Fine Aggregate Features	
Fine aggregate with cracks	0.25
Fine aggregate with cracks and ASR gel	2.00
Debonded fine aggregate	2.00
Reaction rims around fine aggregate	0.25
Cement Features	
Cement paste with cracks	2.00
Cement paste with cracks and ASR gel	4.00
Air Void Features	
Air voids with ASR gel	0.50

F. Acoustic Microscope Testing

Ultrasonic testing was performed on each sample using the Sonoscan GEN6™ C-Mode Acoustic Microscope (C-SAM®). Ultrasonic testing was performed on an exterior surface and an interior, lapped surface within the specimens. The outermost 1 in. of side B of each specimen was saw-cut in order to fit fully submerged within the Sonoscan water basin (Figure 8). The interior surface of each 1-in.-thick, saw-cut sub-specimen was semi-polished, or lapped, because petrographic examination and DRI testing requires such a surface for evaluation. The ultrasonic transducer was 50 MHz with a 12.7 mm focal length and a resolution of 52 micrometer resolution. The ultrasonic beam was focused on the top surface but could not penetrate beyond the top surface successfully.

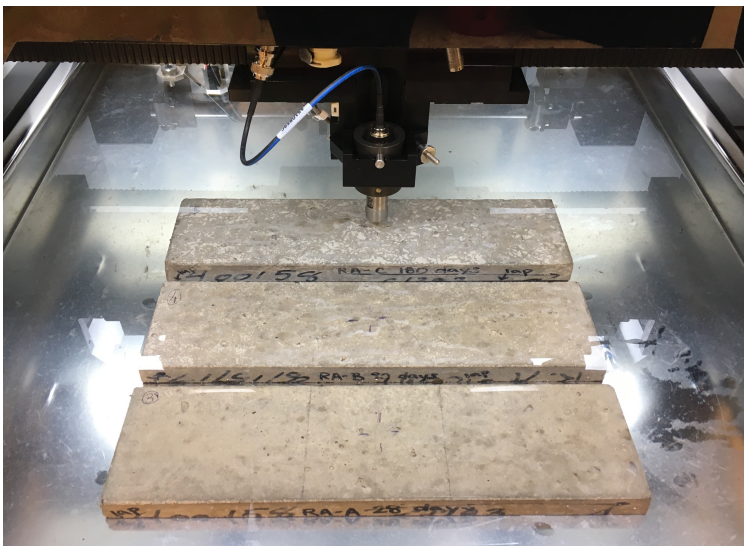

Figure 8 Subspecimens loaded into the Sonoscan water basin

IV. EXPERIMENTAL RESULTS

A. Length Expansion and Mass Change

Results of ASTM C1293 testing show a substantial degree of length expansion in the reactive specimens and a very small degree of length expansion in the nonreactive specimens (Figure 9 and Figure 10). Length expansion in the reactive specimens occurred quickly in the first 90 days of testing, subsequently slowed down, and ultimately plateaued after 210 days. Final expansion measurements for the reactive specimens at 28, 90, 180 and 365 days are 0.019%, 0.168%, 0.203%, and 0.229%, respectively (Figure 9 and TABLE III). Length expansion in the nonreactive specimens occurred relatively slowly and gradually throughout 365 days, though the majority of the expansion occurred in the first 90 days and expansion generally plateaued after 150 days. The final expansion measurements for the nonreactive specimens at 28, 90, 180 and 365 days were an order of magnitude less than the expansions values of the reactive specimens, measuring 0.005%, 0.014%, 0.017%, and 0.014%, respectively with age (Figure 10 and TABLE IV). Specimen NRA-180 expanded the most out of the nonreactive specimens, surpassing the other three specimens including Specimen NRA-365 which was tested even longer. The cause of greater expansion in this one specimen in unknown; it is possible that this specimen contained more reactive particles than the other by random distribution.

Results of ASTM C1293 testing also show a relatively significant degree of positive mass change in the reactive specimens and fairly small degree of positive mass change in the

nonreactive specimens (Figure 11 and Figure 12). Mass measurements were not recorded on either the reactive or the nonreactive specimens during the first 28 days, and because of that, mass change measurements only represent change in mass which occurred from 35 to 365 days; mass change percentage at 35 days is zeroed (Figure 11 and TABLE V). Mass change in the reactive specimens occurred quickly in first 77 days and subsequently slowed down thereafter. The final mass change measurements for the reactive specimens at 90, 180 and 365 days were 0.938%, 1.319%, and 1.341%, respectively. Mass change in the nonreactive specimens occurred fairly gradually over time. The final mass change measurements for the nonreactive specimens at 90, 180 and 365 days were 0.262%, 0.339%, and 0.465%, respectively (Figure 12 and TABLE VI).

Length expansion and mass change values were normalized to the greatest extent of expansion and mass change observed in the reactive (RA) specimens. Nonreactive specimens only expanded 6.11% of the measured expansion of the reactive specimens. Nonreactive specimens also only exhibited 34.69% of the positive mass change the reactive specimens were measured at 365 days. Figure 13 displays the length expansion relationship between the normalized values of the reactive and nonreactive specimens over time, and Figure 14 displays the mass change relationship between the reactive and nonreactive specimens over time. Corresponding data is presented in TABLE VII.

The observed amount of expansion and mass change among the reactive and nonreactive specimens was expected. Because the reactive fine aggregate is known to be particularly fast-reacting, the substantial amount of expansion observed in the first 90 days was anticipated. At the point of which expansion and positive mass change values plateau, it is assumed the majority of the reaction has been exhausted. Because alkalis and moisture are being fed into the system, it is assumed that the amount of reactive silica has been exhausted, at least to a substantial enough degree that expansion is only slightly continuing and positive mass change is due to a small degree of hydration. What is noteworthy, however, is that reaction plateaus at 210 days in reactive specimens and at 150 days in nonreactive specimens.

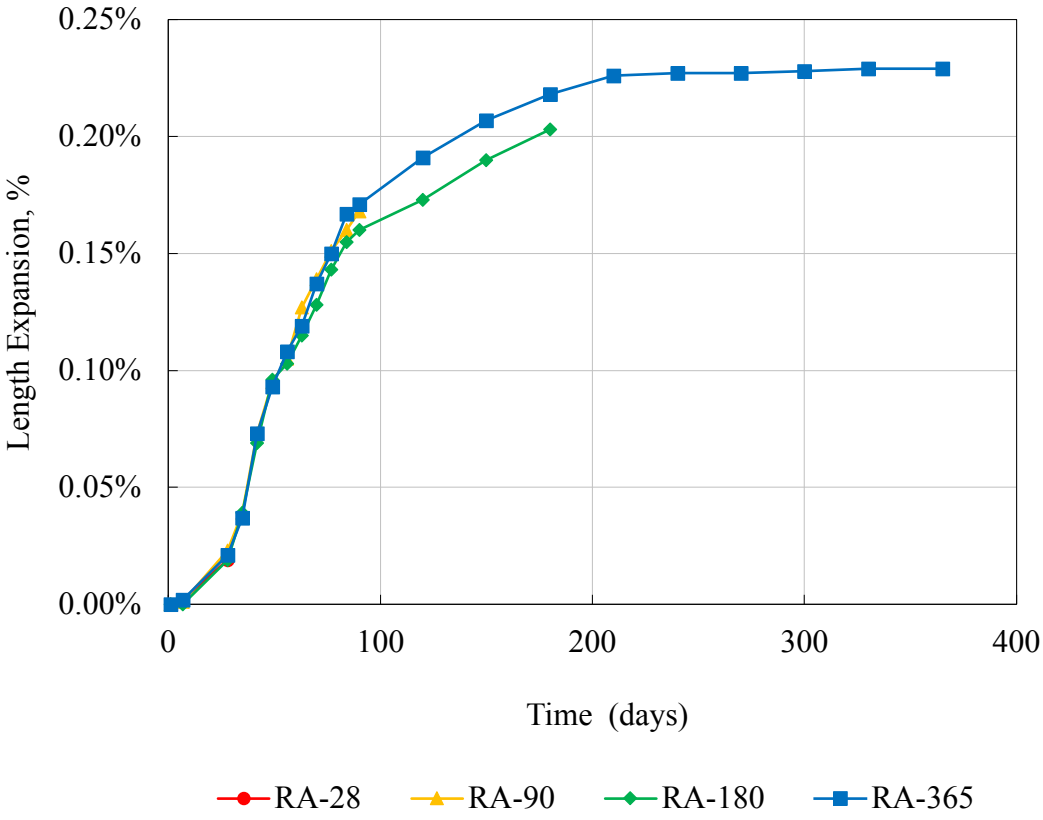

Figure 9 Length expansion of RA specimens

TABLE III LENGTH EXPANSION OF RA SPECIMENS

Time (days)	Length Expansion (%)					
	RA-28	RA-90	RA-180	RA-365	Average	Normalized Average
1	0.000%	0.000%	0.000%	0.000%	0.000%	0.00%
7	0.002%	0.001%	0.000%	0.002%	0.001%	0.55%
28	0.019%	0.023%	0.019%	0.021%	0.021%	8.95%
35		0.039%	0.039%	0.037%	0.038%	16.74%
42		0.073%	0.069%	0.073%	0.072%	31.30%
49		0.095%	0.096%	0.093%	0.095%	41.34%
56		0.105%	0.103%	0.108%	0.105%	46.00%
63		0.127%	0.115%	0.119%	0.120%	52.55%
70		0.139%	0.128%	0.137%	0.135%	58.81%
77		0.151%	0.143%	0.150%	0.148%	64.63%
84		0.160%	0.155%	0.167%	0.161%	70.16%
90		0.168%	0.160%	0.171%	0.166%	72.63%
120			0.173%	0.191%	0.182%	79.48%
150			0.190%	0.207%	0.199%	86.68%
180			0.203%	0.218%	0.211%	91.92%
210				0.226%	0.226%	98.69%
240				0.227%	0.227%	99.13%
270				0.227%	0.227%	99.13%
300				0.228%	0.228%	99.56%
330				0.229%	0.229%	100.00%
365				0.229%	0.229%	100.00%

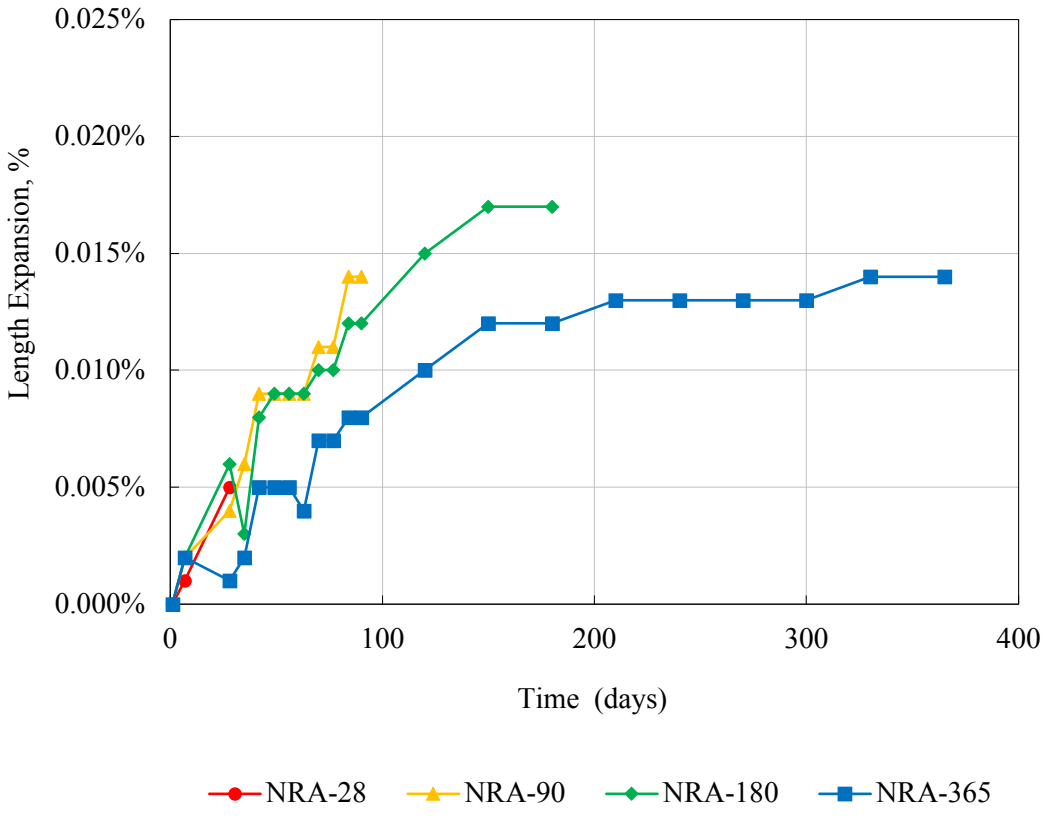

Figure 10 Length expansion of NRA specimens

TABLE IV LENGTH EXPANSION OF NRA SPECIMENS

Time (days)	Length Expansion (%)					
	NRA-28	NRA-90	NRA-180	NRA-365	Average	Normalized Average
1	0.000%	0.000%	0.000%	0.000%	0.000%	0.00%
7	0.001%	0.002%	0.002%	0.002%	0.002%	0.76%
28	0.005%	0.004%	0.006%	0.001%	0.004%	1.75%
35		0.006%	0.003%	0.002%	0.004%	1.60%
42		0.009%	0.008%	0.005%	0.007%	3.20%
49		0.009%	0.009%	0.005%	0.008%	3.35%
56		0.009%	0.009%	0.005%	0.008%	3.35%
63		0.009%	0.009%	0.004%	0.007%	3.20%
70		0.011%	0.010%	0.007%	0.009%	4.08%
77		0.011%	0.010%	0.007%	0.009%	4.08%
84		0.014%	0.012%	0.008%	0.011%	4.95%
90		0.014%	0.012%	0.008%	0.011%	4.95%
120			0.015%	0.010%	0.013%	5.46%
150			0.017%	0.012%	0.015%	6.33%
180			0.017%	0.012%	0.015%	6.33%
210				0.013%	0.013%	5.68%
240				0.013%	0.013%	5.68%
270				0.013%	0.013%	5.68%
300				0.013%	0.013%	5.68%
330				0.014%	0.014%	6.11%
365				0.014%	0.014%	6.11%

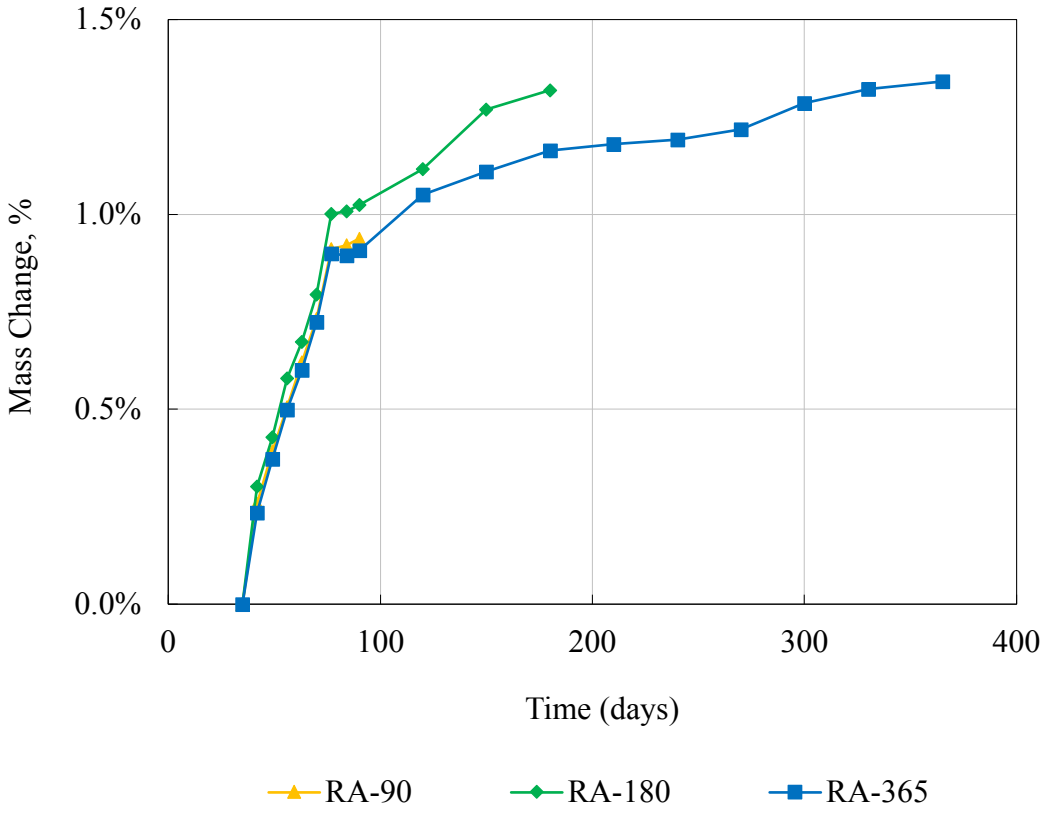

Figure 11 Mass change of RA specimens

TABLE V MASS CHANGE OF RA SPECIMENS

Time (days)	Mass Change (%)					
	RA-28	RA-90	RA-180	RA-365	Average	Normalized Average
1						
7						
28						
35		0.000%	0.000%	0.000%	0.000%	0.00%
42		0.258%	0.303%	0.234%	0.265%	19.75%
49		0.393%	0.429%	0.373%	0.398%	29.69%
56		0.505%	0.580%	0.499%	0.528%	39.38%
63		0.620%	0.673%	0.600%	0.631%	47.06%
70		0.733%	0.794%	0.724%	0.750%	55.94%
77		0.910%	1.001%	0.900%	0.937%	69.88%
84		0.920%	1.009%	0.895%	0.941%	70.19%
90		0.938%	1.024%	0.908%	0.956%	71.31%
120			1.117%	1.051%	1.084%	80.84%
150			1.269%	1.109%	1.189%	88.64%
180			1.319%	1.165%	1.242%	92.59%
210				1.180%	1.180%	87.97%
240				1.192%	1.192%	88.91%
270				1.218%	1.218%	90.79%
300				1.286%	1.286%	95.86%
330				1.321%	1.321%	98.50%
365				1.341%	1.341%	100.00%

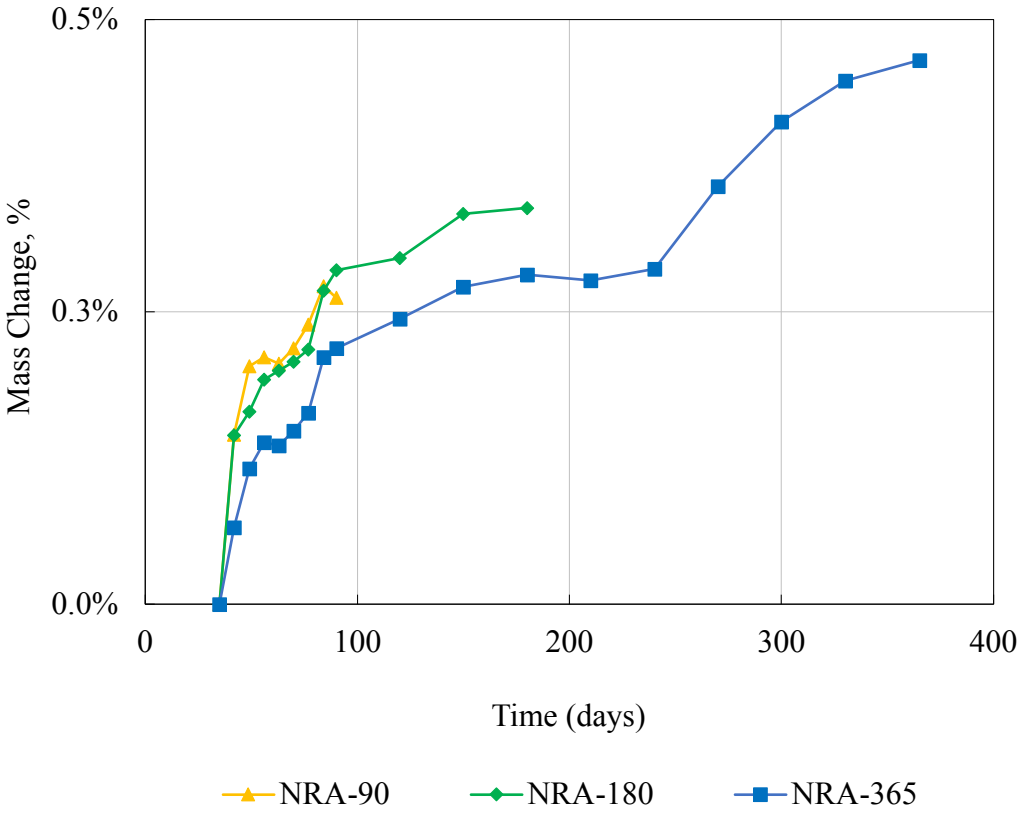

Figure 12 Mass change of NRA specimens

TABLE VI MASS CHANGE OF NRA SPECIMENS

Time (days)	Mass Change (%)					
	NRA-28	NRA-90	NRA-180	NRA-365	Average	Normalized Average
1						
7						
28						
35		0.000%	0.000%	0.000%	0.000%	0.00%
42		0.145%	0.144%	0.065%	0.118%	8.81%
49		0.203%	0.164%	0.116%	0.161%	12.02%
56		0.211%	0.192%	0.138%	0.181%	13.46%
63		0.206%	0.200%	0.136%	0.181%	13.46%
70		0.219%	0.207%	0.148%	0.192%	14.28%
77		0.239%	0.218%	0.163%	0.207%	15.41%
84		0.272%	0.268%	0.211%	0.251%	18.68%
90		0.262%	0.286%	0.219%	0.256%	19.05%
120			0.296%	0.244%	0.270%	20.13%
150			0.334%	0.272%	0.303%	22.57%
180			0.339%	0.282%	0.310%	23.14%
210				0.277%	0.277%	20.63%
240				0.287%	0.287%	21.38%
270				0.357%	0.357%	26.63%
300				0.412%	0.412%	30.75%
330				0.448%	0.448%	33.38%
365				0.465%	0.465%	34.69%

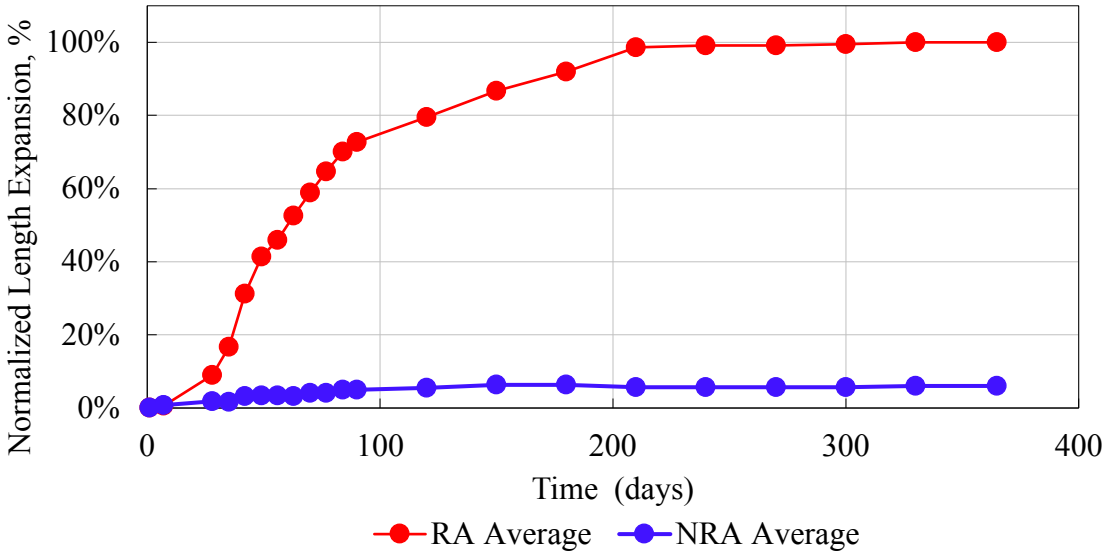

Figure 13 Normalized length expansion over time

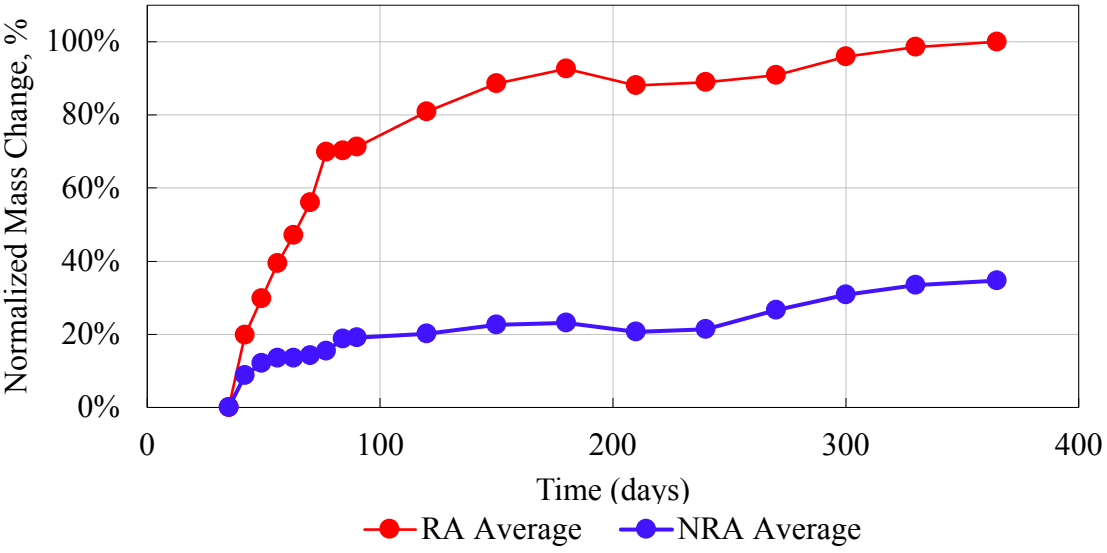

Figure 14 Normalized mass change over time

TABLE VII NORMALIZED EXPANSION AND MASS CHANGE

Time (days)	Normalized Expansion (%)		Normalized Mass Change (%)	
	RA	NRA	RA	NRA
1	0.00%	0.00%	-	-
7	0.55%	0.76%	-	-
28	8.95%	1.75%	-	-
35	16.74%	1.60%	0.00%	0.00%
42	31.30%	1.75%	19.75%	8.81%
49	41.34%	3.35%	29.69%	12.02%
56	46.00%	3.35%	39.38%	13.46%
63	52.55%	3.20%	47.06%	13.46%
70	58.81%	4.08%	55.94%	14.28%
77	64.63%	4.08%	69.88%	15.41%
84	70.16%	4.95%	70.19%	18.68%
90	72.63%	4.95%	71.31%	19.05%
120	79.48%	5.46%	80.84%	20.13%
150	86.68%	6.33%	88.64%	22.57%
180	91.92%	6.33%	92.59%	23.14%
210	98.69%	5.68%	87.97%	20.63%
240	99.13%	5.68%	88.91%	21.38%
270	99.13%	5.68%	90.79%	26.63%
300	99.56%	5.68%	95.86%	30.75%
330	100.00%	6.11%	98.50%	33.38%
365	100.00%	6.11%	100.00%	34.69%

B. Electrical Impedance Spectroscopy

Measured real impedance (Z') and imaginary impedance (Z") values for reactive (RA) and nonreactive (NRA) specimens yielded differentiating results. Nyquist diagrams, which plot real impedance against imaginary impedance, were used to compare impedance results. Reactive specimens in ambient air measured smaller real impedance values and larger imaginary impedance values than nonreactive specimens in ambient air (Figure 15, Figure 16, Figure 17). In reactive specimens conditioned in ambient air, real impedance values ranged from 6,450 to 8,290 Ohms and imaginary impedance values ranged from -3,150 to -499 Ohms. In nonreactive specimens conditioned in ambient air, real impedance values ranged from 19,100 to 24,900 Ohms and imaginary impedance values ranged from -12,000 to -1,110 Ohms. Saturated reactive specimens measured smaller real impedance values and larger imaginary impedance values than nonreactive specimens, except for Specimen NRA-28 (Figure 18, Figure 19, Figure 20); impedance values for Specimen NRA-28 and Specimen RA-365 overlap. In saturated reactive specimens, real impedance values range from 4820 to 7290 Ohms and imaginary impedance values range from -1,080 to -254 Ohms. In saturated nonreactive specimens, real impedance values range from 9,060 to 12,400 Ohms and imaginary impedance values range from -9,620 to -680 Ohms. Reactive specimens in ambient air and saturated conditions exhibit a much smaller range of both real and imaginary impedance values than that of nonreactive specimens in ambient air and saturated conditions. The difference in both real and imaginary impedance ranges is observable in the provided Nyquist diagrams.

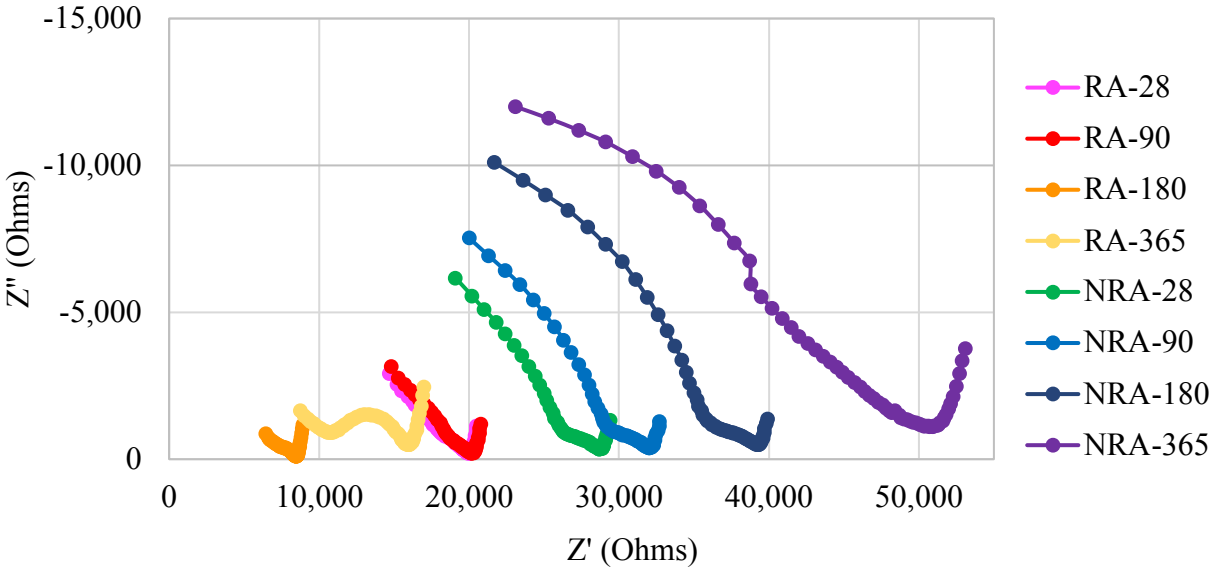

Figure 15 Nyquist diagram of specimens in ambient air condition

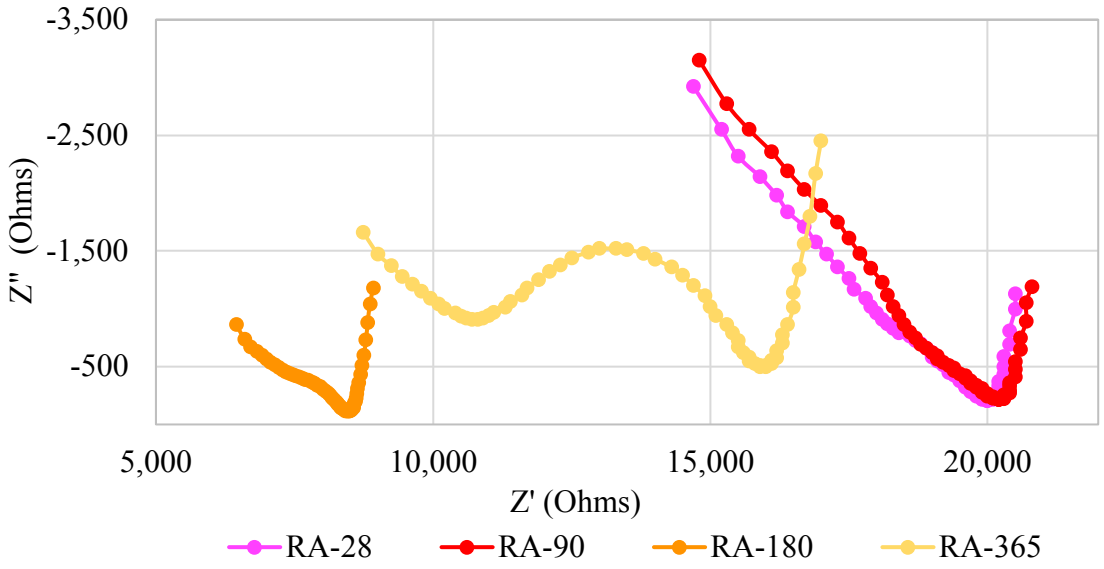

Figure 16 Nyquist diagram of RA specimens in ambient air condition

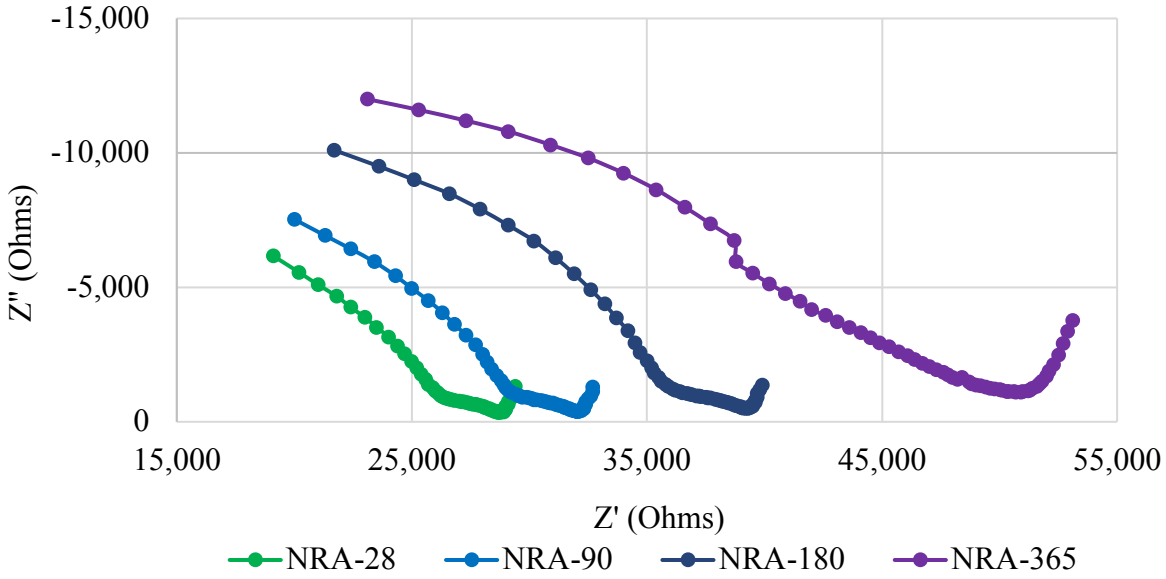

Figure 17 Nyquist diagram of NRA specimens in ambient air condition

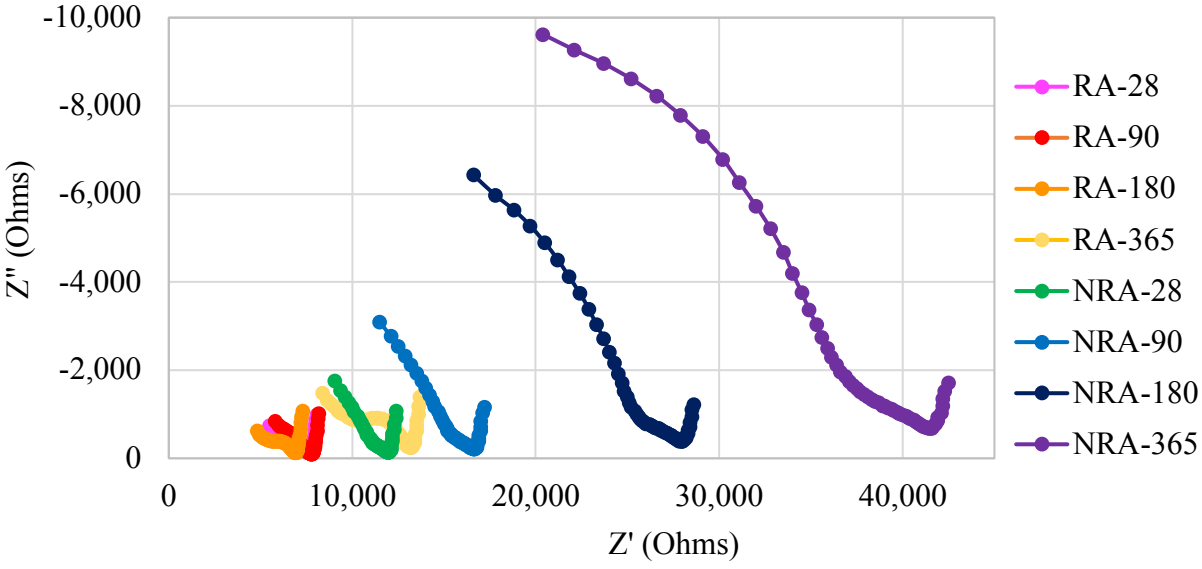

Figure 18 Nyquist diagram of specimens in saturated condition

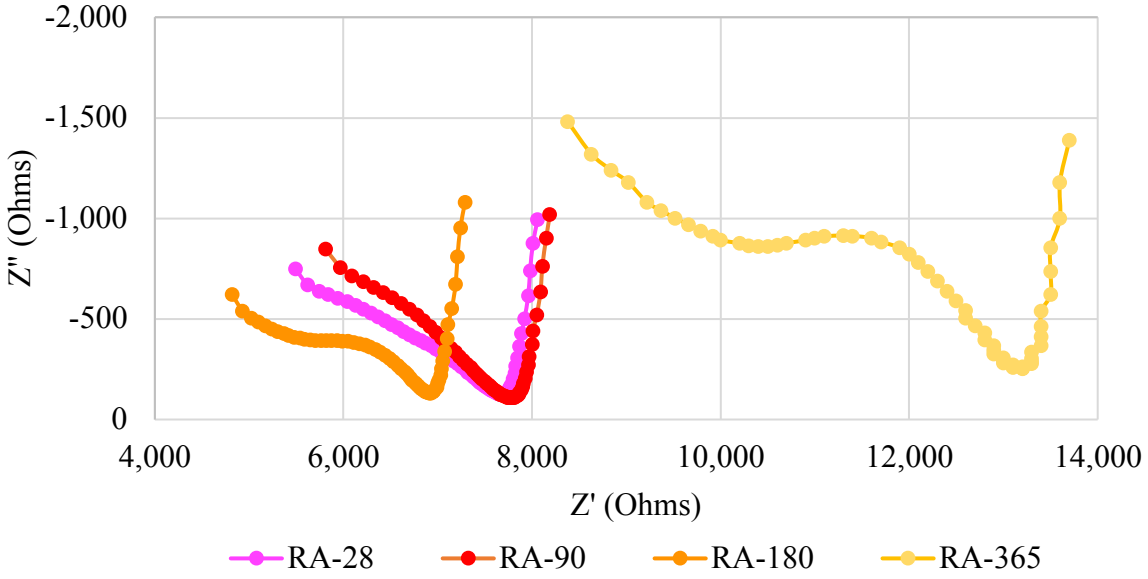

Figure 19 Nyquist diagram of RA specimens in saturated condition

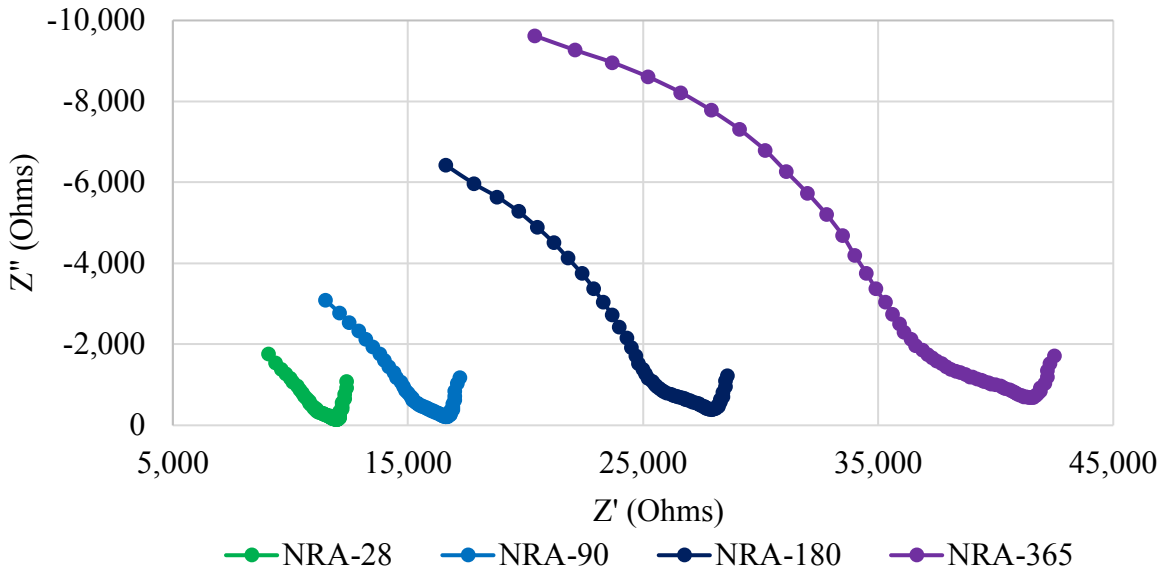

Figure 20 Nyquist diagram of NRA specimens in saturated condition

As observed in Nyquist diagrams in Figure 15 and Figure 18, real impedance values and range of impedance values become smaller moving from right to left along the x-axis and from high to low along the y-axis, except in the case of RA-365. Imaginary impedance values become larger moving from right to left along the x-axis. In both ambient air and saturated conditions, nonreactive specimens exhibit increasing real impedance values with time, whereas reactive specimens exhibit decreasing real impedance values with time, excluding RA-365. RA-365 plots between that of RA-180 and the other two reactive specimens, RA-28 and RA-90, and exhibits a more noticeable double parabola-like curve with two inflection points. Also, in both ambient air and saturated conditions, RA-28 and RA-90 have very similar impedance values which overlap. In ambient air, RA-28 and RA-90 impedance values are much different than RA-180 and RA-365 impedance values. In saturated conditions, only RA-365 impedance values appear much different and RA-28, RA-90, and RA-180 are very similar. Also, in saturated conditions, NRA-28 and NRA-90 impedance values slightly overlap. Overall, the gradually increasing impedance with time trend observed in nonreactive specimens is not observed in the reactive specimens impedance values; the opposite is observed, with the exception of RA-365.

Because real impedance corresponds to resistance and imaginary impedance corresponds to capacitance and inductance, it is reasonable to assume that reactive specimens are better conductors due to their smaller resistance values and that reactive specimens are able to store less energy due to their larger capacitance values compared to nonreactive specimens. In reactive specimens, real impedance values decrease with time, excluding RA-365. On the contrary,

nonreactive specimens exhibit increasing real impedance with time. These findings likely correlate to the availability of moisture within the system; moisture in reactive specimens is increasingly absorbed by ASR gel formation and moisture in nonreactive specimens builds up due to the feeding of moisture into the system through ASTM C1293 testing in conjunction with the lack of ASR gel formation due to the presence of fly ash retarding the reaction. The distinguishing double parabola impedance curve for Specimen RA-365 is curious, but likely due to the degree of ASR occurring within the specimen or change in available moisture.

Bode plots, which plot real against frequency on a log-log scale, are also used in this study to compare impedance results as well as to present visual comparisons between sets of specimens. Imaginary impedance values are plotted against frequency too. When all specimens are plotted together, it is difficult to distinguish differences (Figure 21 and Figure 22). However, when impedance values are plotted by condition (ambient air and saturated), clear differences are observed. In ambient air conditions, reactive specimens exhibit smaller real impedance and much larger imaginary impedance than nonreactive specimens at a frequency sweep of 0.1 to 150,000 Hz (Figure 23 and Figure 24). In saturated conditions, reactive specimens exhibit smaller real impedance values and much larger imaginary impedance than nonreactive specimens with the same frequency sweep, except in the case of overlapping impedance values of Specimens RA-365 and NRA-28 (Figure 25 and Figure 26).

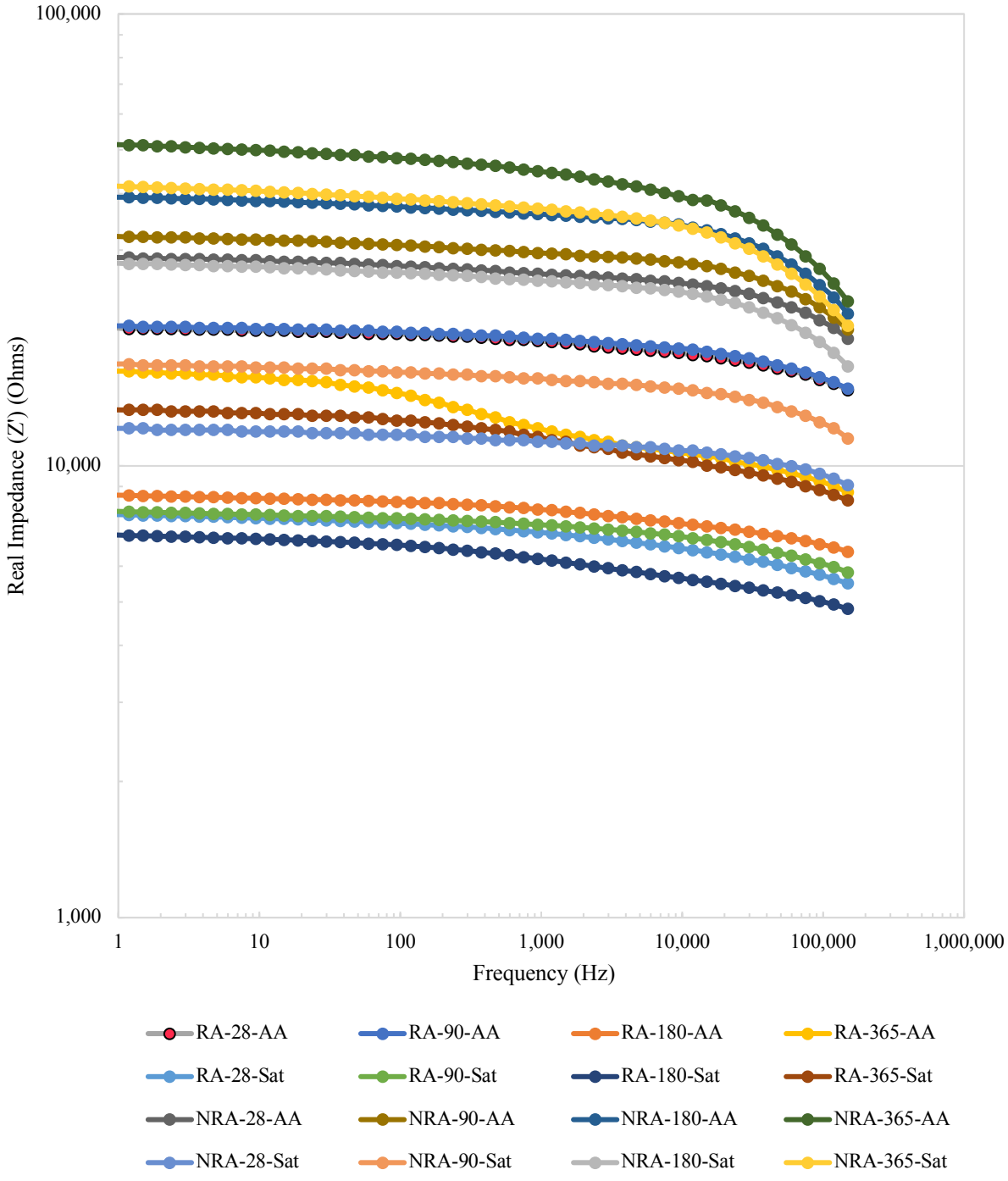

Figure 21 Log-log plot of real impedance (Z') in Ohms vs. frequency in Hz for all specimens

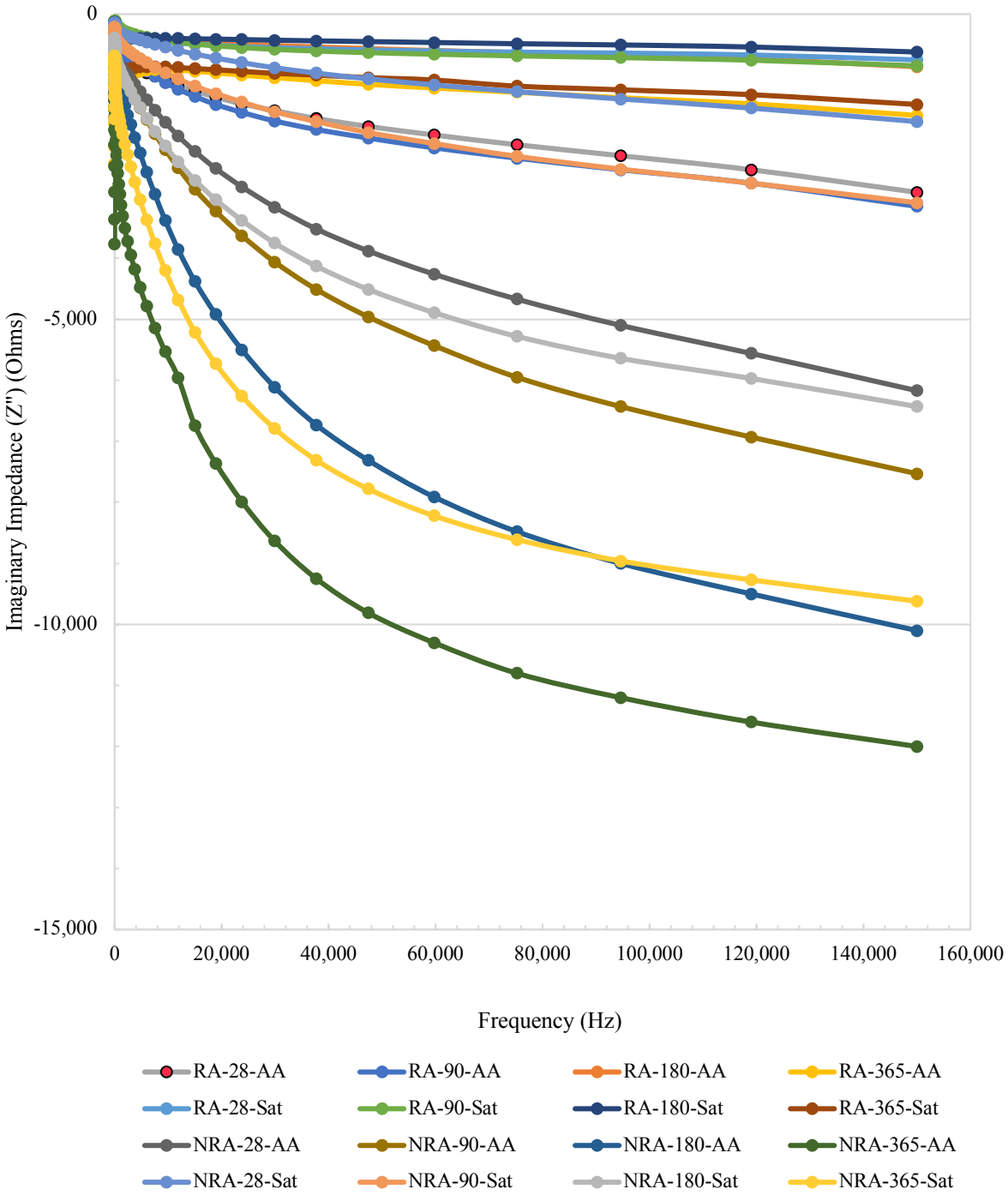

Figure 22 Imaginary impedance (Z") in Ohms vs. frequency in Hz for all specimens

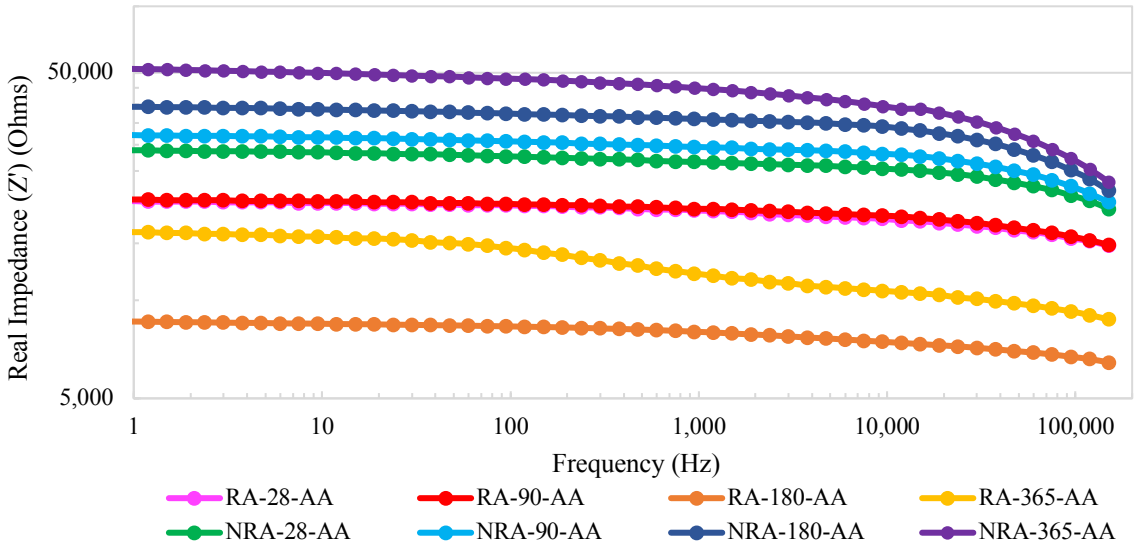

Figure 23 Log-log plot of real impedance (Z') in Ohms vs. frequency in Hz for specimens in ambient air condition

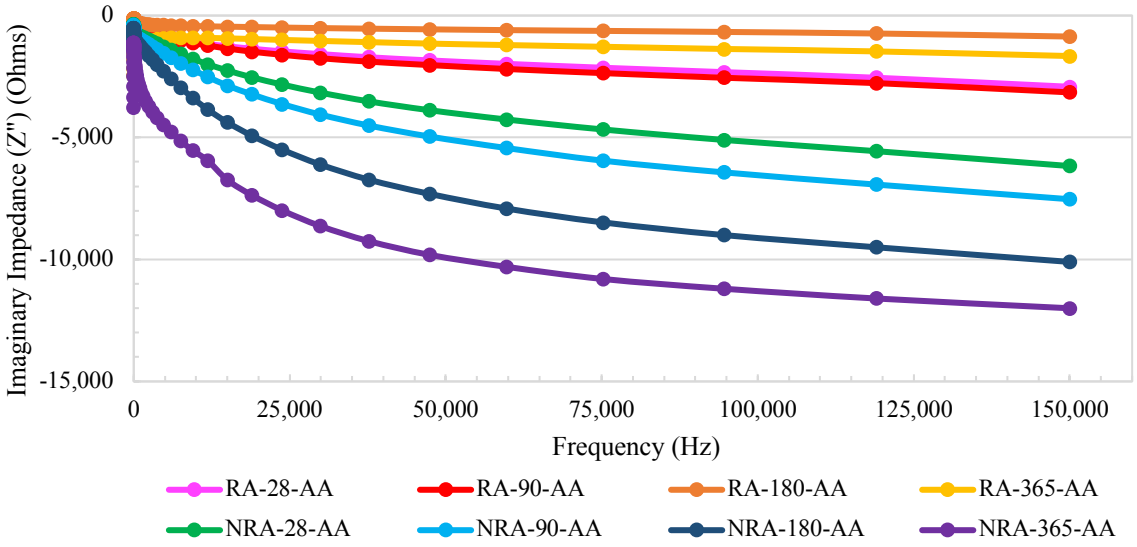

Figure 24 Imaginary impedance (Z") in Ohms vs. frequency in Hz for specimens in ambient air condition

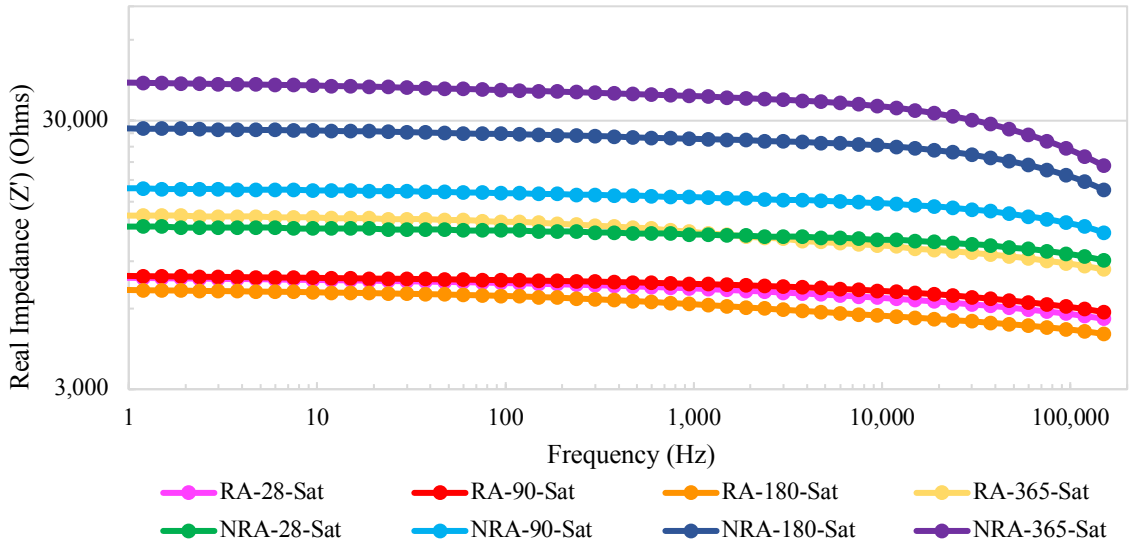

Figure 25 Log-log plot of real impedance (Z') in Ohms vs. frequency in Hz for specimens in saturated condition

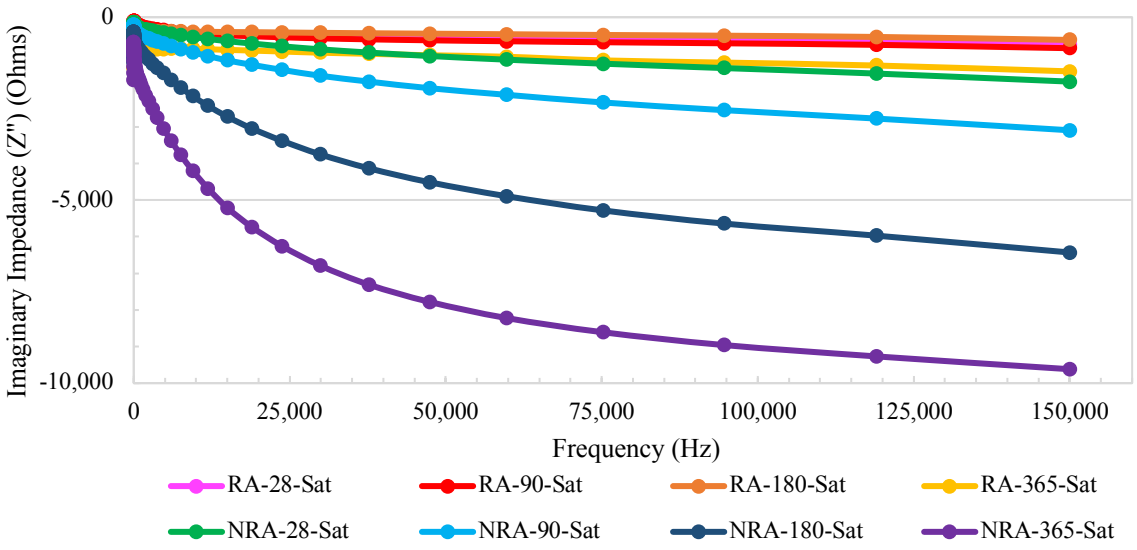

Figure 26 Imaginary impedance (Z") in Ohms vs. frequency in Hz for specimens in saturated condition

Bulk resistance, denoted as the inflection point in Nyquist diagrams (Figure 15 to Figure 20), is greater in ambient air than in saturated conditions for both reactive and nonreactive specimens (TABLE VIII and TABLE IX). Bulk resistance in both reactive and nonreactive specimens generally increases with time in both ambient air and saturated conditions, although an isolated decrease in bulk resistance is observed at 180 days in ambient air and saturated reactive specimens (Figure 27). The bulk resistance recovers in these two reactive specimens, ultimately at a bulk resistance greater than previous measurements. The decrease in bulk resistance at 180 days is curious and later correlated to microwave testing dielectric constant and water volume fraction testing as well as results of petrographic examination and DRI testing, both discussed later in this report.

Bulk resistance is considered a more reliable measure of impedance than real and imaginary impedance values on their own [14]. Bulk resistance values are greater in ambient air condition than in saturated conditions, suggesting that specimens are better conductors in saturated condition. However, bulk resistance and changes in bulk resistance were still measurable in ambient air conditions. This is important because practical use of EIS in the field will require testing of in-situ concrete structures in ambient conditions.

TABLE VIII BULK RESISTANCE FOR SPECIMENS IN AMBIENT AIR CONDITION

Impedance Data for Specimens in Ambient Air Condition		
Specimen	Bulk Resistance (Ohms)	Normalized
RA-28	14,700	0.86
RA-90	14,800	0.87
RA-180	8,920	0.52
RA-365	17,000	1.00
NRA-28	19,100	0.83
NRA-90	20,000	0.87
NRA-180	21,700	0.94
NRA-365	23,100	1.00

TABLE IX BULK RESISTANCE FOR SPECIMENS IN SATURATED CONDITION

Impedance Data for Specimens in Saturated Condition		
Specimen	Bulk Resistance (Ohms)	Normalized
RA-28	8,060	0.96
RA-90	8,190	0.98
RA-180	7,290	0.87
RA-365	8,380	1.00
NRA-28	9,060	0.44
NRA-90	11,500	0.56
NRA-180	16,600	0.81
NRA-365	20,400	1.00

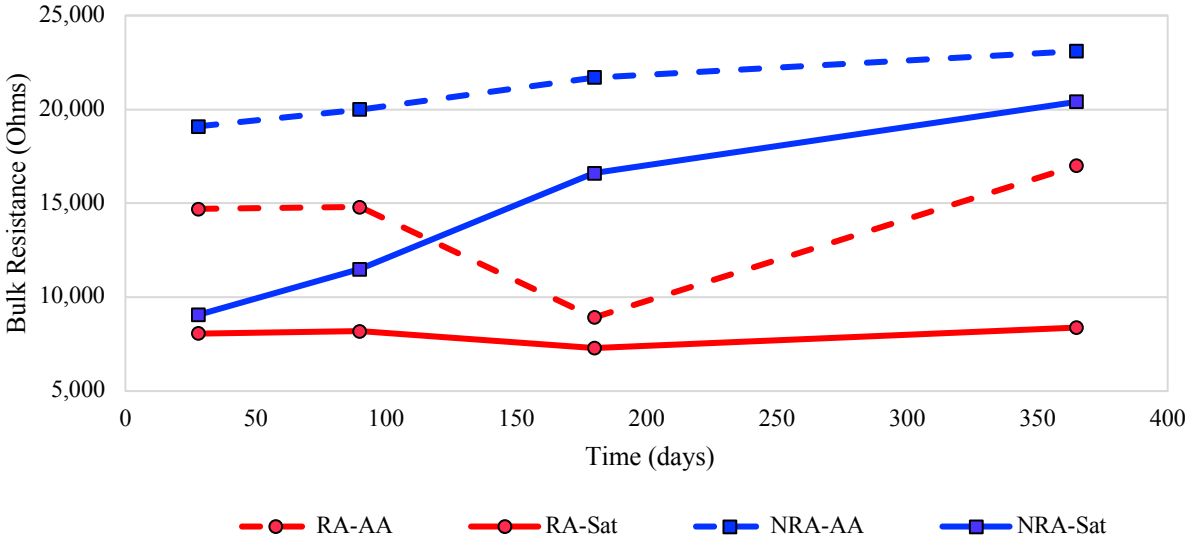

Figure 27 Bulk resistance of specimens in ambient air and saturated condition

C. Microwave Results

Microwave testing on reactive and nonreactive specimens in ambient air, saturated and dry conditions provided reflection coefficient (S_{11}) measurements which were used to calculate dielectric constant (Equation 1), a parameter which measures a materials ability to store energy similar to imaginary impedance. The water volume fraction of the cementitious paste within the specimens was also measured using both calculated dielectric constant values from different conditions and the known dielectric constant value of water (Equation 2).

$$Dielectric\ constant\ (\varepsilon) = \left(\frac{1+S_{11}}{1-S_{11}}\right)^2 \qquad \text{(Equation 1)}$$

$$Water\ volume\ fraction\ (f_W) = \frac{\varepsilon_w + 2\varepsilon_c}{\varepsilon_w - \varepsilon_c} \times \frac{\varepsilon_{eff} - \varepsilon_c}{\varepsilon_{eff} + 2\varepsilon_c} \quad \text{(Equation 2)}$$

$$\varepsilon_c = dry\ dielectric\ constant$$

$$\varepsilon_{eff} = saturated\ dielectric\ constant$$

$$\varepsilon_w = known\ dielectric\ constant\ of\ water$$

Reactive dielectric constant values are smaller than nonreactive dielectric constant values in saturated and ambient air conditions, and reactive dielectric constant values are larger than nonreactive dielectric constant values in dry condition. Dielectric constant values do not correlate to imaginary impedance values, which are supposed to be comparable in regards to capacitance.

Dielectric constant values increase from 28 to 180 days, then decrease between 180 and 365 days for both reactive and nonreactive specimens in all three conditions. Dielectric constant values have smaller ranges in reactive specimens than in nonreactive specimens. In both reactive and nonreactive specimens, dielectric constant values were highest in saturated condition, followed by ambient air, and then dry condition (Figure 28). Dielectric constant values for nonreactive ambient air specimens overlap with dielectric constant values of reactive ambient air and saturated specimens (Figure 28). Dielectric constant values are presented for reactive and nonreactive specimens separately in Figure 29 and Figure 30, respectively. The greatest change in dielectric constant values was observed in reactive and nonreactive dry specimens from 90 to

180 days (substantial positive change) and from 180 to 365 days (substantial negative change), followed by a relatively moderate positive and negative change in ambient air specimens, and then the smallest amount of change in saturated specimens (Figure 31). Dielectric constant values are presented in TABLE X.

Both the increasing trend of dielectric values in the first 180 days as well as the subsequent decreasing trend after 180 days are interesting. Both bulk resistance and dielectric constant values decreased at 180 days and length expansion and mass change values plateau at 180 days, suggesting the possibility of some sort of phenomenon is occurring at this time interval; these results are later correlated to petrographic examination and DRI testing results, as well as water volume fraction discussed in this section. Figure 31 shows that the greatest change in dielectric constant values occurs at the 180 day mark in all specimens, not just the reactive specimens.

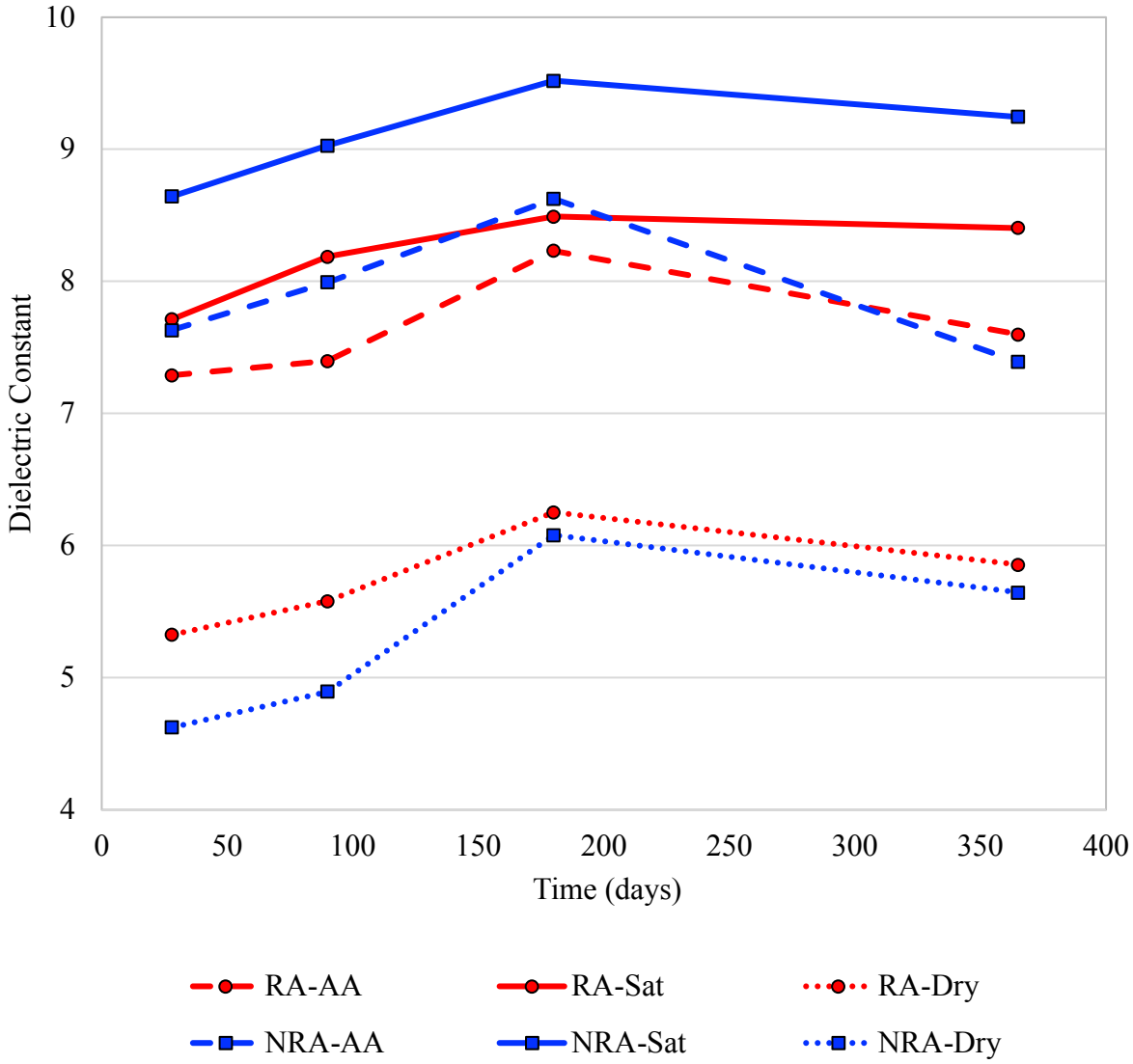

Figure 28 Dielectric constant of all specimens over time

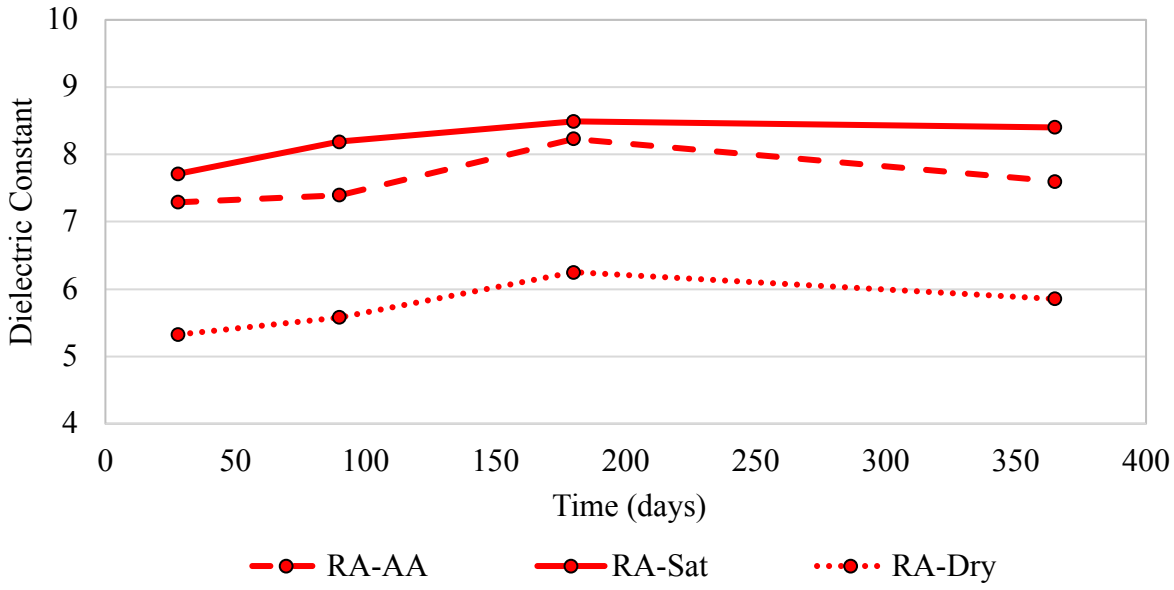

Figure 29 Dielectric constant of RA specimens

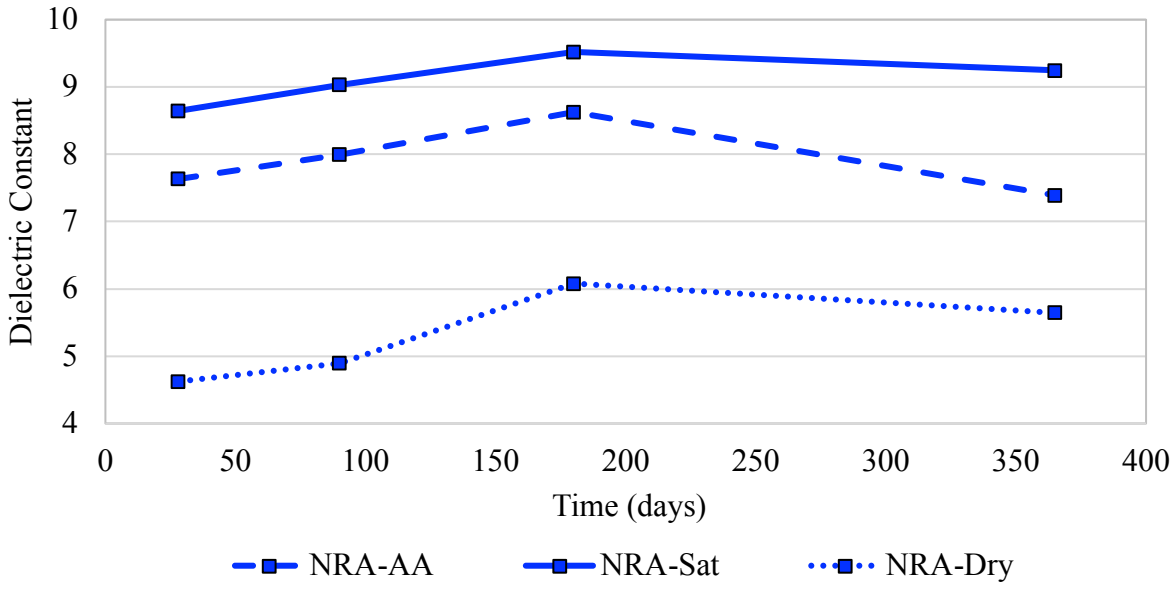

Figure 30 Dielectric constant of NRA specimens

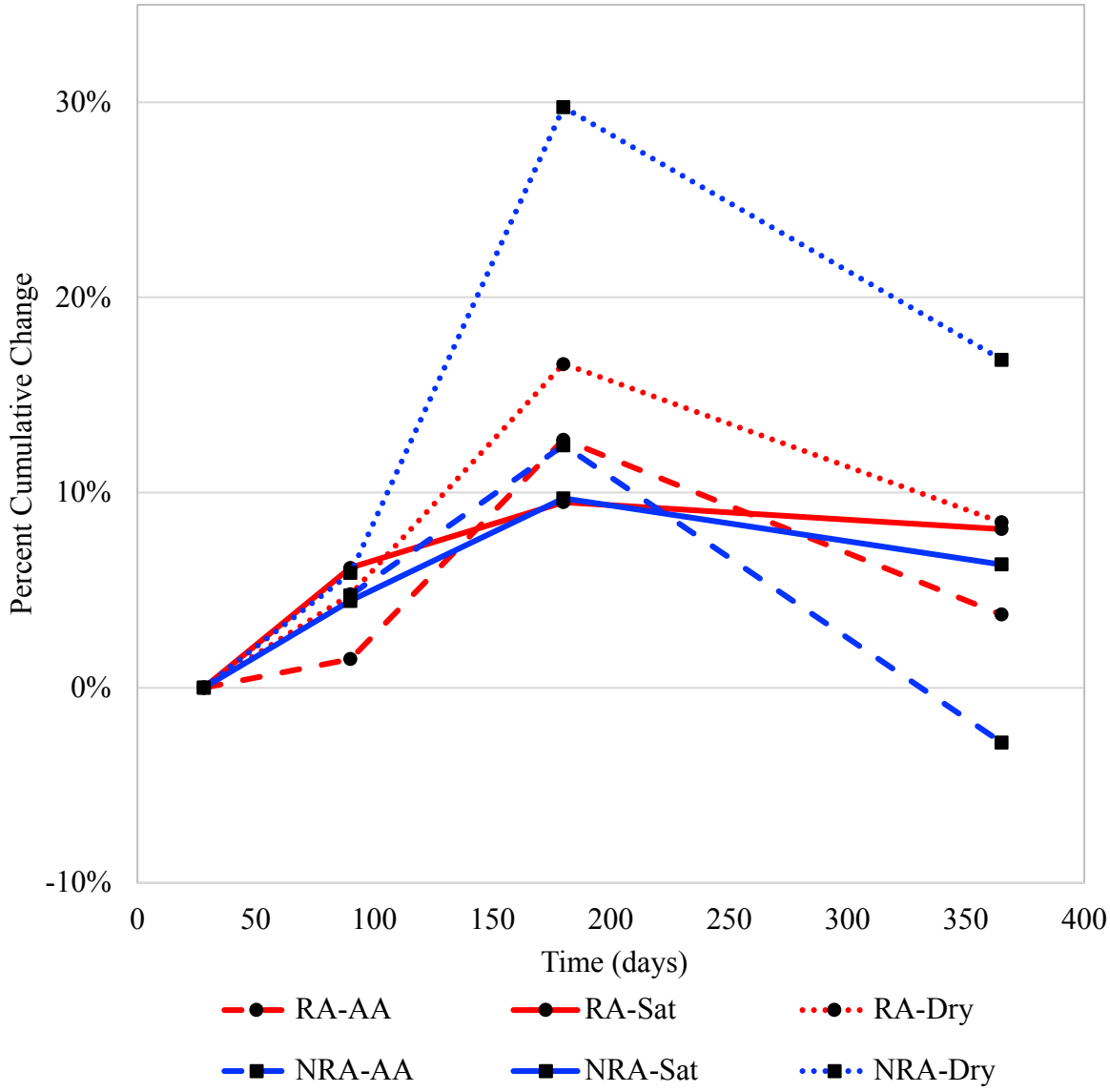

Figure 31 Percent cumulative change in dielectric constant

TABLE X DIELECTRIC CONSTANT IN VARYING CONDITIONS

Dielectric Constant in Varying Conditions						
Specimen	Surface B	Surface C	Surface D	*Avg. of Surfaces*	*Cum. Change*	*% Cum. Change*
Dielectric Constant in Ambient Air Condition						
RA-28	7.16	7.09	7.61	7.29	-	-
RA-90	7.46	7.35	7.38	7.40	0.11	1.5%
RA-180	8.02	8.49	8.19	8.23	0.94	12.7%
RA-365	7.06	8.36	7.38	7.60	0.31	3.8%
NRA-28	6.99	8.06	7.85	7.63	-	
NRA-90	7.31	8.36	8.31	7.99	0.36	4.7%
NRA-180	8.63	8.67	8.58	8.63	0.99	12.4%
NRA-365	6.85	8.81	6.51	7.39	-0.24	-2.8%
Dielectric Constant in Saturated Condition						
RA-28	7.58	7.42	8.14	7.71	-	-
RA-90	7.98	8.45	8.14	8.19	0.47	6.2%
RA-180	8.36	8.67	8.45	8.49	0.78	9.5%
RA-365	8.49	8.19	8.54	8.40	0.69	8.1%
NRA-28	7.54	9.39	9.00	8.64	-	-
NRA-90	7.98	9.92	9.19	9.03	0.39	4.5%
NRA-180	9.34	9.97	9.24	9.52	0.88	9.7%
NRA-365	9.24	9.05	9.45	9.25	0.60	6.3%
Dielectric Constant in Dry Condition						
RA-28	5.24	5.32	5.42	5.33	-	-
RA-90	5.39	5.88	5.47	5.58	0.26	4.8%
RA-180	6.55	6.39	5.82	6.25	0.93	16.6%
RA-365	5.63	6.17	5.77	5.86	0.53	8.5%
NRA-28	4.41	5.02	4.43	4.62	-	-
NRA-90	4.58	5.29	4.82	4.90	0.27	5.9%
NRA-180	5.71	6.68	5.85	6.08	1.46	29.7%
NRA-365	5.55	6.29	5.10	5.65	1.02	16.8%

The water volume fraction of the cementitious paste, measured using Equation 2, is substantially lower in reactive specimens compared to nonreactive specimens at all ages. The water volume fraction ranges from 0.13 to 0.17 in reactive specimens and 0.20 to 0.27 in nonreactive specimens (Figure 32 and TABLE XI). The cause of the substantially higher water volume fraction in NRA specimens is likely due to the fly ash replacement of cement in the mix design and its effect on cement hydration, compared to the RA specimens which contain only portland cement and no SCMs. More available moisture would theoretically be present in NRA specimens because a smaller amount of portland cement is used with the same amount of water in conjunction with fly ash, which has a relatively low ability to hydrate.

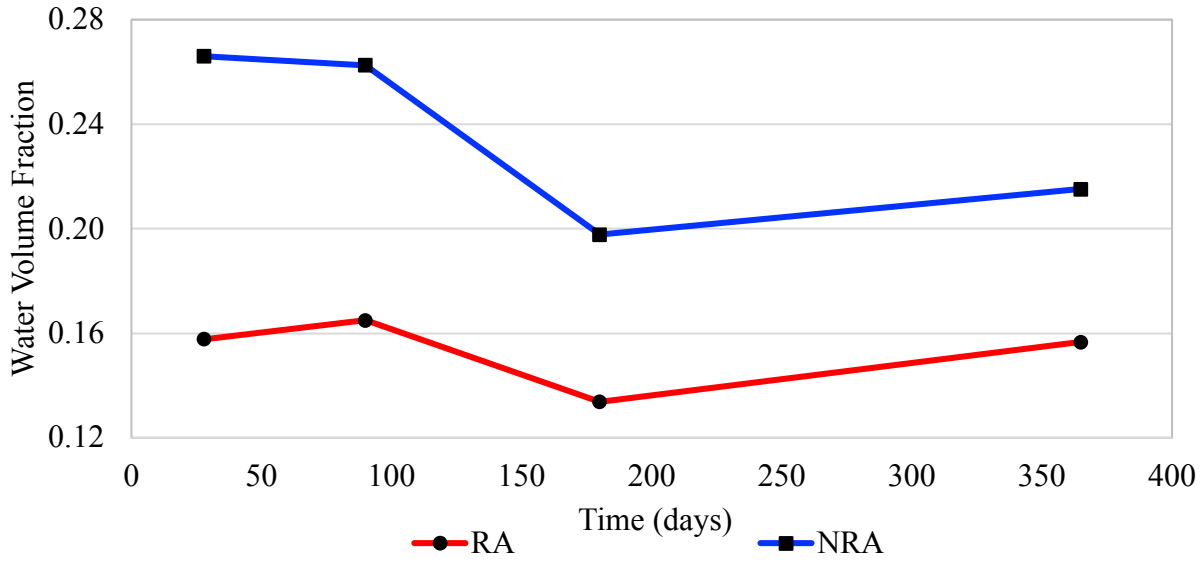

Figure 32 Water volume fraction (f_w) of RA and NRA specimens over time

Both reactive and nonreactive specimens exhibit highest values at 28 days (0.16 and 0.27), slightly different values at 90 days (0.17 and 0.26), substantially lower values at 180 days (0.13 and 0.20), and a final slight increase in values at 365 days (0.16 and 0.22) (TABLE XI). Other than the slight positive change of the reactive water volume fraction compared to the slight negative change of the nonreactive water volume fraction at 28 days, both reactive and nonreactive water volume fractions follow the same trend over time. The cause of slight change in water volume in the first 90 days is not known; however, the substantial decrease in water volume fraction from at 180 days likely corresponds to what is causing decreasing bulk resistance and dielectric constant at 180 days, too.

TABLE XI WATER VOLUME FRACTION (f_w) VARIABLES AND CALCULATIONS

Water Volume Fraction (f_w) using Maxwell-Garnet Equation				
Specimen	Dry DC (ε_c)	Saturated DC (ε_{eff})	Known ε_w	Calculated f_w
RA-28	5.33	7.71	80.1	0.16
RA-90	5.58	8.19	80.1	0.17
RA-180	6.25	8.49	80.1	0.13
RA-365	5.86	8.40	80.1	0.16
NRA-28	4.62	8.64	80.1	0.27
NRA-90	4.90	9.03	80.1	0.26
NRA-180	6.08	9.52	80.1	0.20
NRA-365	5.65	9.25	80.1	0.22
Note: DC = dielectric constant				

It is hypothesized that the water volume fraction is affected by ASR gel progression, particularly the absorption of available moisture during ASR gel formation. The cause of substantial decrease in water volume fraction at 180 days, based on the available data from this study, is likely due to ASR gel absorbing moisture. DRI results, discussed later in this paper, show that the amount of ASR gel rapidly increases from 180 to 365 days, correlating with the drastic decrease in water volume fraction results over the same time. The decrease in water volume fraction at 180 days could also be due, in part, to hydration of belite portland cement particles. Alite particles (C_3A) hydrate quickly, providing early strength, but belite particle (C_2A) hydrate later, providing strength gain later in the curing process. The cause of the slight increase in water volume fraction from 180 to 365 days is hypothesized to be due to the slowing down of the ASR process in conjunction with the with the constant rate of alkalis and moisture being fed into the system by ASTM C1293 testing. It is assumed that as the reaction slows down and is exhausted to some degree, the cementitious paste is able to continue hydration.

D. Petrographic Examination and DRI

The petrographic analysis evaluated qualitative amounts of deterioration features, such as microcracking, as well as identified the reactive aggregate rock types and paste condition; the majority of the analysis was conducted on the lapped surfaces of the specimens (Figure 33 and Figure 34). DRI testing relatively quantified the amount of several deterioration features in each sample including ASR gel, microcracks, debonded aggregate and combinations thereof. Both petrographic analysis and DRI results show a direct relationship between the amount of deterioration in each set of specimens with time; the amount of ASR-related deterioration observed in both the reactive and nonreactive specimens increases with extended ASTM C1293 testing. The amount of ASR-related deterioration is significantly greater in reactive specimens then nonreactive specimens, which was expected and specifically intended for this study.

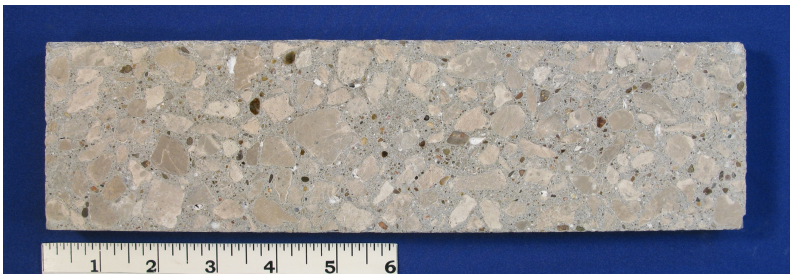

a) RA-28

b) RA-90

c) RA-180

d) RA-365

Figure 33 Lapped surfaces of RA specimens

a) NRA-28

b) NRA-90

c) NRA-180

d) NRA-365

Figure 34 Lapped surfaces of NRA specimens

For petrographic analysis, microcracks on the interior lapped surface of each specimen were traced in red ink for visual observation of microcracking on a macrolevel (Figure 35 and Figure 36). The amount of microcracks were qualitatively assessed using a descriptive scale which comprises of the following terminology a are commonly noted in routine petrographic examinations of hardened concrete in industry. Several ASR gel deposits are present in Specimen RA-365 (Figure 37, Figure 38, Figure 39). Thin-section analysis of the concrete in reactive specimen RA-365 and nonreactive specimen NRA-365 revealed several notable ASR gel deposits in RA-365 but none in NRA-365 (Figure 40, Figure 41, Figure 42).

Thin-section analysis is useful for identifying very small amounts of ASR gel and the source of reactive silica if not readily visible or apparent on a lapped concrete surface at high magnifications. Reactive rock types were identified through thin-section analysis. The alkali-reactive rock types present within the natural sand fine aggregate include chert, chalcedony, opaline particles, glassy volcanic particles, and quartz and quartzite exhibiting high optical strain.

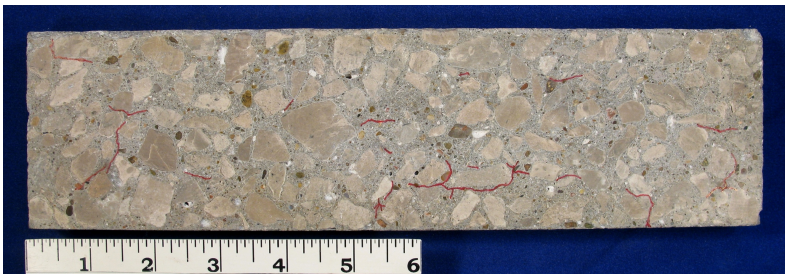

a) RA-28

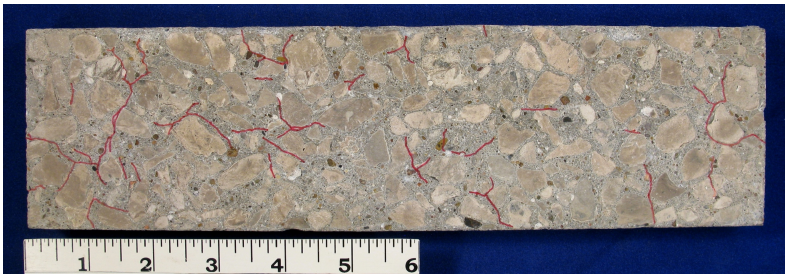

b) RA-90

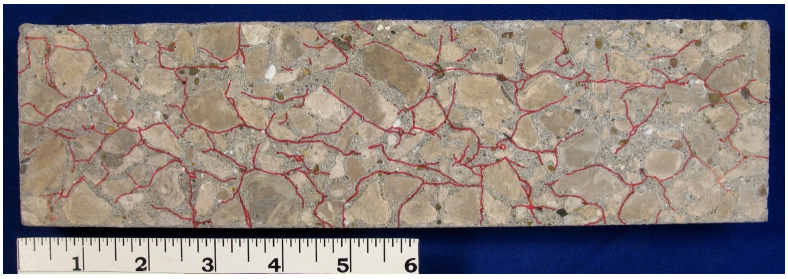

c) RA-180

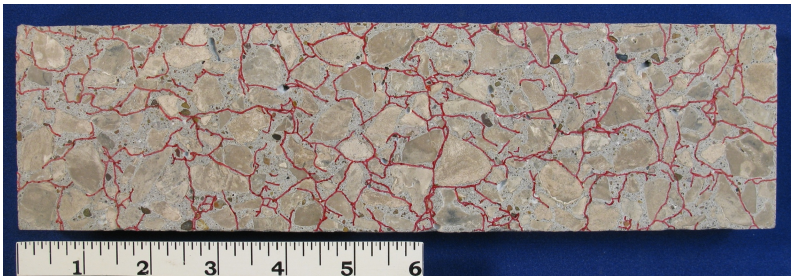

d) RA-365

Figure 35 Lapped surfaces of RA specimens with traced microcracks

a) NRA-28

b) NRA-90

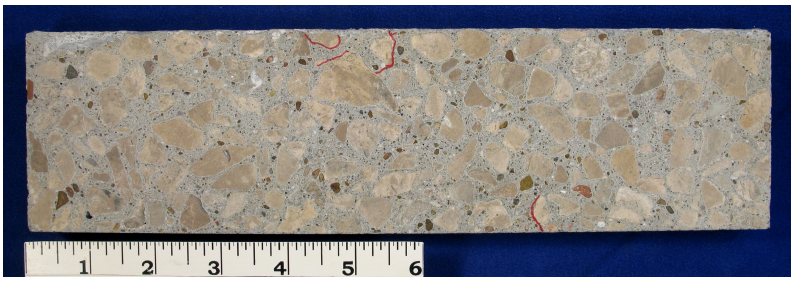

c) NRA-180

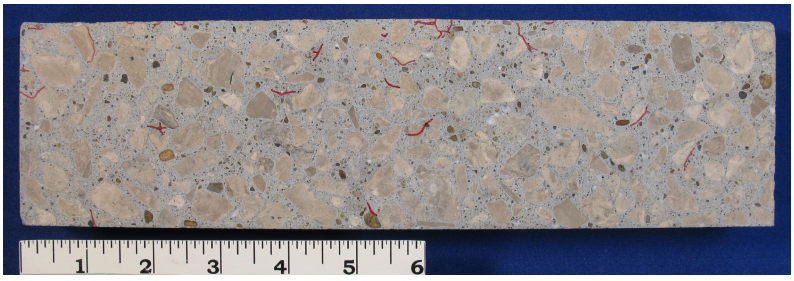

d) NRA-365

Figure 36 Lapped surfaces of NRA specimens with traced microcracks

TABLE XII QUALITATIVE SUMMARY OF PETROGRAPHIC OBSERVATIONS

Specimen	Amount of Microcracks	Amount of ASR gel partially lining to filling microcracks	Amount of ASR gel partially lining to filling air voids
RA-28	Some	Few	Few
RA-90	Several	Some	Some
RA-180	Many	Several	Some
RA-365	Many	Many	Many
NRA-28	None	None	None
NRA-90	Few	None	Few
NRA-180	Few	None	Few
NRA-365	Some	Some	Few
Qualitative Scale: None – Few – Some – Several – Many			

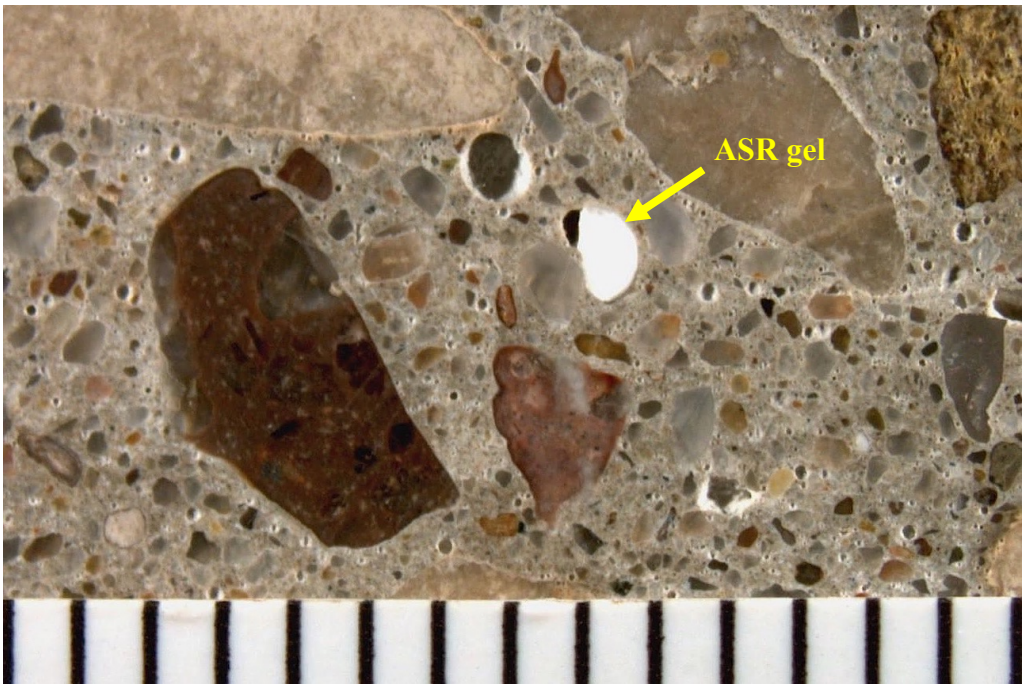

Figure 37 ASR gel partially filling a void in RA-365. Scale is in 1 mm increments.

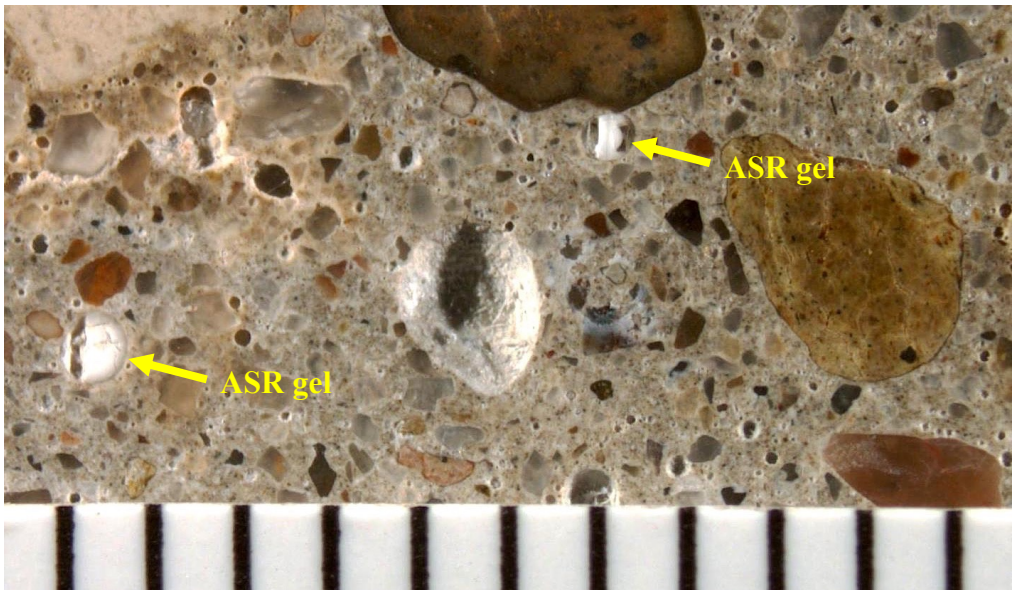

Figure 38 ASR gel partially filling two voids in RA-365. Scale is in 1 mm increments.

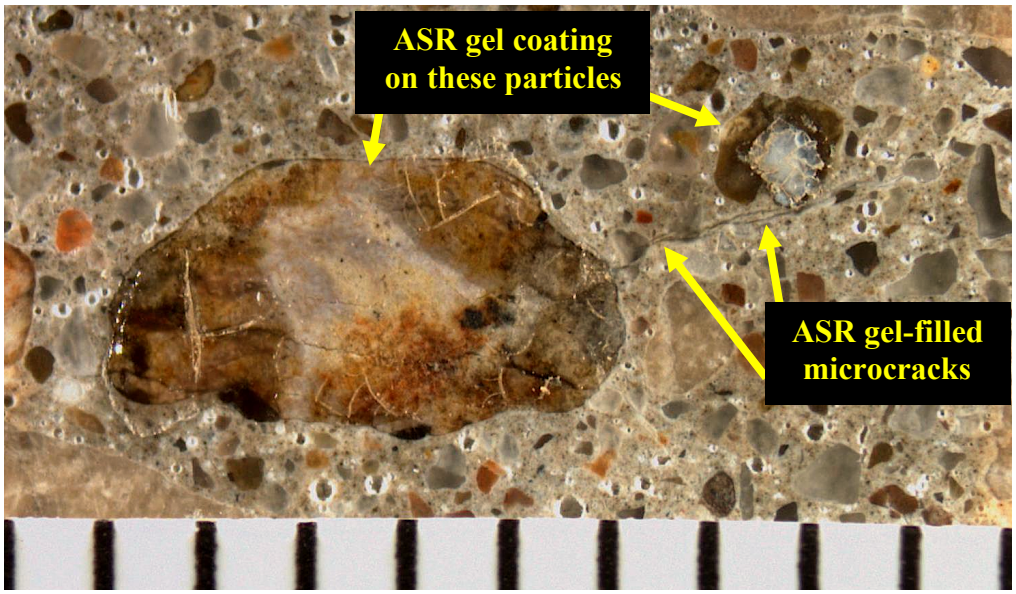

Figure 39 ASR gel features in RA-365. ASR gel coats two reactive sand particles and fills microcracks extending outwardly from the larger particle on left. Scale is in 1 mm increments.

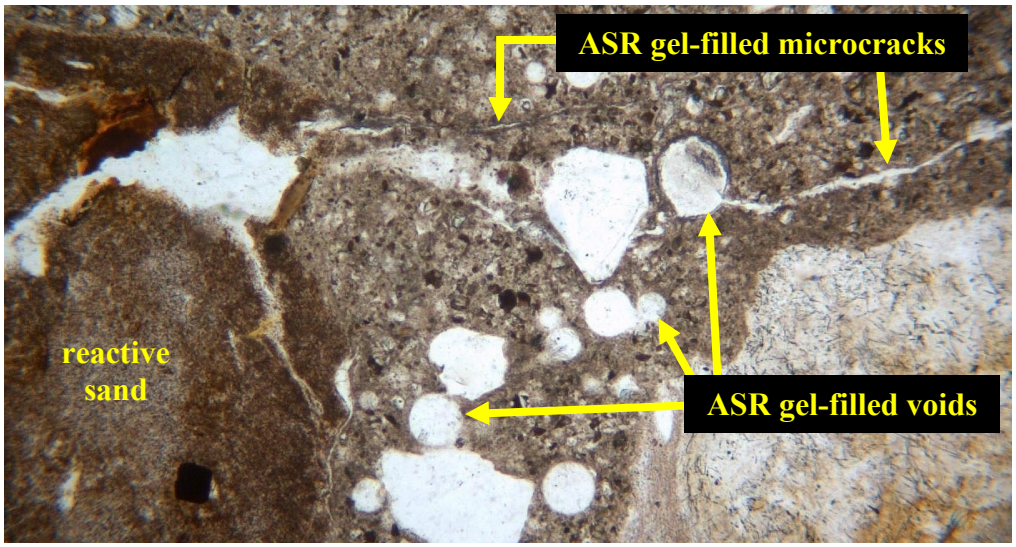

Figure 40 Thin-section photomicrograph of ASR gel and microcracking in RA-365 at 100x. ASR gel exudes from a reactive sand particle (left) and fills voids and microcracks extending outwardly from the particle. Field of view is approximately 1 mm. Plane-polarized light.

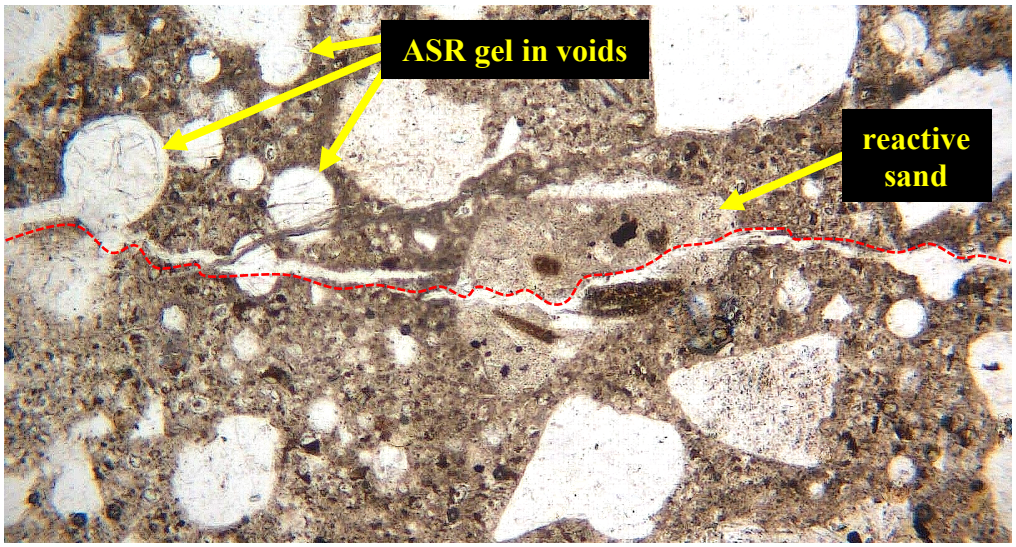

Figure 41 Thin-section micrograph of ASR deterioration in RA-365 at 100x. One long ASR gel-filled microcrack extends through a reactive sand particle (red line). Other gel-filled microcracks and voids are also present. Field of view is approximately 1 mm. Plane-polarized light.

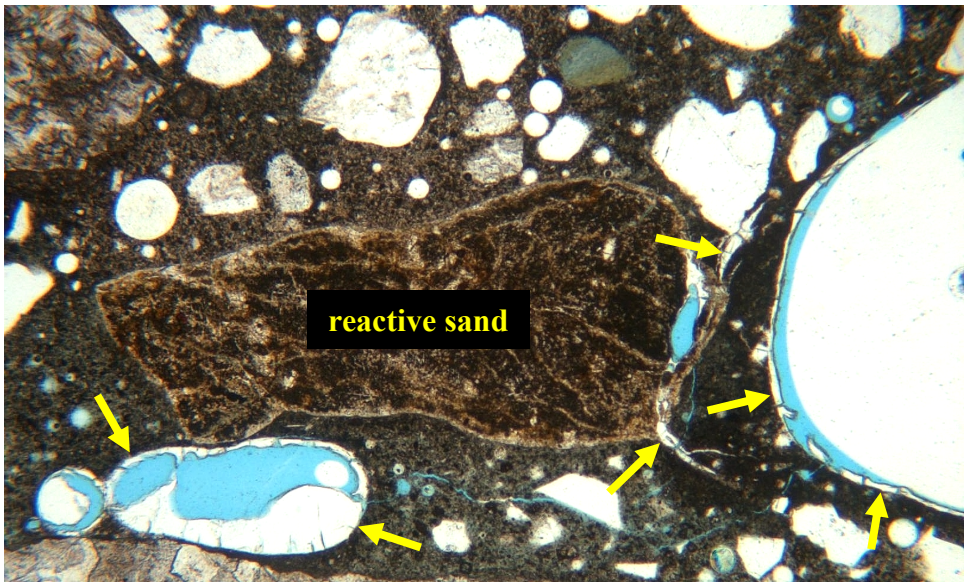

a) 50x magnification

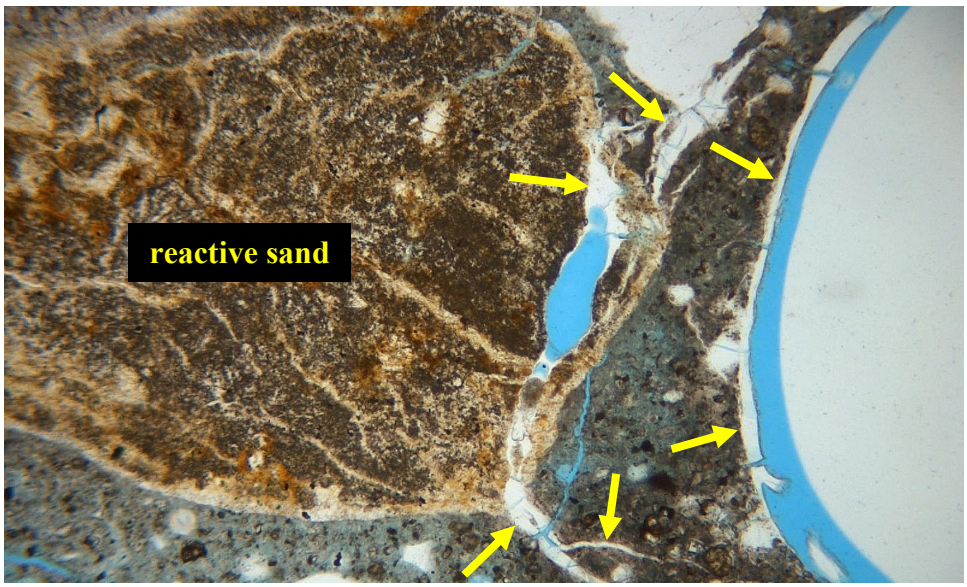

b) 100x magnification

Figure 42 Thin-section micrographs of RA-28 at 50x (a) and 100x (b) magnifications, showing ASR deterioration highlighted with blue epoxy. ASR gel (yellow arrows) extends outwardly from a reactive fine aggregate particle through microcracks and lines air voids. The paste is impregnated with blue epoxy to illustrate the presence of ASR gel, which appears clear in thin section in plane-polarized light. Field of view is approximately 1 mm. Plane-polarized light.

Thin-section analysis of blue epoxy-impregnated thin-section blocks cut from Specimens RA-28, RA-365, NRA-28 and NRA-365 was performed to observe paste absorption characteristics (Figure 42 to Figure 46). The paste in reactive specimens absorbed more blue epoxy than the paste in nonreactive specimens. Specimens RA-28 and RA-365 exhibit fairly substantial blue epoxy uptake (Figure 43and Figure 44). Specimens NRA-28 and NRA-365 exhibit slight blue epoxy uptake (Figure 45 and Figure 46). The ability or inability of the paste to absorb the blue epoxy is attributed to the degree of free pore space within the paste matrix. As shown in Table XI, the water volume fraction in nonreactive specimens is much greater than the water volume fraction in reactive specimens. The amount of blue epoxy uptake directly corresponds to the calculated water volume fraction in reactive and nonreactive specimens. The fairly substantial amount of blue epoxy uptake in reactive specimens is attributed to the low water volume fraction; less pore space is filled with water enabling greater blue epoxy impregnation. The minor amount of blue epoxy uptake in nonreactive specimens is attributed to the higher water volume fraction; more pore space is filled with water enabling less blue epoxy impregnation.

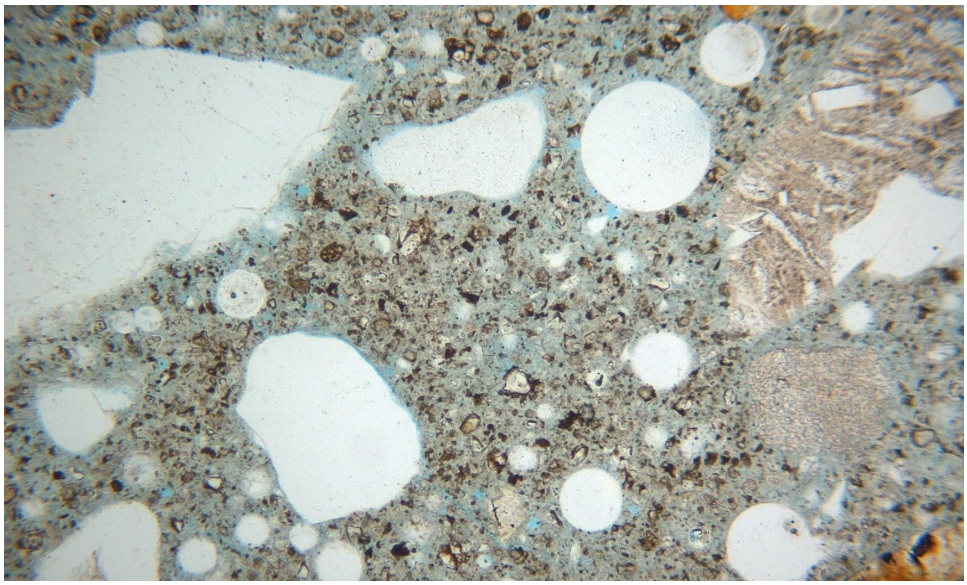

Figure 43 Thin-section micrograph of RA-28 impregnated with blue epoxy at 100x. Blue epoxy uptake in paste is fairly substantial. Field of view is approximately 1 mm. Plane-polarized light.

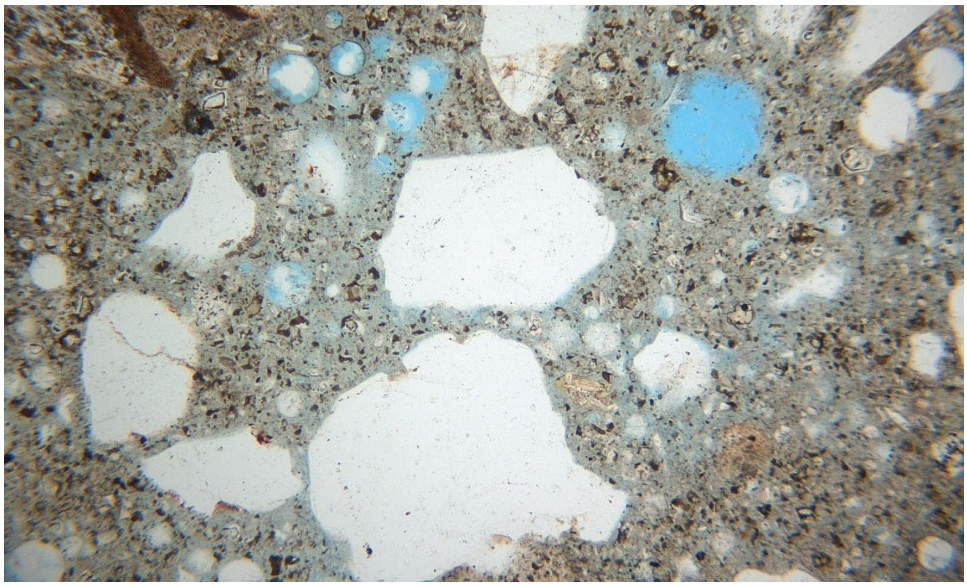

Figure 44 Thin-section micrograph of RA-365 impregnated with blue epoxy at 100x. Blue epoxy uptake in paste is fairly substantial. Field of view is approximately 1 mm. Plane-polarized light.

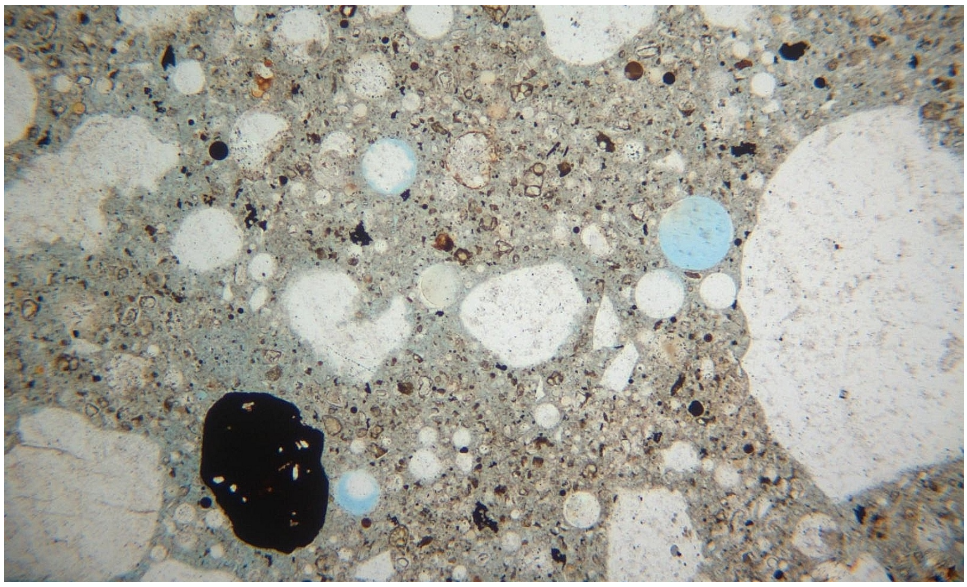

Figure 45 Thin-section micrograph of NRA-28 impregnated with blue epoxy at 100x. Blue epoxy uptake in paste is minor. Field of view is approximately 1 mm. Plane-polarized light.

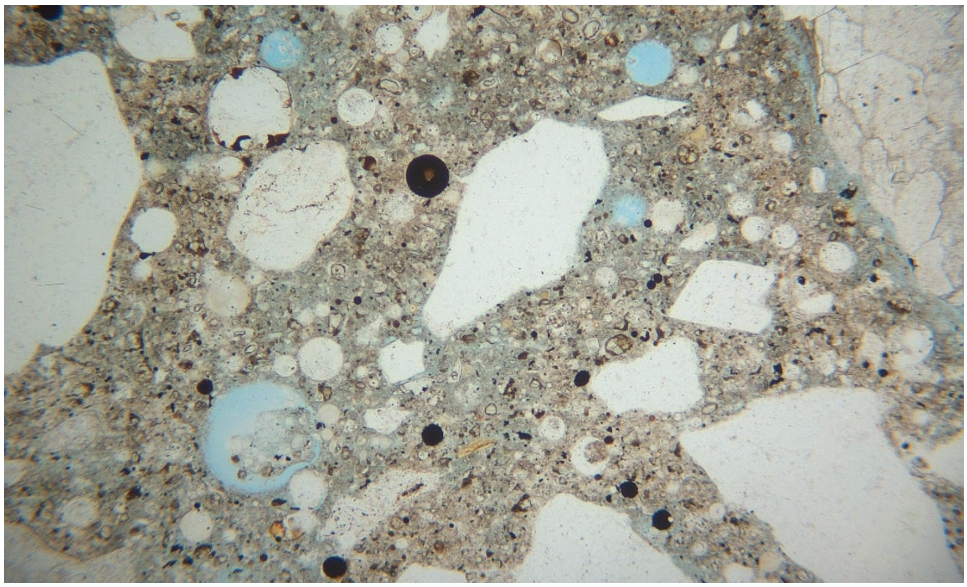

Figure 46 Thin-section micrograph of NRA-365 impregnated with blue epoxy at 100x. Blue epoxy uptake in paste is minor. Field of view is approximately 1 mm. Plane-polarized light.

Normalized DRI scores at 365 days were 595 for Specimen RA-365 and only 52 for Specimen NRA-365. Nonreactive specimens only showed approximately 8% of the ASR-related deterioration that the reactive specimens displayed (Figure 47, TABLE XIII, TABLE XIV). The amount of cracking observed in both reactive and nonreactive specimens appears to follow the same trend as length expansion results (Figure 13 and Figure 48). Surprisingly, the amount of cracks (fractures or frx in DRI shorthand) in paste is essentially the same in RA-180 and RA-365; the only difference is that the majority of the cracks are filled with ASR gel in RA-365 compared to only a small amount in RA-180 (Figure 48 and Table XV). The amount of observed gel increases with time in both reactive and nonreactive specimens; however, the amount of gel significantly increases between 180 and 365 days in reactive specimens and even notably in nonreactive specimens (Figure 49 and Table XVI).

Such crack and gel observations reveal valuable information for this study. ASR gel formation progresses rapidly between 180 and 365 days whereas cracking slows down during this time period. It is hypothesized that initial ASR gel formation causes the majority of initial cracking correlated to length expansion results in the first 90 days and then, because cracks relieve pressure locally to some degree, ASR gel has void space (cracks) to migrate through without causing cracking to occur at the rate at which it did initially.

ASR gel formation between 180 and 365 days was only presumably the cause of changing impedance values and the notable decrease in bulk resistance and dielectric constant;

however, these measurements can now be correlated to confirmed observations. The substantial increase in amount of ASR gel corresponds to the substantial decrease in water volume fraction measured from dielectric constant calculations during microwave testing. This correlation appears to indicate that as ASR gel formation progresses rapidly, ASR gel readily absorbs moisture from the system thereby decreasing the amount of available moisture in the specimens.

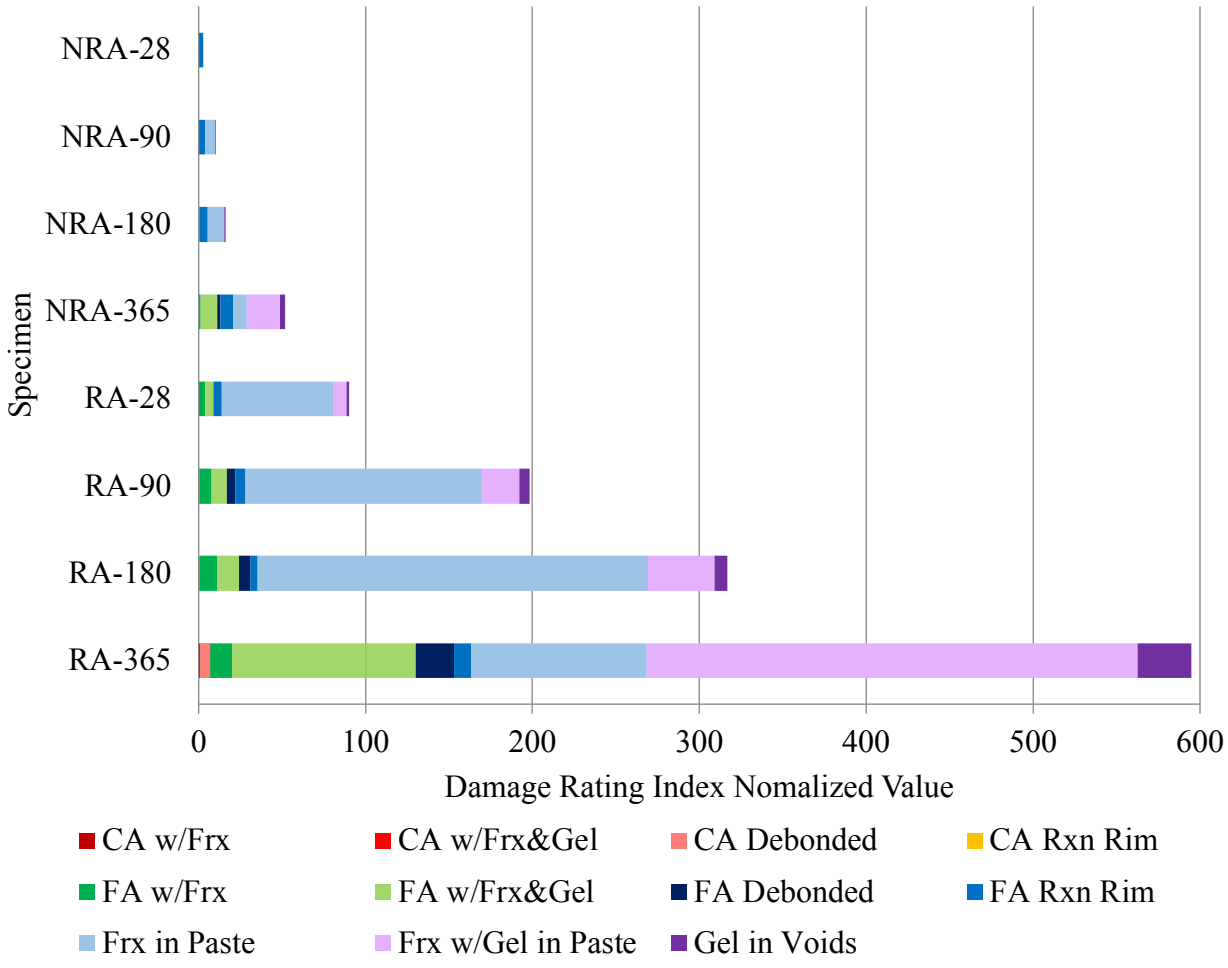

Figure 47 Summary of normalized DRI values

TABLE XIII DRI VALUES FOR RA SPECIMENS

Feature	RA-28	RA-90	RA-180	RA-365
CA w/Frx	0	2	2	6
(multiplier value)	0	0	0	1
CA w/Frx&Gel	0	0	0	0
(multiplier value)	0	0	0	0
CA Debonded	0	0	0	4
(multiplier value)	0	0	0	6
CA Rxn Rim	0	0	0	0
(multiplier value)	0	0	0	0
FA w/Frx	30	61	87	106
(multiplier value)	4	8	11	13
FA w/Frx&Gel	5	9	13	110
(multiplier value)	5	9	13	110
FA Debonded	0	5	7	23
(multiplier value)	0	5	7	23
FA Rxn Rim	40	49	33	84
(multiplier value)	5	6.125	4.125	11
Frx in Paste	67	142	234	105
(multiplier value)	67	142	234	105
Frx w/Gel in Paste	4	11	20	147
(multiplier value)	8	22	40	294
Gel in Voids	6	25	30	129
(multiplier value)	2	6	8	32
Score	180.5	396.5	633.5	1189.5
Area (cm^2)	200	200	200	200
Normalized Score	90	198	317	595

TABLE XIV DRI VALUES FOR NRA SPECIMENS

Feature	NRA-28	NRA-90	NRA-180	NRA-365
CA w/Frx	0	0	0	0
(multiplier value)	0	0	0	0
CA w/Frx&Gel	0	0	0	0
(multiplier value)	0	0	0	0
CA Debonded	0	0	0	0
(multiplier value)	0	0	0	0
CA Rxn Rim	0	0	0	0
(multiplier value)	0	0	0	0
FA w/Frx	0	1	2	9
(multiplier value)	0	0	0	1
FA w/Frx&Gel	0	0	0	10
(multiplier value)	0	0	0	10
FA Debonded	0	0	0	2
(multiplier value)	0	0	0	2
FA Rxn Rim	23	31	40	62
(multiplier value)	2.875	4	5	7.75
Frx in Paste	0	6	10	8
(multiplier value)	0	6	10	8
Frx w/Gel in Paste	0	0	0	10
(multiplier value)	0	0	0	20
Gel in Voids	0	1	4	11
(multiplier value)	0	0	1	3
Score	5.75	20.5	32.5	103.25
Area (cm^2)	200	200	200	200
Normalized Score	3	10	16	52

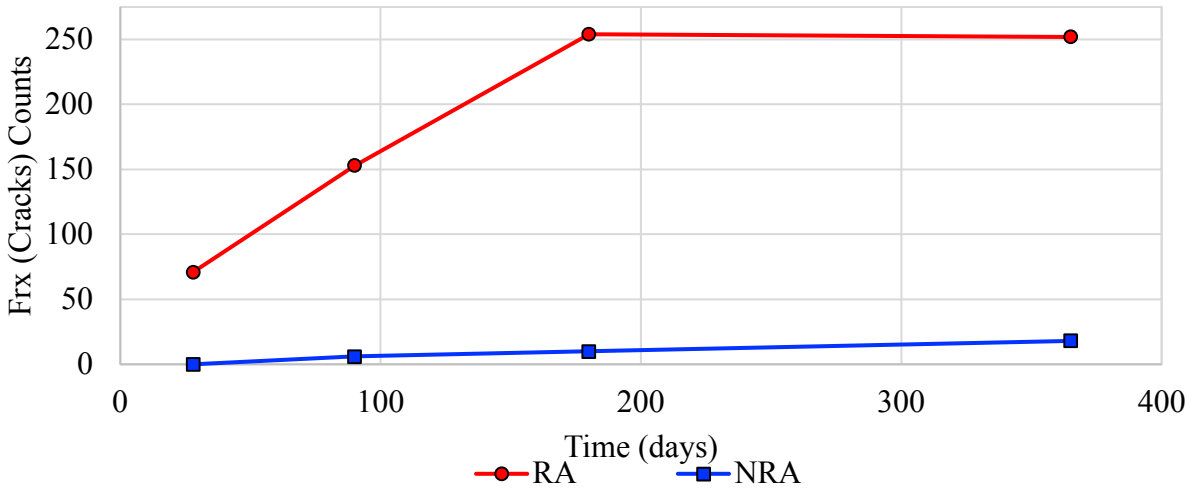

Figure 48 DRI frx (crack) counts over time

Table XV DRI FRX (CRACK) COUNTS OVER TIME

Specimen	Frx in Paste	Frx w/Gel in Paste	Total Frx Counts
RA-28	67	4	71
RA-90	142	11	153
RA-180	234	20	254
RA-365	105	147	252
NRA-28	0	0	0
NRA-90	6	0	6
NRA-180	10	0	10
NRA-365	8	10	18

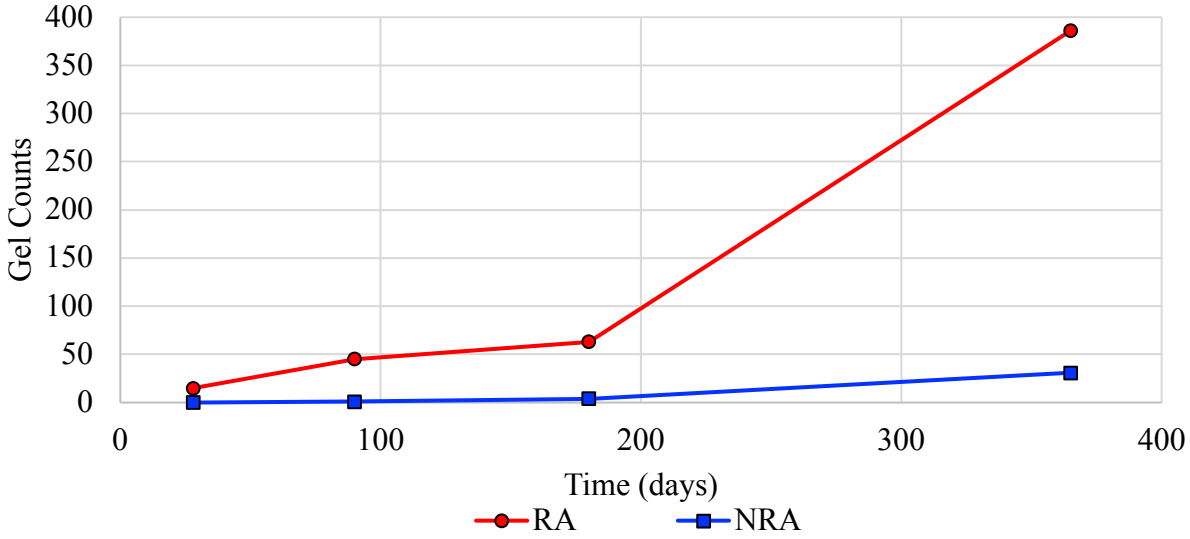

Figure 49 DRI gel counts over time

Table XVI DRI GEL COUNTS OVER TIME

Specimen	CA w/Frx & Gel	FA w/Frx & Gel	Frx w/Gel in Paste	Gel in Voids	Total Gel Counts
RA-28	0	5	4	6	15
RA-90	0	9	11	25	45
RA-180	0	13	20	30	63
RA-365	0	110	147	129	386
NRA-28	0	0	0	0	0
NRA-90	0	0	0	1	1
NRA-180	0	0	0	4	4
NRA-365	0	10	10	11	31

E. Acoustic Microscope Image Analysis

Sonoscan GEN6™ C-SAM® testing yielded acoustic microscope (AM) images of the exterior surface and interior lapped surface of the concrete specimens. Images collected from the exterior surface of both Specimens RA-365 and NRA-365 were substantially affected by the amount of residual sodium hydroxide solution on the surface and, as a result, variable imaging was produced and no valuable data or observations could be collected from the surfaces (Figure 50 and Figure 51). Images collected from the interior lapped surface of all eight specimens are presented in Figure 52 through Figure 59. The interior lapped surface of Specimen RA-365 also shows variable imaging observable through the variation of color between that of the longitudinal midportion of the surface compared to that of the longitudinal side surfaces (Figure 55). The cause of variable imaging is unknown but could be due to equipment error, differences in focal points and gain setting as measurements were taken at different times, uneven nature of the lapped surface, or chemical differences in the paste.

The intent of Sonoscan testing for this study was to assess the ability of acoustic imaging to aid in ASR evaluations through identification of cracking and ASR gel formation. It was hypothesized that acoustic imaging would readily highlight cracks and ASR gel; however, the images produced were less striking than images of the lapped surface with traced microcracks produced during petrographic examination with the current data; additional image processing can be done for future testing. Figure 60 and Figure 61 present AM images of reactive and nonreactive specimens, respectively, in a sequence which allows for visual comparison of

features over time and ASR progression. Figure 62 and Figure 63 present AM images of the lapped surface of each specimen alongside petrographic examination images of the equivalent section in which microcracks are traced in red ink. The two image types are descriptive in their own respect; AM images better distinguish between paste, aggregate and voids whereas the petrographic images with traced microcracks highlight mainly microcracks while also displaying a true visual representation of the concrete surface. Acoustic microscope images do highlight cracks in specimens, too, however, they are much less apparent. Acoustic microscope image analysis did not provide valuable information for rapid crack identification for this study and, therefore, the results are only in the form of images for additional comparison of specimens.

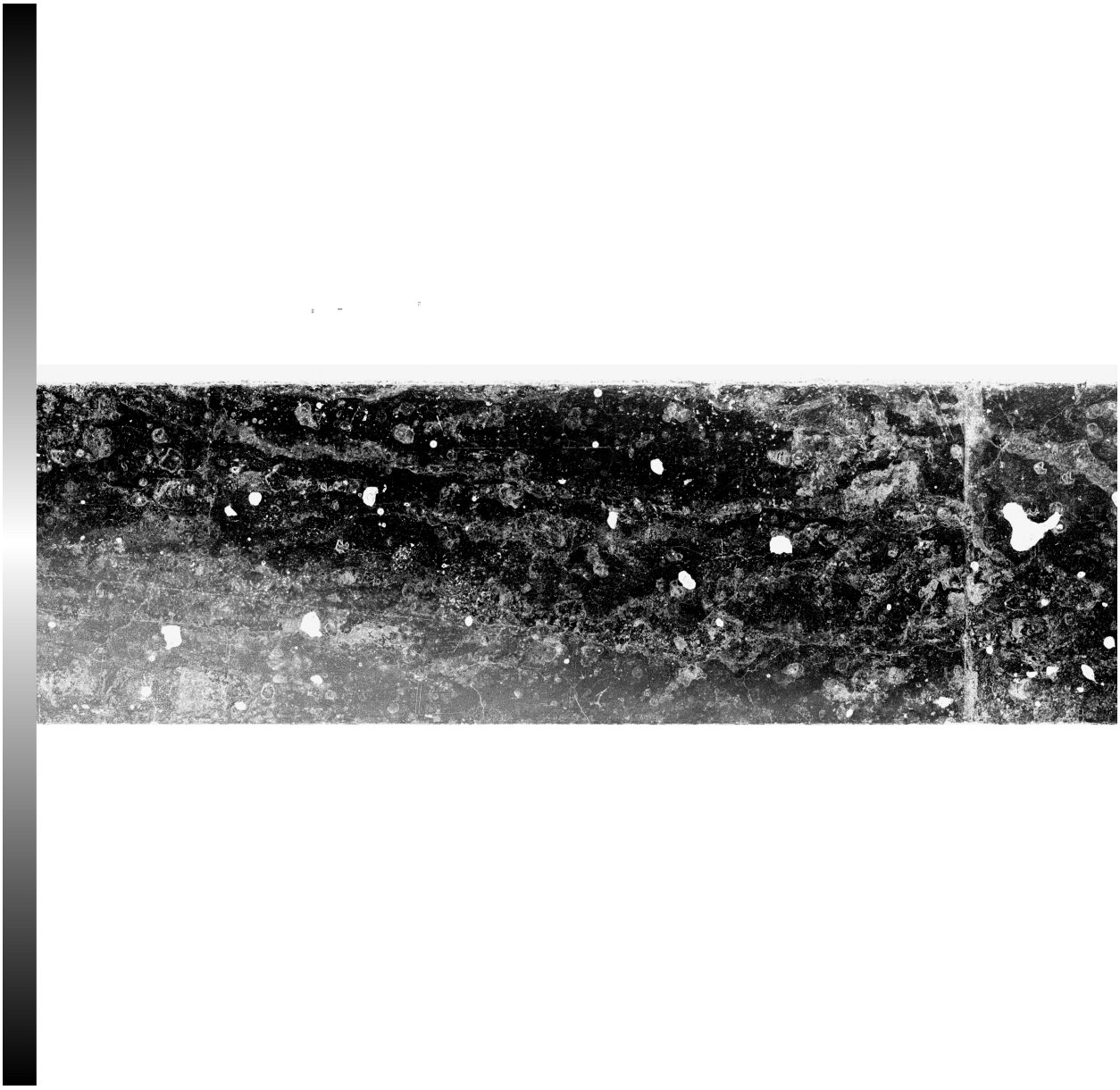

Figure 50 AM image of exterior surface of RA-365

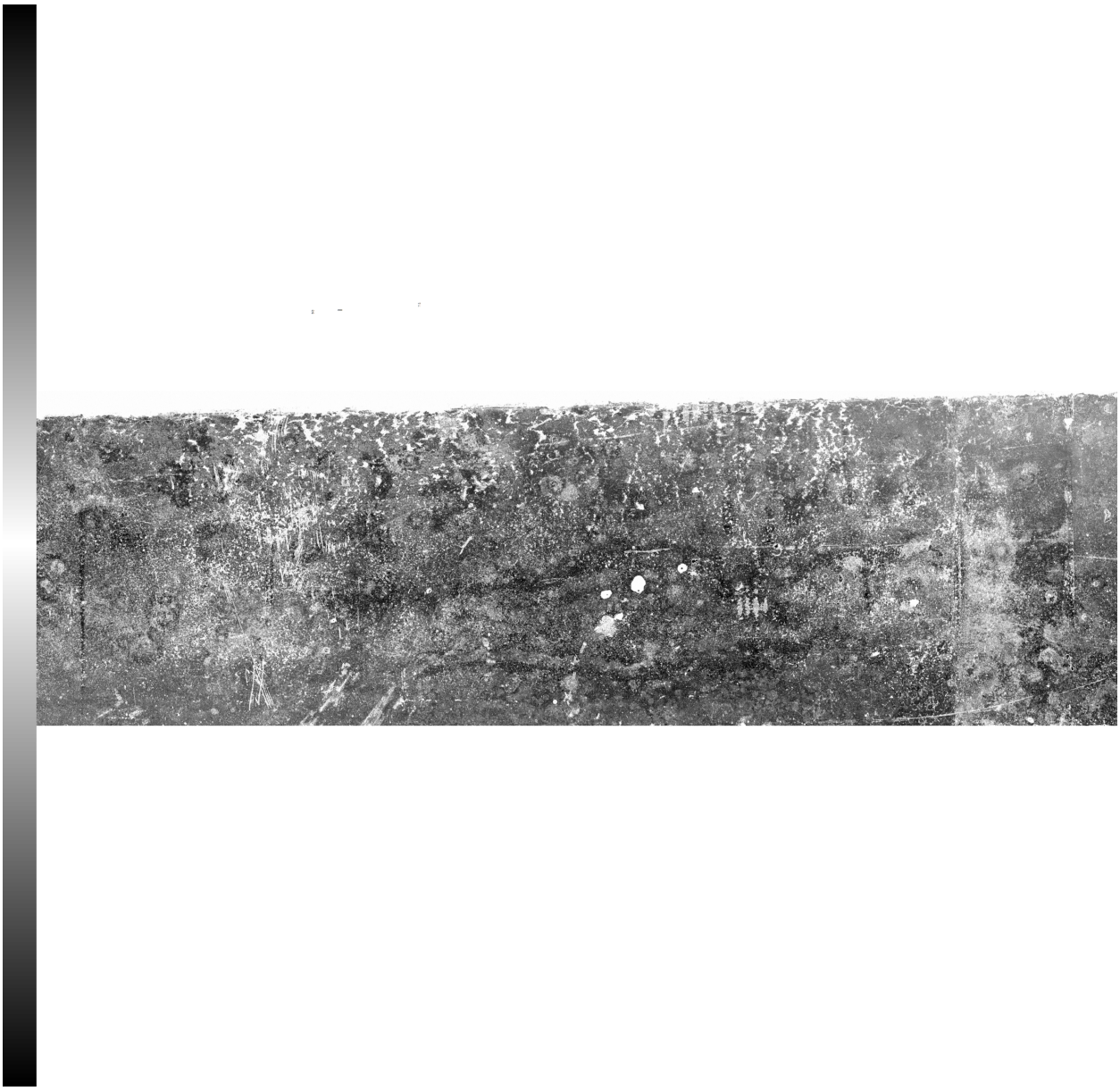

Figure 51 AM image of exterior surface of NRA-365

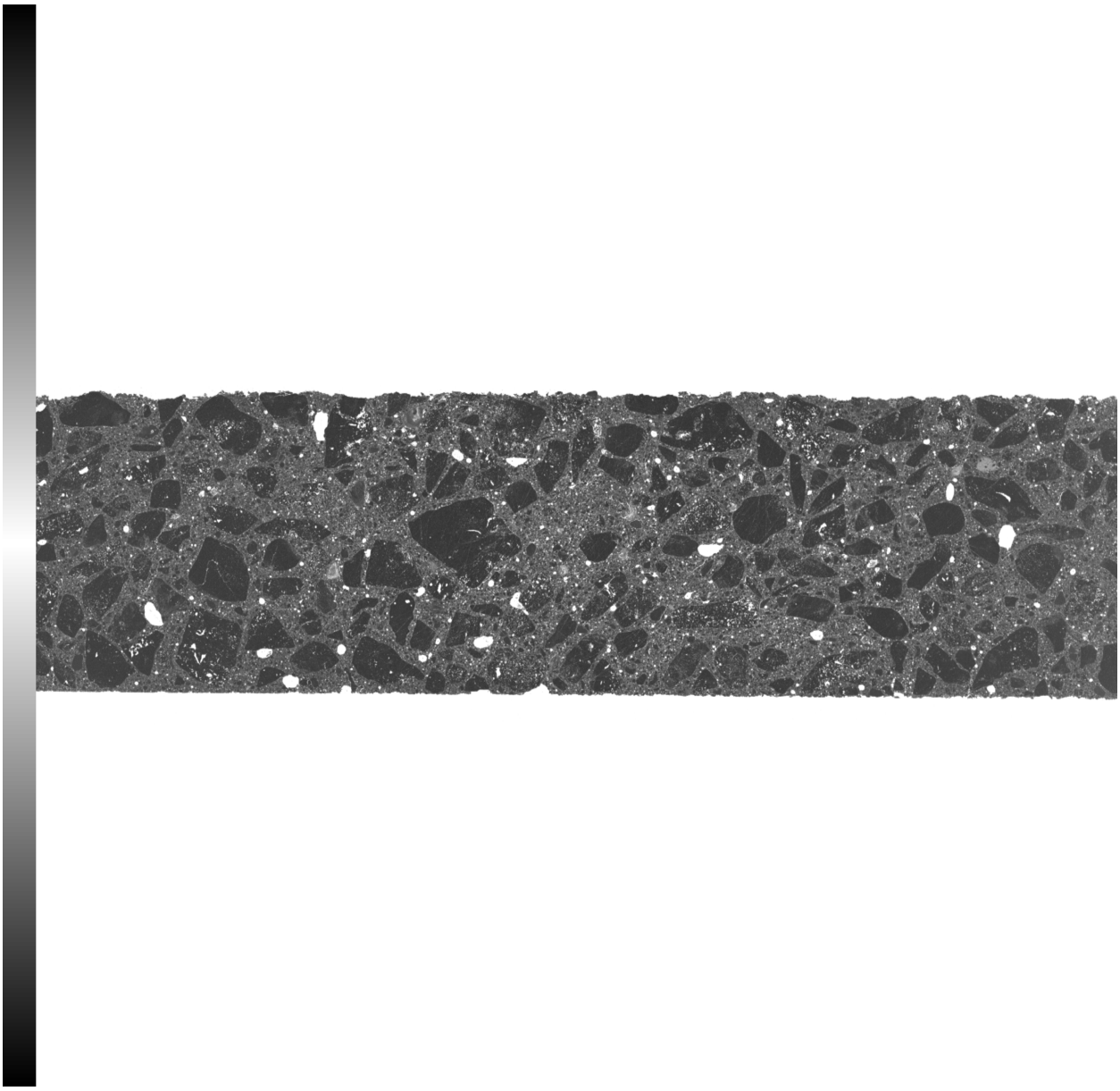

Figure 52 AM image of interior lapped surface of RA-28

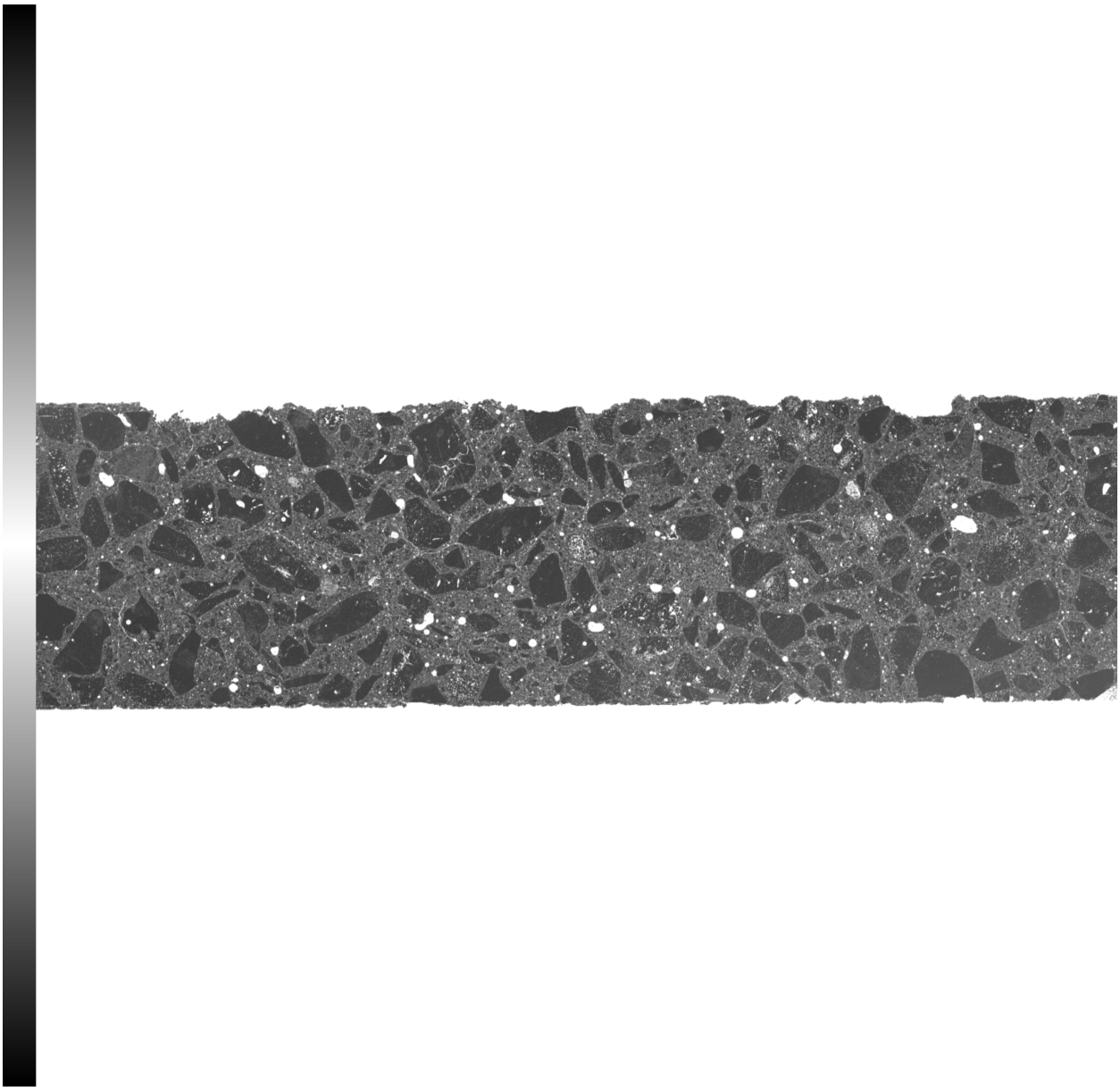

Figure 53 AM image of interior lapped surface of Specimen RA-90

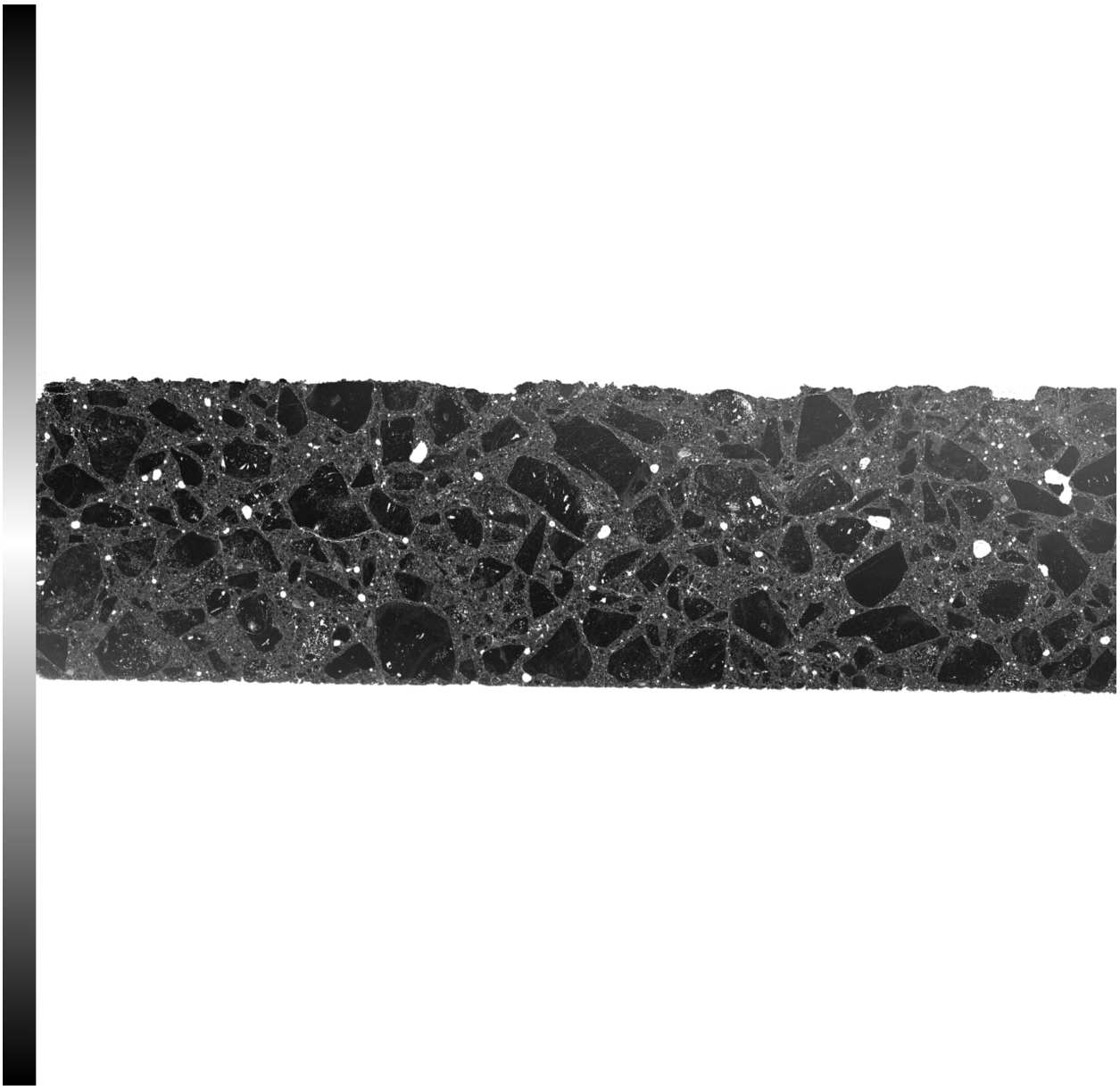

Figure 54 AM image of interior lapped surface of RA-180

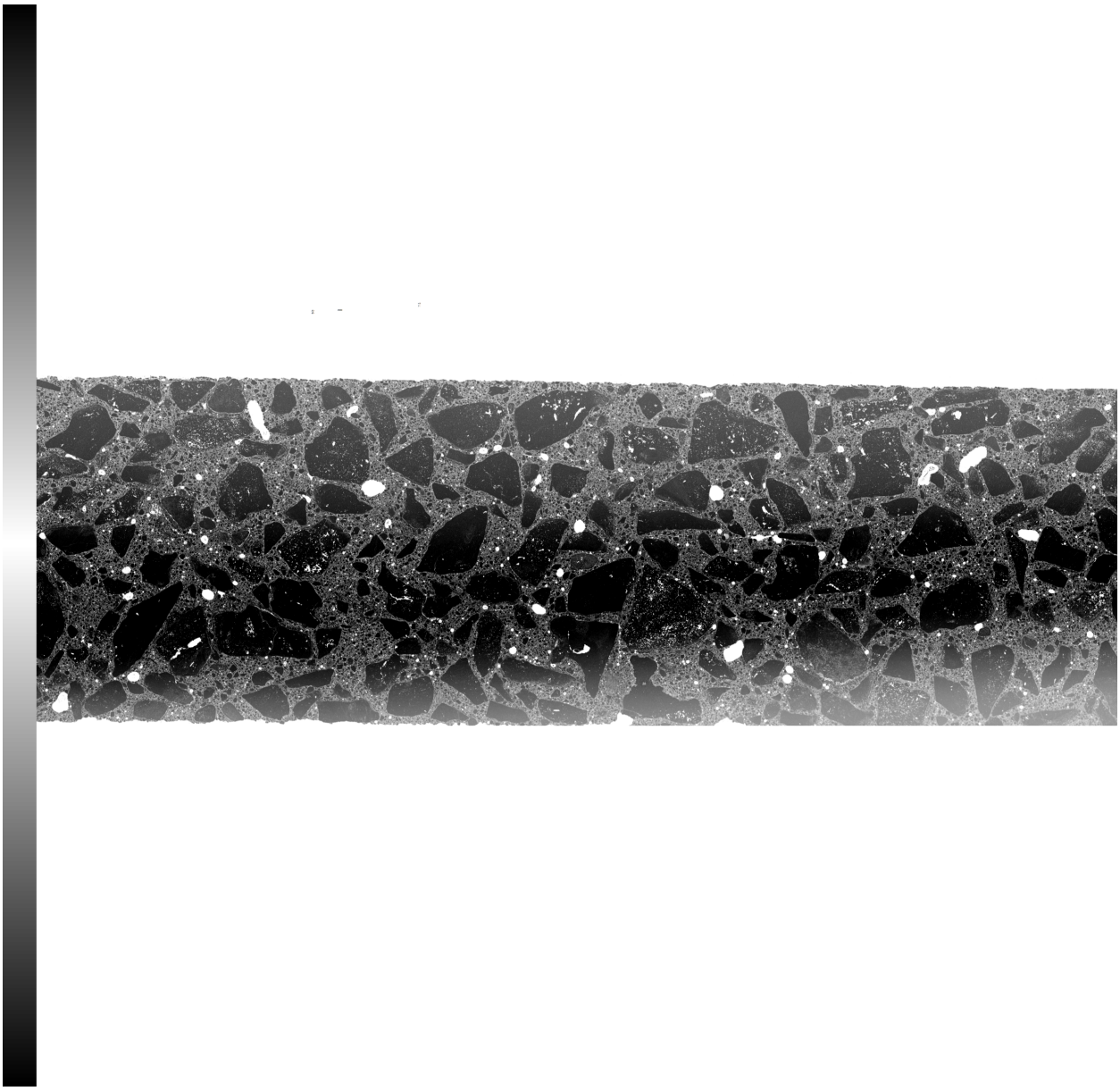

Figure 55 AM image of interior lapped surface of RA-365

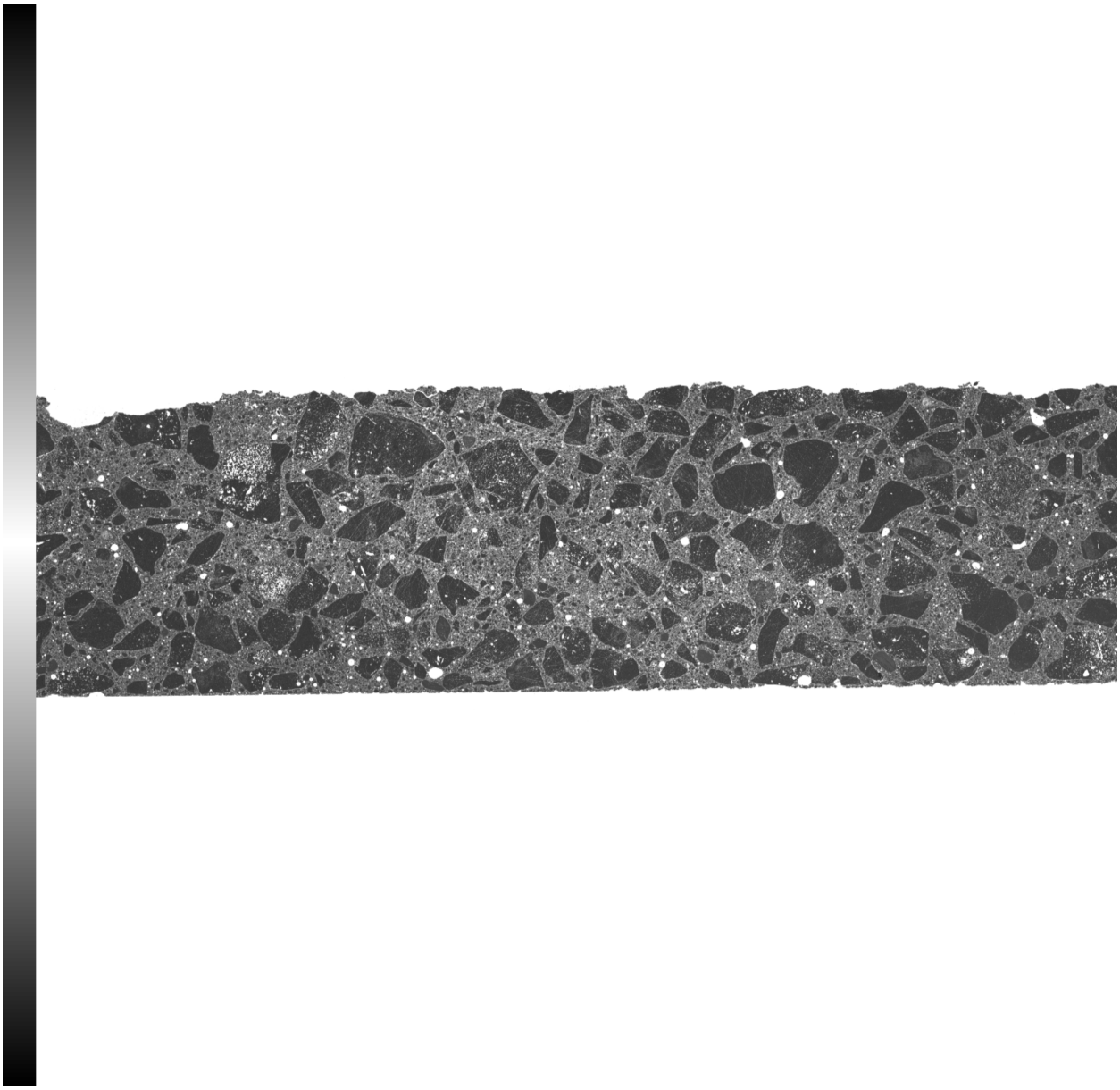

Figure 56 AM image of interior lapped surface of NRA-28

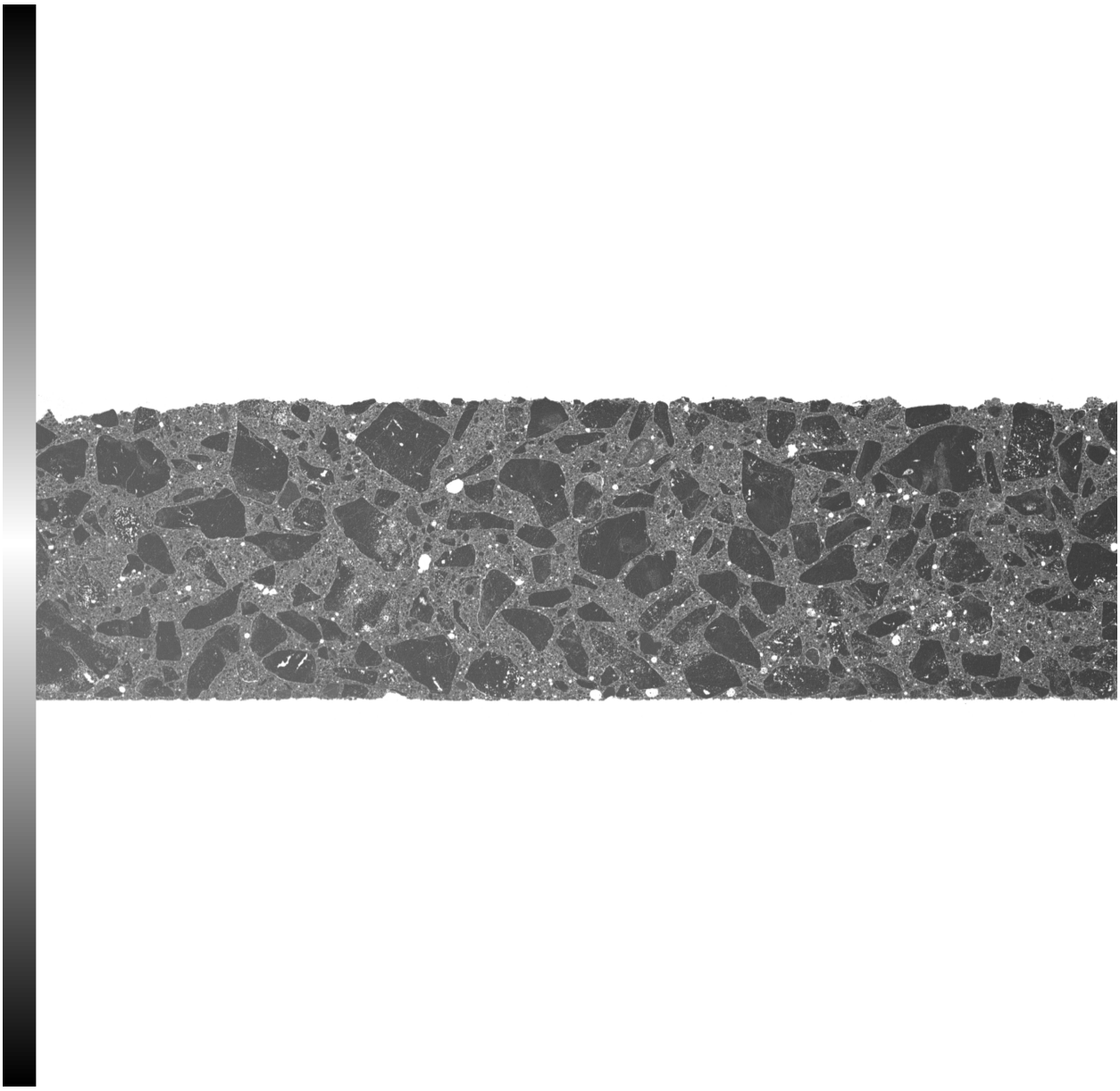

Figure 57 AM image of interior lapped surface of NRA-90

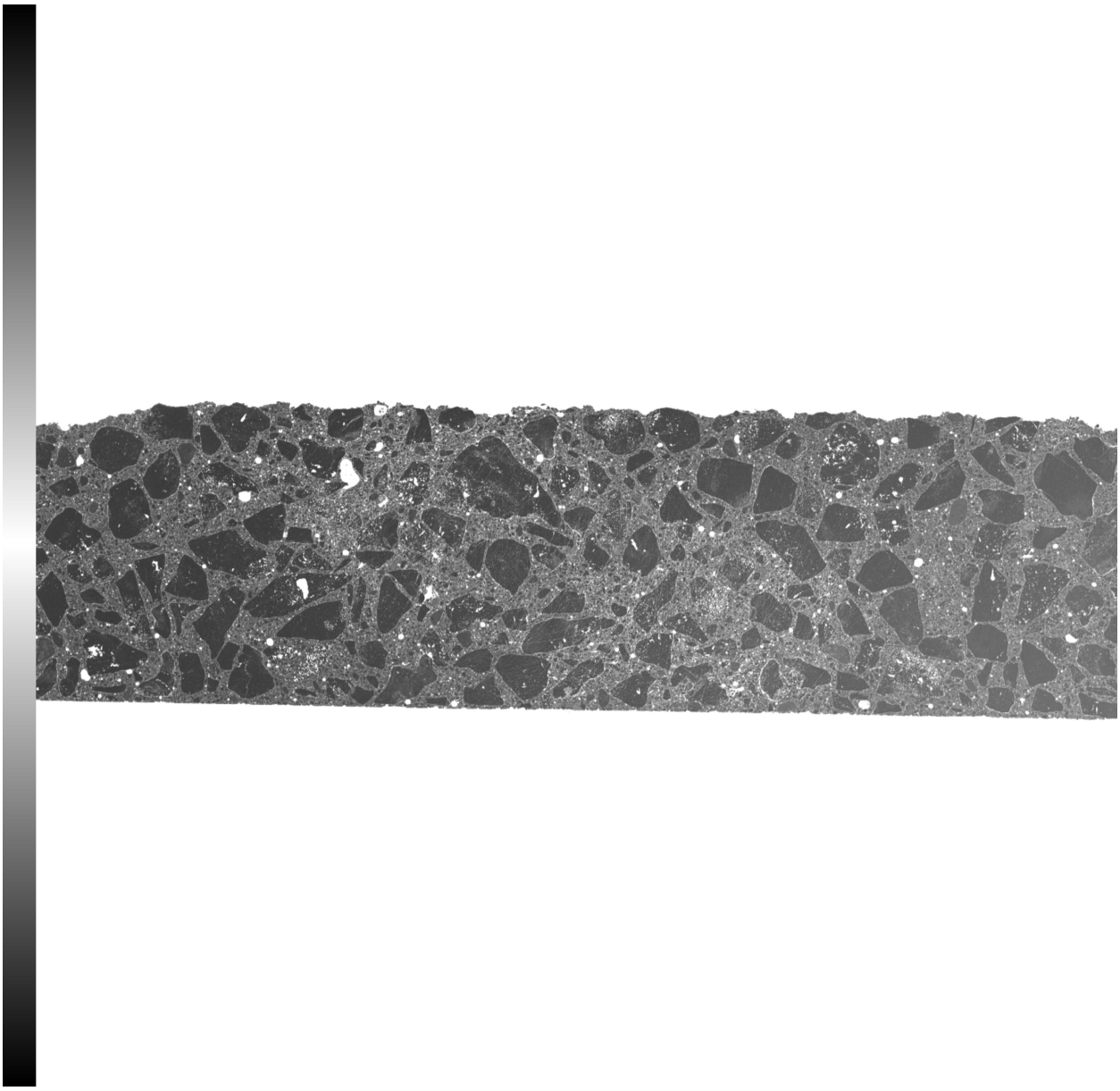

Figure 58 AM image of interior lapped surface of NRA-180

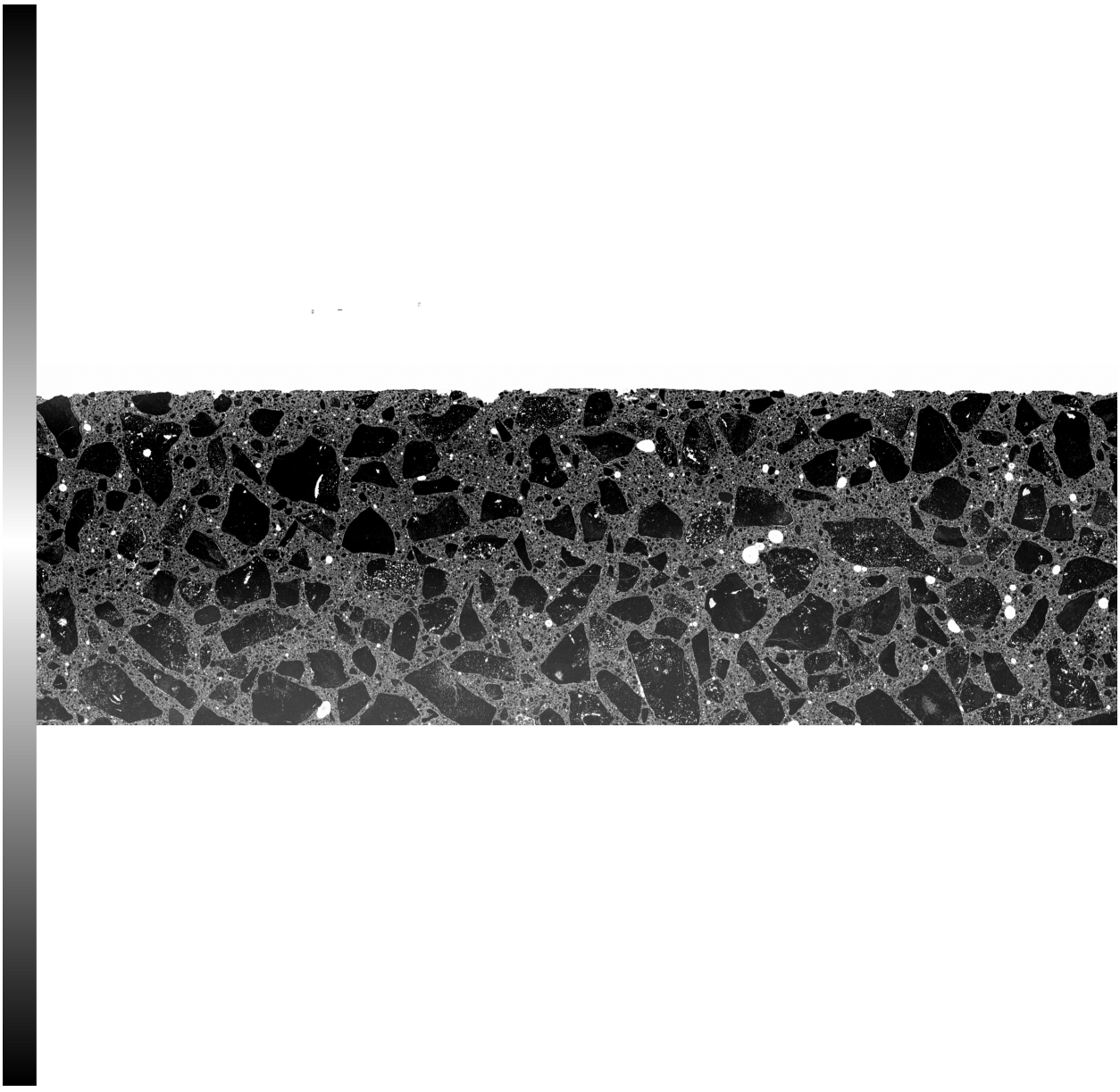

Figure 59 AM image of interior lapped surface of NRA-365

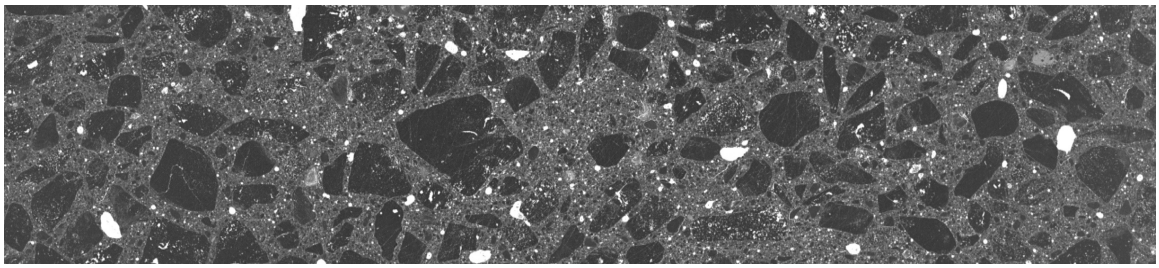

a) RA-28

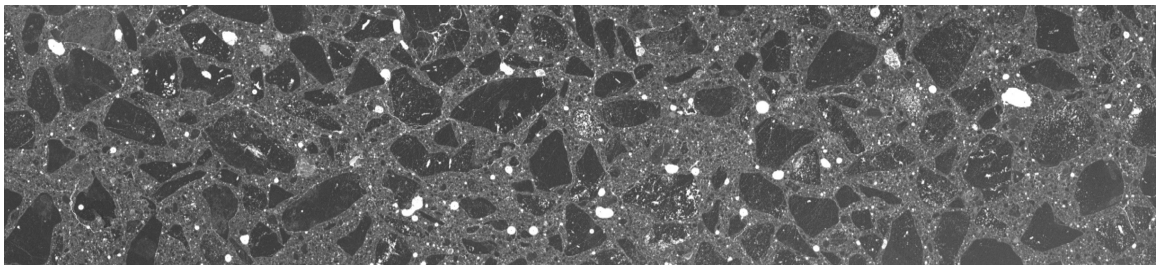

b) RA-90

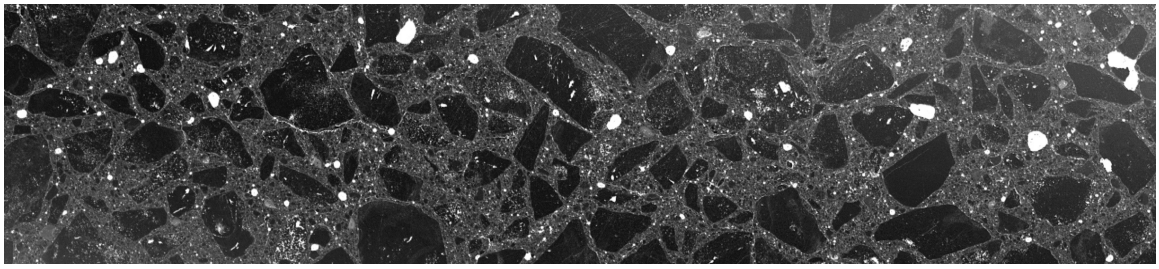

c) RA-180

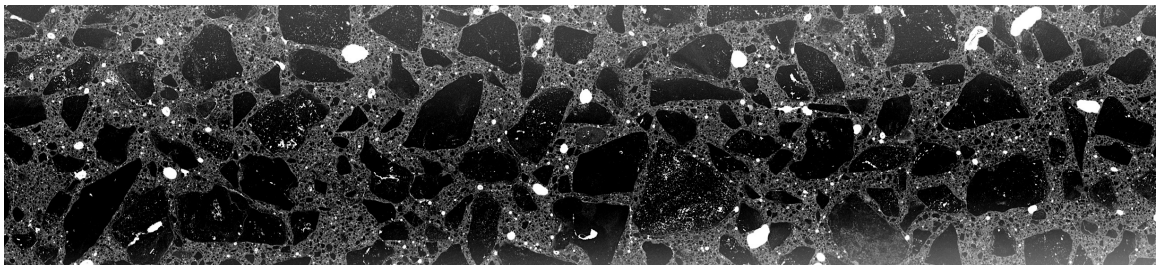

d) RA-365

Figure 60 AM images of RA specimens for comparison

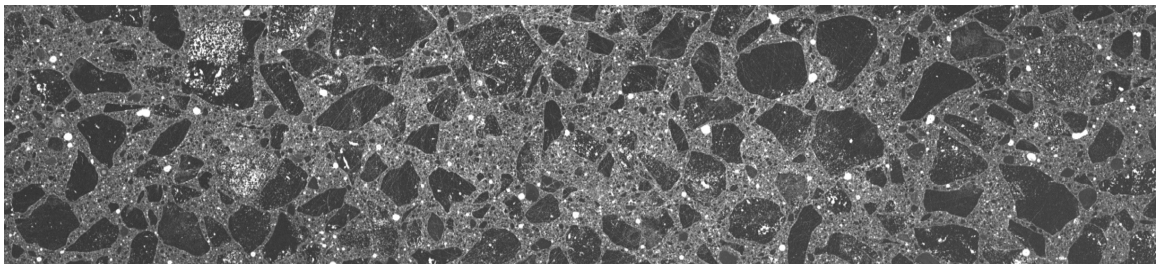

a) NRA-28

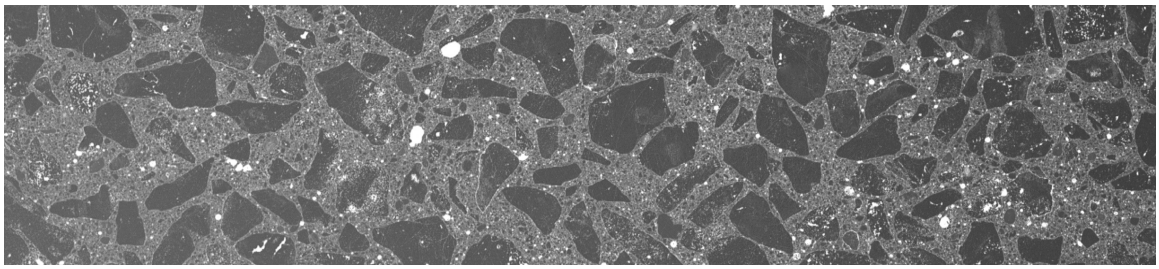

b) NRA-90

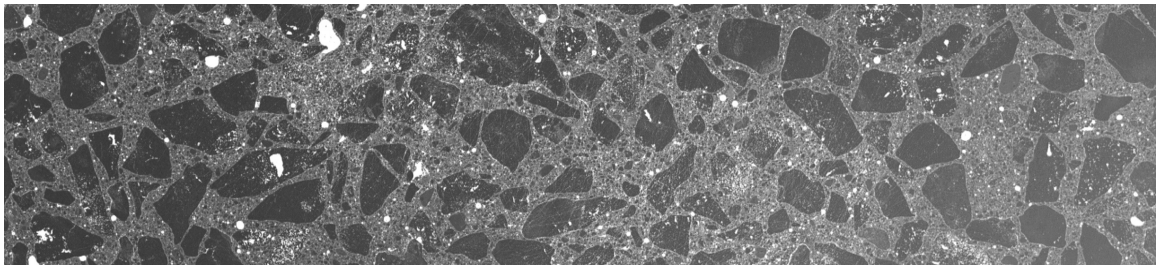

c) NRA-180

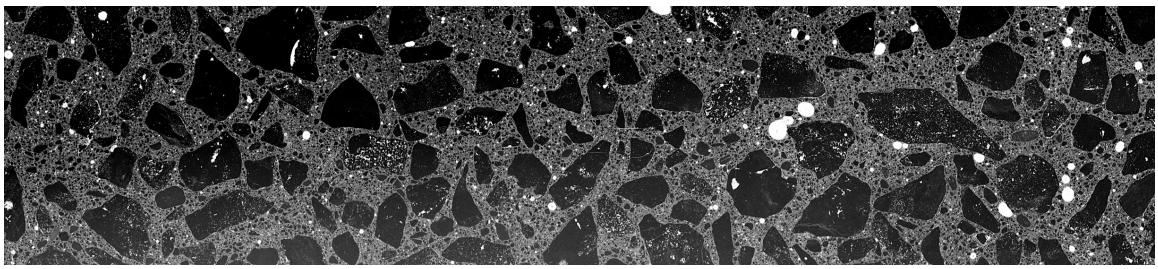

d) NRA-365

Figure 61 AM images of NRA specimens for comparison

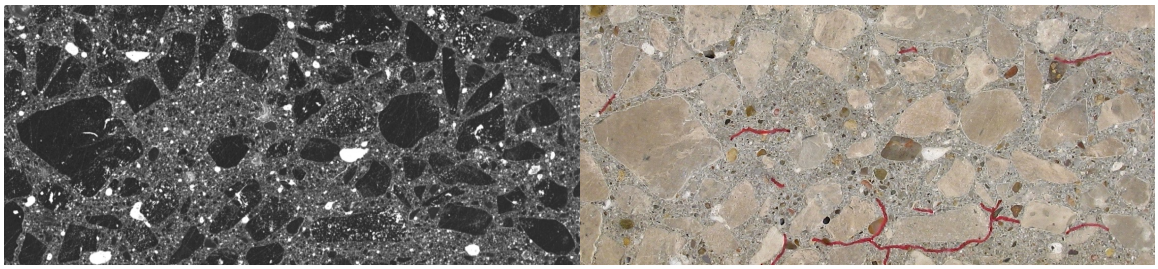

a) RA-28

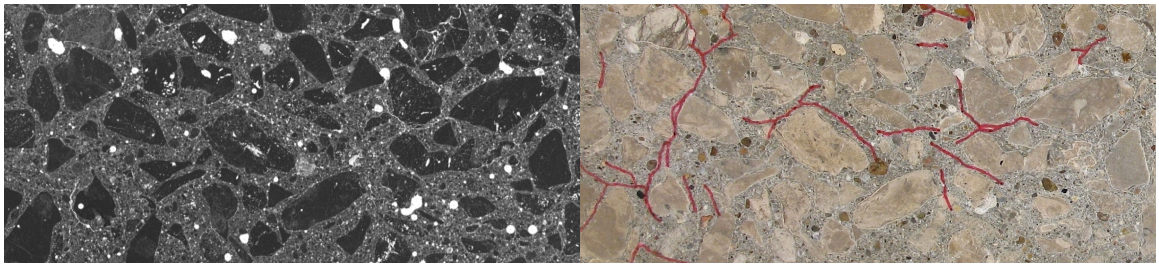

b) RA-90

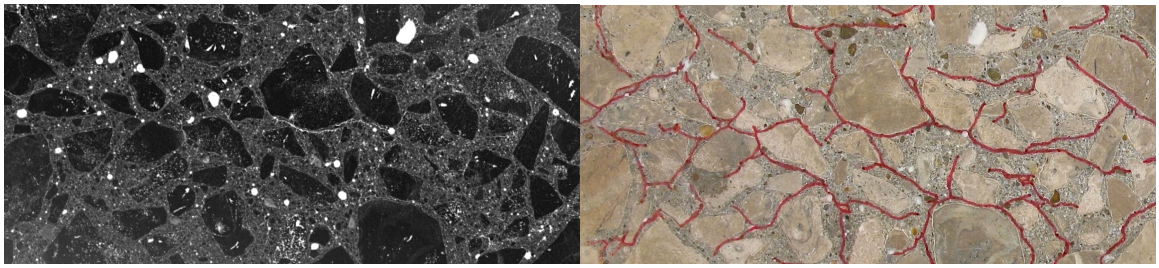

c) RA-180

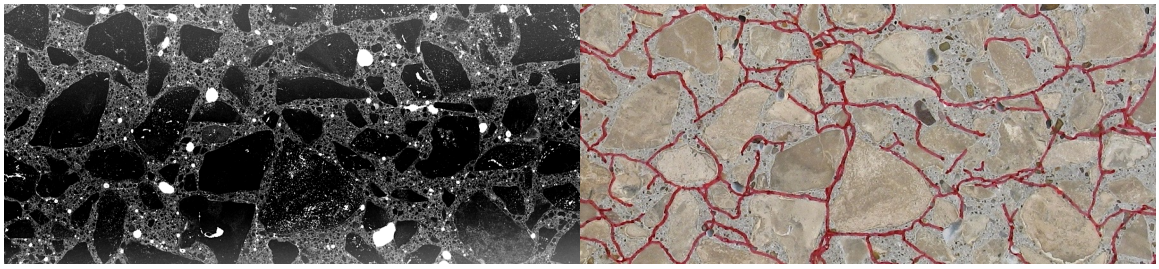

d) RA-365

Figure 62 AM and petrographic microcrack images of equivalent sections in RA specimens

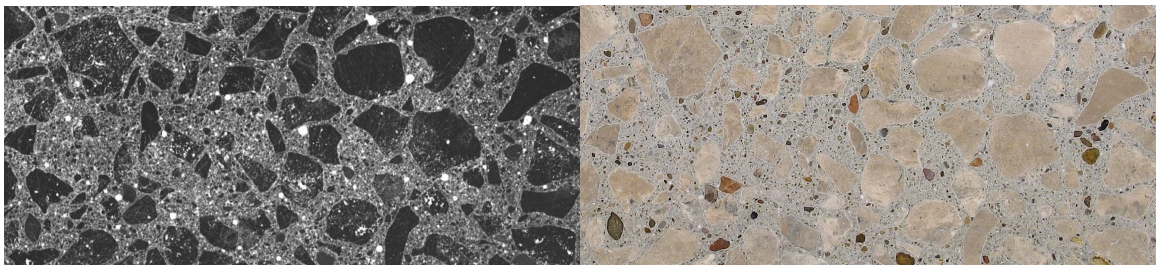

a) NRA-28

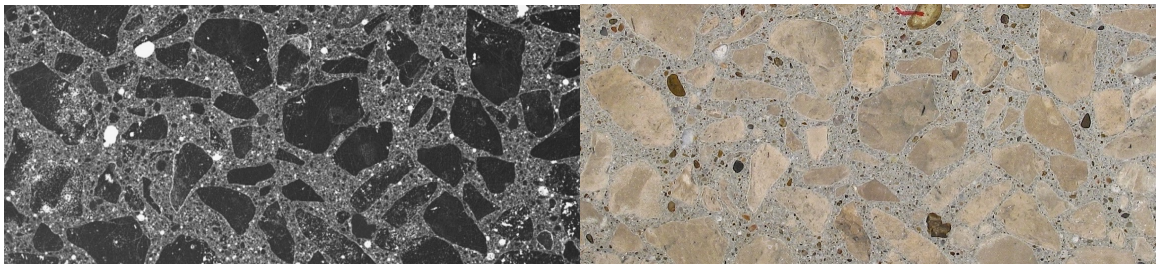

b) NRA-90

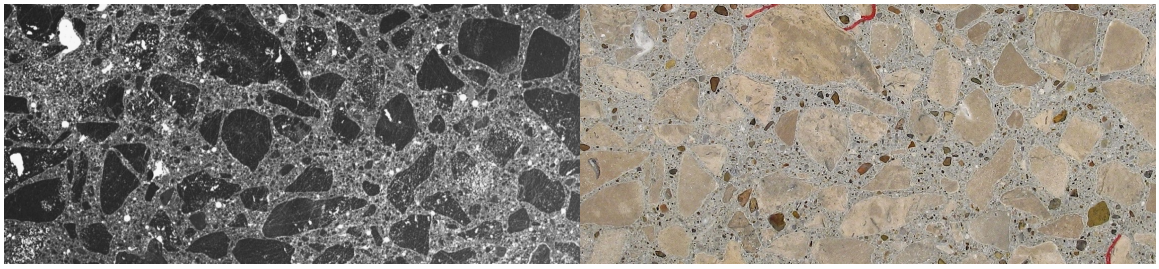

c) NRA-180

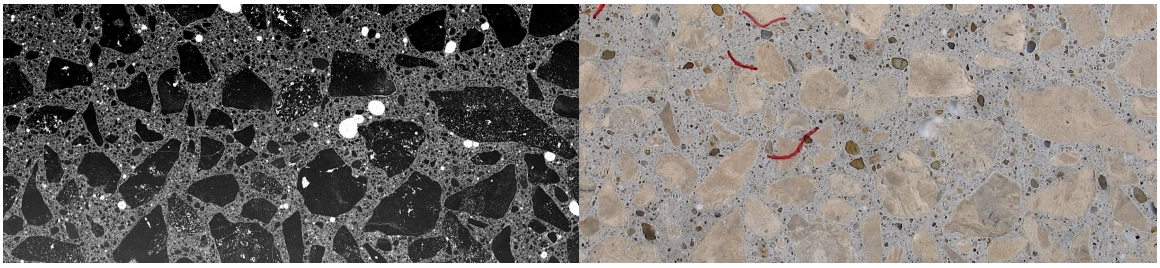

d) NRA-365

Figure 63 AM and petrographic microcrack images of equivalent sections in NRA specimens

V. CONCLUSION

A. Summary

EIS and microwave nondestructive testing techniques were successful in distinguishing between reactive and nonreactive specimens. Notable differences between reactive and nonreactive specimens were observed through real and imaginary impedance, bulk resistance and dielectric constant values. In comparison to nonreactive specimens, reactive specimens revealed smaller real impedance (resistance), larger imaginary impedance (capacitance) and smaller bulk resistance from EIS testing. From microwave testing, reactive specimens exhibit smaller dielectric constants in ambient air and saturated conditions and larger dielectric constants in dry condition compared to nonreactive specimens. Microwave testing also highlighted differences in water volume fraction between reactive specimens and nonreactive specimens; reactive specimens measured much lower water volume fractions. Nondestructive EIS and microwave testing not only revealed general differences between reactive and nonreactive specimens but also specific changes among properties within each sample set over time. Petrographic examination and DRI testing provided further information to correlate EIS and microwave results to visually observed characteristics of the concrete. Acoustic microscope imaging provided little value to this study; additional image analysis is recommended for useful information. A summary of all results is presented in TABLE XVII.

Petrographic examination of the two sample sets revealed an anticipated substantial degree of ASR gel and related deterioration (cracking) in reactive specimens compared to

nonreactive specimens after exposed to ASR-accelerating conditions. The number of ASR gel counts and crack counts from DRI testing, when individually plotted against time, reveal that crack formation plateaus from 180 to 365 days while gel formation rapidly progresses from 180 to 365 days. This finding was unforeseen and quite an important finding for understanding ASR progression in concrete.

Water volume fraction, calculated using dielectric constant values of specimens in different conditions, revealed that available water in both sample sets substantially decreases at 180 days. It is reasonable to deduce that the decrease in water volume fraction at 180 days could be the result of ASR gel progression which consists of the hygroscopic gel absorbing available water from the system. It is also reasonable to postulate that the decrease in water volume fraction at 180 days is the cause of, or at least related to, localized decreasing impedance, bulk resistance and dielectric constant values at 180 days recorded for several of the specimens. The decrease in water volume fraction at 180 days could also be due, in part, to later internal curing such as by hydration of belite portland cement particles, which occurs relatively slowly.

Although EIS and microwave nondestructive testing techniques were successful in differentiating between reactive and nonreactive specimens, it is of importance to note that nonreactive specimens contain fly ash. Because fly ash is known to have a decreasing effect on conductivity of concrete, it should be understood that fly ash, in addition to ASR, has likely affected EIS and microwave results at least to a small degree.

TABLE XVII SUMMARY OF ALL RESULTS

Length Expansion & Mass Change (%)	RA	NRA
Length Expansion	0.229%	0.014%
Mass Change	1.341%	0.465%
Real and Imaginary Impedance (Ohms)	Ambient Air	Saturated
RA Real Impedance	6,450 to 8,920	4,820 to 7,290
RA Imaginary Impedance	-3,150 to -499	-1,080 to -254
NRA Real Impedance	19,100 to 24,900	9,060 to 12,400
NRA Imaginary Impedance	-12,000 to -1,110	-9,620 to -680
Bulk Resistance (Ohms)	Ambient Air	Saturated
RA-28	14,700	8,060
RA-90	14,800	8,190
RA-180	8,920	7,290
RA-365	17,000	8,380
NRA-28	19,100	9,060
NRA-90	20,000	11,500
NRA-180	21,700	16,600
NRA-365	23,100	20,400

Dielectric Constant	*Water Vol. Fraction*	Ambient Air	Saturated	Dry
RA-28	0.16	7.29	7.71	5.33
RA-90	0.17	7.40	8.19	5.58
RA-180	0.13	8.23	8.49	6.25
RA-365	0.16	7.60	8.40	5.86
NRA-28	0.27	7.63	8.64	4.62
NRA-90	0.26	7.99	9.03	4.90
NRA-180	0.20	8.63	9.52	6.08
NRA-365	0.22	7.39	9.25	5.65

DRI Results	Gel in Voids	Total Gel Counts	Frx in Paste	Frx w/ Gel in Paste	Total Frx Counts
RA-28	6	15	67	4	71
RA-90	25	45	142	11	153
RA-180	30	63	234	20	254
RA-365	129	386	105	147	252
NRA-28	0	0	0	0	0
NRA-90	1	1	6	0	6
NRA-180	4	4	10	0	10
NRA-365	11	31	8	10	18

B. Future Work

Even though this study revealed promising results for the use of EIS and microwave testing in nondestructive ASR evaluations, much more work is needed to understand how these techniques can be effectively applied to field investigations. The ability to effectively interpret EIS and microwave data gathered in the field should come after extensive testing of a variety of concrete specimens from both the laboratory and the field. Recommended testing includes the comparison of results from this study performed on air-entrained concrete to that of the study conducted by Heifetz et al. on non-air-entrained concrete to understand the role of air entrainment in EIS and microwave testing. Additionally, testing should be conducted on reactive and nonreactive specimens that consist of the same cementitious materials (only high alkaline portland cement and no SCMs) but different aggregate (e.g. reactive aggregate in RA specimens and nonreactive aggregate in NRA specimens) so that the effect of fly ash is removed from the experiment. Lastly, testing of a multitude of in-situ structures paired with petrographic analysis is recommended to further understanding and correlation of results to confirmed visual observations.

The use of EIS and microwave testing in ASR evaluations is likely to remain only a partially nondestructive method which provides only relative information for a given structure; this is because ASR evaluations typically require visual confirmation of ASR gel in the concrete which is only possible through petrographic examination, a destructive test method. However, if EIS and microwave testing continue to differentiate between ASR-related concrete

characteristics, these techniques have the ability to reduce the amount of concrete extracted from a structure for evaluation purposes.

VI. CITED LITERATURE

1. Abdelrahman, M., ElBatanouny, M., Ziehl, P., Fasl, J., Laroashe, C., and Fraczek, J.: Classification of alkali-silica reaction damage using acoustic emission: a proof-of-concept study. Construction and Building Materials 95:406-413, 2015.

2. ASTM Standard C157, 2017, "Standard test method for length change of hardened hydraulic-cement mortar and concrete," ASTM International, West Conshocken, PA, 2017, DOI: 10.1520/C0157_C0157M-17, www.astm.org.

3. ASTM Standard C192, 2016, "Standard practice for making and curing concrete test specimens in the laboratory," ASTM International, West Conshocken, PA, 2016, DOI: 10.1520/C0192_C0192M-16A, www.astm.org.

4. ASTM Standard C294, 2012 (2017), "Standard descriptive nomenclature for constituents of concrete aggregates," ASTM International, West Conshocken, PA, 2017, DOI: 10.1520/C0294-12R17, www.astm.org.

5. ASTM Standard C295, 2018, "Standard guide for petrographic examination of aggregates for concrete," ASTM International, West Conshocken, PA, 2018, DOI: 10.1520/C0295_C0295M-18A, www.astm.org.

6. ASTM Standard C856, 2018, "Standard practice for petrographic examination of hardened concrete," ASTM International, West Conshocken, PA, 2018, DOI: 10.1520/C0856-18A, www.astm.org.

7. ASTM Standard C1260, 2014, "Standard test method for potential alkali reactivity of aggregates (mortar-bar method)," ASTM International, West Conshocken, PA, 2014, DOI: 10.1520/C1260-14, www.astm.org.

8. ASTM Standard C1293, 2018, "Standard test method for determination of length change of concrete due to alkali-silica reaction," ASTM International, West Conshocken, PA, 2018, DOI: 10.1520/C1293-18, www.astm.org.

9. ASTM Standard C1567, 2013, "Standard test method for determining the potential alkali-silica reactivity of combinations of cementitious materials and aggregate (accelerated mortar-bar method)," ASTM International, West Conshocken, PA, 2013, DOI: 10.1520/C1567-13, www.astm.org.

10. Bois, K.J, Benally, A.D., Nowak, P.S., and Zoughi, R.: Cure-state monitoring and water-to-cement ratio determination of fresh portland cement-based materials using near-field microwave techniques. IEEE Transactions on Instrumentation and Measurement 47(3):628-637, 1998.

11. Chen, J., Jayapalan, A.R., Kim, J.-Y., Kurtis, K.E., and Jacobs, L.J.: Rapid evaluation of alkali-silica reactivity of aggregates using a nonlinear resonance spectroscopy technique. Cement and Concrete Research 40:914-923, 2010.

12. Chen, X.J., Kim, J.-Y., Kurtis, K.E., Qu, J., Shen, C.W., and Jacobs, L.J.: Characterization of progressive microcracking in Portland cement mortar using nonlinear ultrasonics. NDT&E International 41:112-118, 2008.

13. Choi, P., Kim, D.-H., Lee, B.-H., and Won, M.: Application of ultrasonic shear-wave tomography to identify horizontal crack or delamination in concrete pavement and bridge. Construction and Building Materials 121:81-91, 2016.

14. Christensen, B.J., Coverdale, R.T., Olson, R.A., Ford, S.J., Garboczi, E.J., Jennings, H.M., and Mason, T.O.: Impedance spectroscopy of hydrating cement-based materials: measurement, interpretation, and application. Journal of the American Ceramic Society 77(11):2789-2804, 1994.

15. Clayton, D., Khazanovich, L., and Salles, L.: Linear array of ultrasonic test results from alkali-silica reaction (ASR) specimens. *Oak Ridge National Laboratory*, Technical Report: ORNL/TM-2016/159, 2016.

16. Deschenes, D.J.: ASR/DEF-damaged bent caps: shear tests and field implications. Master's thesis, University of Texas at Austin, Texas, 2009.

17. Detweiler, R.: The role of fly ash composition in reducing alkali-silica reaction. *Portland Cement Association*, Technical Report: PCA R&D Serial No. 2092, 1997.

18. Donnell, K.M., Hatfield, S., Zhougi, R., and Kurtis, K.: Wideband microwave characterization of alkali-silica reaction (AR) gel in cement-based materials. Materials Letters 90:159-161, 2013.

19. Donnell, K.M., Zoughi, R., and Kurtis, K.E.: Demonstration of microwave method for detection of alkali-silica reaction (ASR) gel in cement-based materials. Cement and Concrete Research 44:1-7, 2013.

20. Dunbar, P.A., and Grattan-Bellew, P.E..: Results of Damage Rating Evaluation of Condition Concrete from a Number of Structures Affected by AAR. Proceedings of CANMET/ACI International Workshop on AAR in Concrete, Dartmouth, Nova Scotia, CANMET, Department of Natural Resources Canada, 257-265, 1995.

21. Fournier, B., Berube, M., Folliard, K.J., and Thomas, M.D.A.: Report on the diagnosis, prognosis, and mitigation of alkali-silica reaction (ASR) in transportation structures. *Federal Highway Association*, Technical Report: FHWA-HIF-09-004, 2010.

22. Grattan-Bellew, P.E.: Comparison of Laboratory and Field Evaluation of Alkali-Silica Reaction in Large Dams. Proceedings of the First International Conference on Concrete Alkali-Aggregate Reactions in Hydroelectric Plans and Dams, Fredericton, New Brunswick, Canada, 23 p., 1992.

23. Hashemi, A., Horst, M., Kurtis, K., Donnell, K., and Zoughi, R.: Comparison of alkali-silica reaction gel behavior in mortar at microwave frequencies. IEEE Transactions on Instrumentation and Measurement 64(7):1907-1915, 2015.

24. Hashemi, A., Kurtis, K., Donnell, K., and Zoughi, R.: Empirical multiphase dielectric mixing model for cement-based materials containing alkali-silica reaction gel. IEEE Transactions on Instrumentation and Measurement 66(9):2428-2436, 2017.

25. Heifetz, A., Bakhtiari, S., Lu, J., Aranson, I. S., Vinokur, V.M., and Bentivegna, A.: Development of microwave and impedance spectroscopy methods for in-situ nondestructive evaluation of alkali-silica reaction in concrete. AIP Conference Proceedings 1806:120003, 2017.

26. Jamil, M., Hassan, M.K., Al-Mattarneh, H.M.A., and Zain, M.F.M.: Concrete dielectric properties investigation using microwave nondestructive techniques. Materials and Structures 43:77-87, 2013.

27. Ju, T., Achenbach, J., Jacobs, L., Guimaras, M., and Qu, J.: Ultrasonic nondestructive evaluation of alkali-silica reaction damage in concrete prism samples. Materials and Structures 50(1):60, 2017.

28. Klein, C. and Dutrow, B.: Mineral Science. Hoboken, New Jersey, John Wiley & Sons, Inc., 23:536-539, 2008.

29. Kosmatka, S. and Wilson, M.: Design and Control of Concrete Mixtures. Skokie, Illinois, Portland Cement Association 15; 208-212, 2011.

30. Lesnicki, K.J., Kim J.-Y., Kurtis, K., and Jacobs, L.: Assessment of alkali-silica reaction damage through quantification of concrete nonlinearity. Materials and Structures 46:497-509, 2013.

31. Lokajicek, T., Prikryl, R., Sachlova, S., and Kucharova, A.: Acoustic emission monitoring of crack formation during alkali silica reactivity accelerated mortar bar test. Engineering Geology 220:175-182, 2017.

32. Loveday, D., Peterson, P., and Rogers, B.: Evaluation of Organic Coatings with Electrical Impedance Spectroscopy, Part 1: Fundamentals of Electrical Impedance Spectroscopy. Journal of Coatings Technology and Research 12: 46-52, 2004.

33. Rajabipour, F., Giannini, E., Dunant, C., Ideker, J., and Thomas, M.D.A: Alkali-silica reaction: current understanding of the reaction mechanism and the knowledge gaps. Cement and Concrete Research 76:130-146, 2015.

34. Rashidi, M., Knapp, M., Hashemi, A., Kim, J.-Y., Donnell, K., Zoughi, R., Jacobs, L., and Kurtis, K.: Detecting alkali-silica reaction: a multi-physics approach. Cement & Concrete Composites 73: 123-135, 2016.

35. Rivard, P., and Ballivy, G.: Assessment of the expansion related to alkali-silica reaction by the Damage Rating Index method. Construction and Building Materials 19:83-90, 2005.

36. Rivard, P. Fournier, B. and Ballivy, G.: Quantitative petrographic technique for concrete damage due to ASR: experimental and application. Cement, Concrete, and Aggregates 22:63-72, 2000.

37. Sargolzahi, M., Kodjo, S.A., Rivard, P., and Rhazi, J.: Effectiveness of nondestructive testing for the evaluation of alkali-silica reaction in concrete. Construction and Building Materials 24:1398-1403, 2010.

38. Shi, T., Zheng, L., and Xu, X.: Evaluation of alkali reactivity of concrete aggregates via AC impedance spectroscopy. Construction and Building Materials 145:548-554, 2017.

39. Snyder, K.A. and Lew, H.S.: Alkali-silica reaction degradation of nuclear power plant concrete structures: a scoping study. *National Institute of Standards and Technology*, Internal Report: NISTIR 7937, 2013.

40. Stanton, T.E.: Expansion of concrete through reaction between cement and aggregates. Proceeding of the American Society of Civil Engineers 66:1781-1811, 1940.

41. Wen, S. and Chung, D.D.L.: Effect of admixtures on the dielectric constant of cement paste. Cement and Concrete Research 31:673-677, 2001.

42. Zhang, T., Zhou, Liangdong, Z., Ammari, H., and Seo, J.-K.: Electrical impedance spectroscopy-based defect sensing technique in estimating cracks. Sensors 15:10909-10922, 2015.

VII. VITA

Meredith Strow completed a Bachelor of Science in Geology with a minor in Environmental Studies from Illinois State University in 2013. Ms. Strow has been published twice for undergraduate research and was awarded the SGD-SEPM Student Poster Excellence Award (funded by Nexen) for her presentation of research at the Geological Society of America 2012 Annual Meeting.

Currently, Ms. Strow is employed as a concrete petrographer, conducting forensic evaluations of concrete and other building materials. She examines materials using microscopical techniques and interprets observations to assess for quality and condition. She also identifies deleterious mechanisms, such as ASR, in concrete. Ms. Strow routinely performs ASTM C295, C457, and C856 testing and manages material evaluations often requiring a multi-faceted forensic approach to solve complex construction problems.